UNIVERSITY OF CALIFORNIA
RIVERSIDE

Indocyanine Green Loaded Nanoconstructs for Optical Imaging and Phototherapeutic Applications

A Dissertation submitted in partial satisfaction
of the requirements for the degree of

Doctor of Philosophy

in

Bioengineering

by

Baharak Bahmani

August 2013

Dissertation Committee:
Prof. Bahman Anvari, Chairperson
Prof. Ameae M. Walker
Prof. Valentine I. Vullev

The Dissertation of Baharak Bahmani is approved:

Committee Chairperson

University of California, Riverside

ACKNOWLEDGEMENTS

This study would not have been completed without the support, patience and guidance of many people. It is to them that I owe my deepest gratitude. I would like to thank my thesis committee. I am grateful to my thesis advisor, Prof. Bahman Anvari for his wisdom, knowledge and commitment to the highest standards, which inspired and motivated me. I would like to thank Prof. Valentine Vullev for his support and guidance. I am grateful to Prof. Ameae Walker for her insight and guidance.

I am grateful to the entire AnvariBiophotonicsLab for supporting, inspiring and encouraging me in the past five years in particular, Mr. Yadir Guerrero. I'm thankful for the support I received from several professors including Prof. Victor Rodgers and Prof. Hyle Park as members of my dissertation proposal committee, Prof. Jaiyu Liao and his entire lab, Prof. Christian Lytle and Dr. David Carter. I also would like to thank Mrs. Hong Xu in the Bioengineering Department and Mrs. Leslie Karpinski and Mrs. Sally Scott in the Office of Campus Veterinarian for their help, guidance and patience.

I would like to extend my sincere appreciation to Hamed Hosseini Bay, my husband, for his constant love, support and patience. I wouldn't have been here without his support and encouragement. I would like to express my deepest gratitude to my parents for their unconditioned love and support, which have taught me so much about sacrifice.

Finally, I would like to thank all my friends, who inspired me everyday despite the stress and work pressure we were facing.

ABSTRACT OF THE DISSERTATION

Indocyanine Green Loaded Nanoconstructs for Optical Imaging and Phototherapeutic Applications

by

Baharak Bahmani

Doctor of Philosophy, Graduate Program in Bioengineering
University of California, Riverside, August 2013
Dr. Bahman Anvari, Chairperson

Development of theranostic nano-constructs may enable diagnosis and treatment of diseases at high spatial resolution. Optically active nanoparticles are widely pursued as exogenous chromophores in diagnostic imaging and phototherapeutic applications. However, the blood circulation time of nanoparticles remains limited due to the rapid clearance of the nanoparticles by reticuloendothelial system (RES). Coating with Polyethylene glycol (PEG) is a strategy to extend the circulation time of nanoparticles. Here, we report PEGylation of polymeric-based nanocapsules loaded with Indocyanine green (ICG) and effect of PEG's molecular weight on the uptake of these nanocapsules by human spleen macrophages and hepatocytes using flow cytometry. To characterize the biodistribution of the constructs, we performed in vivo quantitative fluorescence imaging in mice and subsequently analyzed the various extracted organs. Our results suggest that encapsulation of ICG in these PEGylated constructs is an effective approach to prolong

the circulation time of ICG and delay its hepatic accumulation. Increased bioavailability of ICG, offers the potential of extending the clinical applications of ICG. Targeted delivery of therapeutic and imaging agents using surface modified nanovectors has been explored immensely in recent years. The growing demand for site-specific and efficient delivery of nanovectors entails stable surface conjugation of targeting moieties. Our ICG-loaded polymeric nanocapsules (ICG-NCs) have potential for covalent coupling of various targeting moieties and materials due to presence of amine groups on the surface. Here, we covalently bioconjugate PEG-coated ICG-NCs with monoclonal anti- HER2 through reductive amination-mediated procedures. The targeting abilities of HER2 functionalized ICG-NCs toward ovarian cancer was investigated in-vitro. Since these functionalized nanoconstructs have potential applications in laser-induced photodestruction of ovarian cancer cells, we studies NIR laser induced phototherapy of ovarian cancer cells in-vitro. Other than polymeric theranostic nano-constructs, here we demonstrate the first successful engineering of hybrid nano-scale constructs derived from membranes of hemoglobin-depleted erythrocytes that encapsulate ICG. We show the utility of the constructs as photo-theranostic agents in fluorescence imaging and photothermal destruction of human cells. These erythrocyte-mimicking nano-structures can be derived autologously, and may have broad applications in personal nanomedicine ranging from imaging and photo-destruction of cancerous tissues to vascular abnormalities, and longitudinal evaluations of therapeutic interventions.

TABLE OF CONTENT

LISTS OF FIGURES

CHAPTER 1: INTRODUCTION

Nano-carriers containing near-infrared (NIR) exogenous chromophores are currently under investigation for use as site- specific and sensitive optical imaging probes, and in phototherapeutic applications. Some major advantages of utilizing NIR optical probes are that: 1) the light in this spectral bandwidth (700-1000 nm) is absorbed less by water and proteins in biological tissue; allowing for deeper light penetration (several centimeters) into the tissue; and 2) the exogenous chromophore increases the signal to background ratio by overcoming the tissue autofluorescence.

Indocyanine green (ICG) is the only NIR exogenous chromophore approved by Food and Drug Administration (FDA), and used for assessment of hepatic function and cardiac output measurement.[1–5] However, circulating ICG in plasma binds to albumin and high-density lipoproteins (HDLs) such as alpha-1lipoprotein resulting in short vascular circulation time and exclusive clearance by liver.[6,7] Encapsulation of ICG in various constructs has been extensively studied to: (1) enhance optical and thermal stability of ICG; (2) to reduce non-specific protein binding to ICG; and (3) to prolong vascular half-life of ICG.[8–10] Our group has previously reported on encapsulation of ICG into polymeric nanocapsules.[11–16]

One main challenge associated with all types of nanoparticles in blood stream is phagocytosis by cells of the reticuloendothelial system (RES). This non-specific recognition of nanoparticles by RES is facilitated through opsonization.[17–19] Diminishing

protein adsorption to the surface of nanoparticles can minimize the interaction with RES cells. Grafting Polyethylene glycol (PEG) on the surface of various types of nanoparticles is a strategy to reduce phagocytosis.[20–22]

The second chapter of this thesis describes studies to assess effect of PEGylation on uptake of ICG-loaded nanocapsules by cells or RES, in particular human macrophages and hepatocytes. Using optical absorbance spectroscopy and flow cytometry, we investigate the effect of molecular weight (MW) of PEG [5000 and 30,000 Daltons (Da)] on the phagocytic content of human spleen macrophages incubated with ICG- containing nanocapsules (ICG-NCs) between 15 to 360 min. We also study the interaction of PEGylated ICG-NCs with human hepatocytes in-vitro. Our results indicate that surface coating with PEG is an effective method to reduce the phagocytic content of ICG-NCs within macrophages for at least up to 360 min of incubation time. Coating the surface of ICG-NCs with the low MW PEG results in lower phagocytic content of ICG-NCs within macrophages for at least up to 60 min of incubation time as compared to ICG-NCs coated with the high MW PEG. Surface coating of ICG-NCs with PEG is a promising approach to prolong vasculature circulation time of ICG for NIR imaging and phototherapeutic applications.

In chapter 3, we focus on biodistribution of PEGylated ICG-NCs in healthy mice using quantitative fluorescence imaging and analysis of organs. Motivated by results of our previous in-vitro studies, in the study reported here, we extended our investigations to evaluate the effectiveness of encapsulation and coating the surface of ICG-NCs with 5 KDa PEG in extending the circulation time of ICG and to investigate the utility of these

ICG-NCs for in vivo quantitative fluorescence imaging. We compare biodistribution of PEGylated ICG-NCs with non-coated ICG-NCs and freely dissolved ICG in PBS up to one hour post-injection. Our results suggest that encapsulation of ICG in these PEGylated constructs is an effective approach to prolong the circulation time of ICG and delay its hepatic accumulation. Increased bioavailability of ICG, due to encapsulation, offers the potential of extending the clinical applications of ICG, which are currently limited due to rapid elimination of ICG from the vasculature. Our results also indicate that PAH and ICG-doped nanocapsules (ICG-NCs) are not cytotoxic at the levels used in this study.

Ovarian cancer is the leading cause of cancer-related death among all types of gynecological cancer.[23] Detection of ovarian cancer in early stages has remained a great challenge. Additionally, for patients diagnosed at advanced stages of the disease, the effectiveness of the therapy including cytoreduction surgery or complete removal of ovaries followed by chemotherapy, depends on successful removal of tumor masses specially the very small ones.[24] Unfortunately, visualization of very small tumor masses (<3 mm in diameter) utilizing CT, CT/PET, MRI or visual inspection is very difficult. One approach to enhance visualization of small tumor deposits is to use targeted fluorescence imaging probes.[25]

Chapter 4 describes surface functionalization of ICG-NCs for targeted fluorescent imaging and laser-mediated phototherapy of ovarian cancer. Here, we investigate the effectiveness of ICG loaded nanoparticles (ICG-NCs) functionalized with anti-HER2 for targeted fluorescent imaging and laser-mediated photodestruction of ovarian cancer cells in vitro. The monoclonal anti-HER2 antibody is conjugated to the surface of

nanoparticles using double aldehyde terminated polyethylene glycol (PEG) chains as linker through reductive amination procedure. We study targeted imaging of two different ovarian cancer cell line, SKOV3 and OVCAR3, using fluorescent confocal microscopy and flow cytometry. The laser-mediated photodestruction ability of nanoparticles is investigated using and 808 nm continuous laser. Our results suggest that the anti-HER2 functionalized nanoparticles can actively target ovarian cancer cells, which is successfully demonstrated by both fluorescent confocal microcopy and flow cytometry. Post-targeting ovarian cancer cells, theses nanoconstructs can cause photothermal damage to the cells mediated by NIR laser irradiation.

In chapter 5, we demonstrate the first successful engineering of hybrid nano-scale constructs derived from membranes of hemoglobin-depleted erythrocytes that encapsulate the near infrared chromophore, indocyanine green. We show the utility of the constructs as photo-theranostic agents in fluorescence imaging and photothermal destruction of human cells. These erythrocyte-mimicking nano-structures can be derived autologously, and may have broad applications in personal nanomedicine ranging from imaging and photo-destruction of cancerous tissues to vascular abnormalities, and longitudinal evaluations of therapeutic interventions.

In Summary, the studies described here show the polymeric nanocapsules loaded with ICG have potential for optical diagnostic and therapeutic applications. In particular, when functionalized with monoclonal anti-HER2, can successfully target ovarian cancer cells and photothermally damage these cells. Such functionalized nanoconstructs can be used intraoperatively for diagnostic and laser-mediated phototherapy of ovarian cancer.

Moreover, we report the first proof-of-principle to demonstrate the successful engineering of ICG-loaded nano-sized vesicles derived from erythrocyte ghosts, and their utility as photo-theranostic agents for fluorescence imaging and photothermal destruction of cells.

CHAPTER 2: Effect of Polyethylene Glycol Coatings on Uptake of Indocyanine Green Loaded Nanocapsules by Cells of Reticuloendothelial System (RES) *In-Vitro*

2.1 INTRODUCTION

The ability to detect and visualize tissue and vascular malformations constitutes a fundamentally crucial step for early diagnosis of disease, selecting an appropriate therapeutic approach, and monitoring the effectiveness of the therapy. For example, early and accurate tumor detection is the first step towards diagnosis, treatment, and clinical management of cancer. Development of highly sensitive probes with high specificity that would enable diagnosis of pre-malignant lesions and early stage tumors remains as one of the great challenges of oncology. Recent advances in extreme miniaturization to the nano-scale now provide the technological basis and potential for the development of nano-sized materials that may enable early diagnosis and treatment of a wide range of diseases such as cancer at cellular and molecular levels. In recent years, such nano-materials have been studied for their utilities in imaging of tissue abnormalities including cancerous cells, and delivering therapeutic drugs.[26–29]

Near-infrared (NIR) fluorescence imaging using exogenous chromophores with sizes on the nano-scale has been gaining increased attention as an enabling technology with highly sensitive and target specific capabilities.[29–35] The use of NIR wavelengths is particularly advantages in that there is relatively deep optical penetration and emission (on the order of several centimeters) over this spectral bandwidth with minimal

autofluorescence. Additionally, utilization of NIR wavelengths in combination with nano-scale optical contrast agents can provide a methodology for subcellular and molecular imaging.

Indocyanine green (ICG) is a cyanine NIR dye approved by United States Food and Drug Administration (FDA) for assessment of cardiac output, hepatic function and ophthalmological vascular imaging.[1–5] Additionally, ICG has been studied for potential phototherapeutic applications including photothermal destruction of tumors and photocoagulation of blood vessels,[36–38] treatment of skin disorders,[39–41] and as a sensitizer for photodynamic therapy (PDT) of cancer.[42,43]

Current method of administering ICG is by dissolving it in isotonic saline solution, and delivering it intravenously. Despite its clinical usage, ICG in its current formulation, suffers from several major drawbacks: (1) concentration of the ICG solution and the nature of solvent have a significant influence on its absorption properties;[44–47] (2) after a bolus injection, ICG binds readily to albumin and high-density lipoproteins (HDLs) in blood plasma, resulting in changes in its optical absorbance and fluorescence emission properties;[48,49] and (3) ICG is cleared rapidly from the body, showing a rapid vascular clearance with half-life on the order of 3-4 minutes,[50,51] and eliminated from the general circulation by hepatocytes.

Given the optical instability of ICG when exposed to physiologically relevant conditions (e.g., blood plasma, and body temperature), its short vascular circulation time, and nearly exclusive uptake by the liver, the true potential of this non-toxic and clinically proven exogenous chromophore for optical imaging and phototherapeutic applications

remains limited. Recent studies demonstrate that encapsulation of organic dyes help stabilize their optical properties, mainly due to the protecting role of the encapsulating structure, which shields the embedded fluorophore from the external.[11,52] To-date, a number of nanoconstructs have been developed to encapsulate ICG. These systems have been constructed from polymeric micelles formed from poly(styrene-alt-maleic anhydride)-block-poly(styrene)) diblock copolymers,[10] poly-lactic co(glycolic)-acid (PLGA) particle,[52,53] phospholipid emulsions,[8,54] modified silicate matrices,[9] and calcium phosphate.[35] These studies have demonstrated improved optical stability of ICG resulting from encapsulation, and are very encouraging in that they demonstrate nano-encapsulation of ICG provides a potential technique for targeted optical imaging.

We have previously reported on ICG loading into polymeric nanocapsules composed of cross-linked poly(allylamine) hydrochloride (PAH) and sodium salt.[11–16] Certain advantages, associated with our ICG-containing nanocapsules (ICG-NCs), set them apart from other ICG-doped constructs. Our constructs are spontaneously self-assembled via green-chemistry in aqueous media within 10-30 seconds, and the entire time to impregnate the nanocapsules with ICG does not exceed two hours. The self-assembly of a readily available polymer (PAH) via electrostatically-driven cross-linking with multivalent inorganic anions, phosphates, produces capsules with a broad range of sizes and physical stability with ability for different types of dye loading.

A common problem that nearly all types of nanoparticles will have to overcome once within the vasculature is the issue of clearance from the vasculature and non-specific recognition. Phagocytic cells of reticuloendothelial system (RES), comprising of

liver, spleen, and bone marrow, play a key role in clearance of foreign particles from circulation. The interaction between these cells and nanoparticles is mediated through the presence of specific proteins adsorbed on the surface of nanoparticles. *In-vivo* clearance of nanoparticles from circulation is dependent on the level of protein adsorption on their surface and intracellular uptake by the phagocytic cells.[18,19,55,56] Therefore, shielding the nanoparticles from macrophages, by minimizing the interaction between macrophages receptors and proteins adsorbed on the surface of nanoparticles, is expected to increase the circulation time of the nanoparticles.

Use of polyethylene glycol (PEG) to coat the surface of nanoparticles has been investigated as a methodology to minimize the interaction between nanoparticles and macrophages.[20,21,57–60] PEG is a water-soluble biocompatible polymer with highly ambulant and flexible chains.[61] On a PEGylated surface, the major forces between the surface and proteins in the solution are steric repulsion, Van der Waals attraction and hydrophobic [22]. When the steric repulsion prevails the attraction forces between proteins and PEG chains, the surface becomes less susceptible to protein adsorption.[62–64]

The density and conformation of PEG molecules on the surface are two crucial factors in determining the net interfacial forces governing protein adsorption. On a low density PEGylated surface, the steric repulsion force between the proteins attempting to attach to the PEGylated surface and the PEGylated surface would be smaller as a result of reduced hydration energy per chain and unit surface. The conformation of PEG chains on the surface depends on the molecular weight (MW) of the PEG. In low MW PEG, chains

extend out in helical conformation and form a brush-like layer. However, in high MW PEG, chains entangle with each other and form a mushroom-like layer.[65–70]

As the first step towards characterizing the influence of PEGylating the surface of ICG-loaded nanocapsules (ICG-NCs) on circulation and biodistribution of the capsules, herein, we report the effects of ICG-NCs surface PEGylation on the uptake of the capsules by human spleen macrophages *in-vitro*. Specifically, we investigate the effect of PEG's MW on the uptake level of the ICG-NCs by macrophages. The results presented here provide a basis for the design of ICG-NCs with optimal surface properties required for prolonged circulation of these nanocapsules *in-vivo*.

2.2 MATERIALS AND METHODS

2.2.1 Materials

Sodium phosphate dibasic heptahydrate ($Na_2HPO_4.7H_2O$, Fisher Scientific), poly(allylamine) hydrochloride (PAH, Sigma-Aldrich), Indocyanine green (Sigma-Aldrich), Methoxy-Poly (ethylene glycol)-Butyraldehyde (PEG-ALD, MW= 5,000 and 30,000 Da, Laysan Bio Inc.), Sodium dithionite ($Na_2S_2O_4$, Sigma-Aldrich) and Phosphate buffer saline (PBS, Fisher BioReagents) were used as purchased.

2.2.2 Cell lines

Human spleen macrophages (KMA cell line, ATCC®) were cultured in Iscove's modified Dulbecco's medium (IMDM) supplemented with 4 mM L-glutamine, 1.5 g/L sodium bicarbonate, 0.02 mM thymidine, 0.1 mM hypoxanthine, 0.05 mM 2-mercaptoethanol, 10% fetal bovine serum, and 1% penicillin. Normal human hepatocytes

(HH, ScienCell) were cultured in hepatocyte medium (HM) containing 500 ml of basal medium supplemented with 25 ml of fetal bovine serum, 5 ml of hepatocyte growth supplement, and 5 ml of penicillin/streptomycin solution.

2.2.3 Synthesis of ICG-loaded Nanocapsules

ICG-loaded nanocapsules (ICG-NCs) were synthesized through a self-assembly method described in details previously.[11–16] First a polymeric aggregate was formed through ionic cross-linking between 20 μL of PAH solution (2 mg/mL DI water, 4 ºC) and 60 μL of disodium phosphate salt solution (0.01 M in DI water, 4 ºC) by mixing them for 10 seconds. Subsequently, 1.2 mL of cooled deionized water (4 ºC) was added to the polymeric aggregate suspension, followed immediately by the addition of 240 μL of cooled ICG stock solution (500 μg/mL DI water, 4 ºC)). The nanocapsule suspension was mixed for 10 seconds and then aged for 20 minutes in dark at 4 ºC. The nanocapsule suspension was washed twice through centrifugation at 3000 rpm for 2 hours at 4 ºC.

The size of polymeric aggregate formed during the first step of synthesis can be tuned through altering the ratio of total negative charge of the Na_2HPO_4 salt to the total positive charge of PAH, defined as *R* ratio.[12,16] In this study, *R* value was set at 2. Using an *R* ratio higher than 2 will results in formation of larger and fast growing aggregates.

2.2.4 PEG-coating

After ICG-NCs were formed, the amine groups on the surface of the capsules were used as the sites for covalent coupling with Aldehyde-terminated Polyethylene glycol (PEG-ALD) via reductive amination. Reductive amination is an important

technique to form a covalent bond between carbon and nitrogen.[71] In this process, an aldehyde or ketone is condensed with an amine in the presence of a reducing agent. Since hydride reducing agents, such as cyanoborohydride, are detrimental for cyanine dyes, we employed sodium dithionite, as a reductant in coating the ICG-NCs. The Schiff base (i.e., the imine) formed between the aldehyde-terminated PEGs and the surface amines of the nanocapsules is not sufficiently stable under physiological conditions. Therefore, we added sodium dithionite, to irreversibly convert the imines into amines and afford covalent coating of the nanocapsules with PEG (Scheme 1).

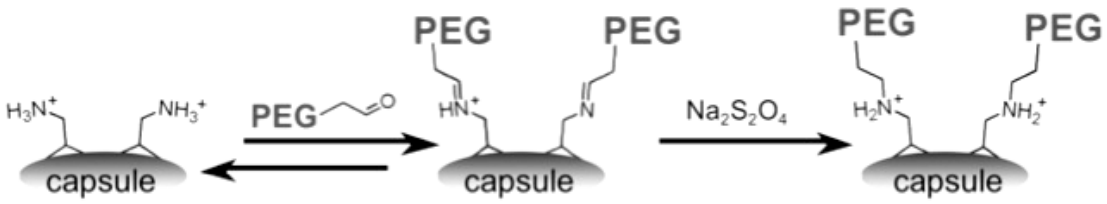

Scheme 1 Synthesis procedure for PEGylation of ICG-loaded nanocapsules through reductive amination.

Since a maximum of three PEG chains can be conjugated on ≈1 nm², we aimed to achieve a minimum number density of 1 chain/nm² by conjugating at least 10 Aldehyde-terminated PEG chains per 10 nm^2 of nanocapsule surface, and determined the required amount of PEG-ALD based on diameter and number of nanocapsules in the suspension.

Aldehyde-terminated PEGs with two different MWs (5,000 Da and 30,000 Da) were used. Sodium dithionite was used as the reducing agent and was added as a solid to the nanocapsules suspension at approximately two equivalents per mole PEG-ALD. The suspension of ICG-NCs, PEG-ALD and Sodium hydrosulfite was aged for at least 8 hours in dark at 4 ºC. The sample was then dialyzed in water for 48 hours in dark at 4º C.

Water was changed every 12 hours during the dialysis. To separate possible remaining reducing agent, the sample was centrifuged at 3000 rpm for 2 hours (twice) at 4º C. As a control set, ICG-NCs were coated with PEG-ALD non-covalently in absence of the reducing agent, resulting in formation of unstable Schiff base between amine groups on the surface of ICG-NCs and the PEG-ALD molecules.

2.2.5 Characterization of Nanocapsules

The morphology of lyophilized uncoated ICG-NCs was examined by scanning electron microscopy (SEM, Philips, XL-30 FEG). Diameter distribution of these capsules was quantified by analysis of the SEM images using the ImageJ software.

Optical absorbance spectra of PEG-coated ICG-NCs were obtained using a UV-Visible spectrophotometer (Cary 50 UV-Vis spectrophotometer). Presence of PEG on the surface of nanocapsules was verified by Fourier transform infra-red spectroscopy (FTIR) using a Perkin-Elmer 1600 series spectrometer. The zeta (ζ)-potentials of nanocapsules were measured by Laser Doppler Velocimetry (LDV) (Zetasizer Nanoseries, Nano-ZS90) to further confirm PEGylation.

2.2.6 Incubation of Human Spleen Macrophages with ICG-NCs

To study the interaction of ICG-NCs with cells of reticuloendothelial system (RES), ICG-NCs were incubated with human spleen macrophages. We added 200 µl of cell suspension ($\approx 5\times10^5$ cells/ml) in growth media (IMDM) to each well of a 96-well flat-bottomed micro-titer plate. Subsequently, 100 µl of uncoated ICG-NCs, PEG-ALD (MW=5,000 Da) coated ICG-loaded nanocapsules (PEG-5k-coated ICG-NCs) and PEG-

ALD (MW=30,000 Da) coated ICG-loaded nanocapsules (PEG-30k-coated ICG-NCs) were separately added to cell suspensions. Freely dissolved ICG (free ICG) in PBS was used as positive control, and cell suspension without ICG-NCs or free ICG was considered as negative control.

Cells were incubated with samples and positive control for 30 minutes and two hours without exposure to light in an incubator at 37 °C with 5% CO_2. Following incubation, the suspension of cells and ICG-NCs were washed at low speed centrifugation (1200 rpm) to separate any remaining suspended NCs from cells.

2.2.7 Incubation of Human Hepatocytes with ICG-NCs

To study the interaction of human hepatocytes with ICG-NCs, hepatocytes were cultured in 12-well flat-bottomed plate 24 hours. Subsequently, 200 µl of uncoated ICG-NCs, PEG-5k-coated ICG-NCs, or PEG-30k-coated ICG-NCs were added to wells. Cells were incubated between 15 minutes to two hours in dark at 37 °C and supplied with 5% CO_2. Following incubation, cells were washed with PBS twice and trypsinized for flow cytometry analysis.

2.2.8 Fluorescent Imaging of Spleen Macrophages

Cells were resuspended in growth medium after centrifugation. An Electron Multiplier (EM) gained CCD camera (Quant EM-CCD, Hamamatsu) in combination with a long pass emission filter (>770 nm) were used to capture the fluorescent images of the cells in response to 740±35 nm excitation wavelength. Camera exposure time was set at 0.1 seconds in all imaging sessions. The contrast and brightness window of all

fluorescent images were normalized to the fluorescent image of cells incubated with free ICG (positive control) using ImageJ software.

2.2.9 Quantification of ICG Content within Macrophages

Following incubation with ICG-NCs or free ICG, macrophages were dissolved in Sodium Dedecyl Sulfate (SDS). Upon exposure to SDS, macrophages are lysed, and release their ICG content. The absorbance spectra of solutions containing the lysed cells in SDS were collected. We took advantage of exclusive NIR absorbance by ICG to quantify the ICG content of lysed cells. Specifically, the ICG content was quantified using a calibration that yielded a linear relationship between peak absorbance at λ=790 nm, and ICG dissolved in SDS at different concentrations. Saxena et al.[72] and Yaseen et al.[14] have used a similar method to quantify the uptake of ICG-containing PLGA nanoconstructs by cervical cancer cell lines *in-vitro*, and biodistribution of PAH-based ICG-NCs in healthy mice, respectively.

2.2.10 Characterization of ICG-NCs Phagocytic Content and hepatocytes uptake by Flow Cytometry

We used flow cytometry to characterize the phagocytic content of ICG-NCs. Human spleen macrophages were incubated with free ICG, uncoated, and PEG-coated ICG-NCs for various time intervals ranging between 15-360 minutes. Following each incubation time, we detected overall fluorescent emission from a large population of human spleen macrophages exposed to free ICG and ICG-NCs by flow cytometry. Cells were washed with PBS twice through centrifugation (1200 rpm for 4 minutes) and

resuspended in PBS. FITC Annexin V (BD Biosciences) apoptosis detection kit and Propidium Iodide (PI) were used to identify late apoptotic and dead cells, respectively, so that they could be excluded from the analysis. Macrophages were also labeled with fluorescent maker Phycoerythrin **(**PE) mouse anti-human CD11b/Mac-1. The integrin receptor CD11b/Mac-1 regulates the adherence and survival of activated macrophages. Therefore, we utilized the PE mouse anti-human CD11b/Mac-1 to discern activated macrophages from any other cell types. The prepared cells were analyzed by flow cytometer (BD FACSAria cell sorter) using 633 nm excitation and 785 nm emission wavelength for ICG detection. The fluorescent intensity distributions and mean fluorescent intensity (MFI) of PI negative but PE mouse anti-human CD11b/Mac-1 positive cells were used to quantify the interaction level of the human spleen macrophages with free ICG or ICG-NCs.

To study the uptake of ICG-NCs by hepatocytes, we utilized flow cytometry. We used FITC Annexin V apoptosis detection kit and Propidium Iodide (PI) to identify the dead cells and those in final apoptosis stages in order to eliminate the fluorescent signal associated with these cells from the analysis.

2.3 RESULTS AND DISCUSSION

2.3.1 Nanocapsules Characterization

ICG-NCs were completely spherical in shape (Fig. 1(a)). Diameter distribution of lyophilized uncoated ICG-NCs, as determined from the analysis of SEM images, is shown in Fig. 1(b). The particles mean diameter was 250 ± 40 nm.

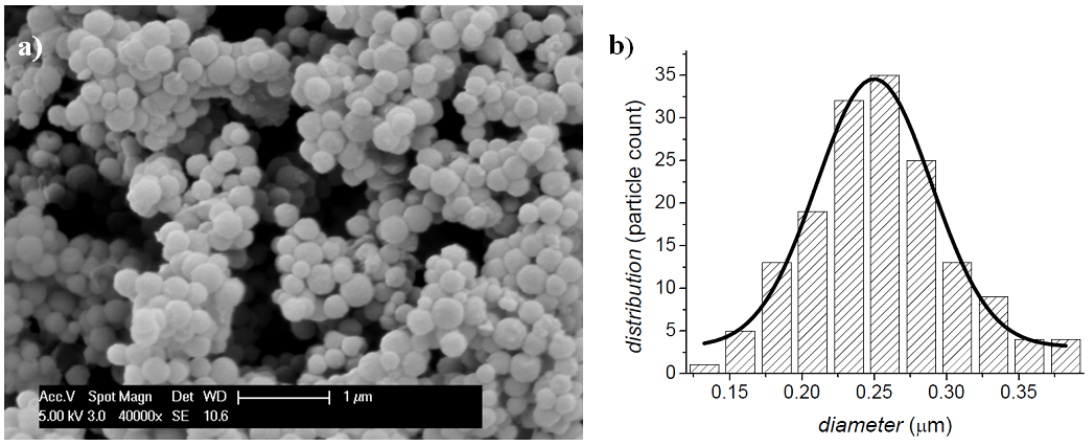

Figure 1 (a) SEM image, and (b) diameter distribution of lyophilized uncoated ICG-loaded nanocapsules. A Gaussian fit to the measured diameter distribution is also shown in panel (b).

The optical absorption and fluorescence spectra of free ICG, uncoated ICG-NCs, PEG-5k-coated ICG-NCs and PEG-30k-coated ICG-NCs are shown in Fig. 2. Concentration of free ICG and that used to construct the ICG-NCs were 4 μM and 3 μM, respectively. The absorption spectrum for free ICG displays the peak absorbance values at 780 and 680 nm, corresponding to the monomeric and dimeric forms of ICG, respectively. Increased absorbance values in the spectral bands of 570-765 nm, and >814 nm are observed for uncoated and PEG-coated ICG-NCs (Fig. 2(a)). There are red shifts in the wavelengths associated with monomeric and dimeric forms for PEG-coated ICG-NCs. The difference in absorbance values are between 0-5% for uncoated and PEG-coated ICG-NCs in the 550-810 nm spectral range, and virtually none for wavelengths greater than ≈810 nm (Fig. 2(a)). There are very minimal differences in absorbance values of PEG-5k and PEG-30k coated ICG-NCs. Changes in absorbance spectra of uncoated and PEG-coated ICG-NCs may be induced by conformational changes in ICG

within the confined environment of the capsules, and have also been reported in a previous report utilizing PAH-based ICG-NCs.[12–15,73]

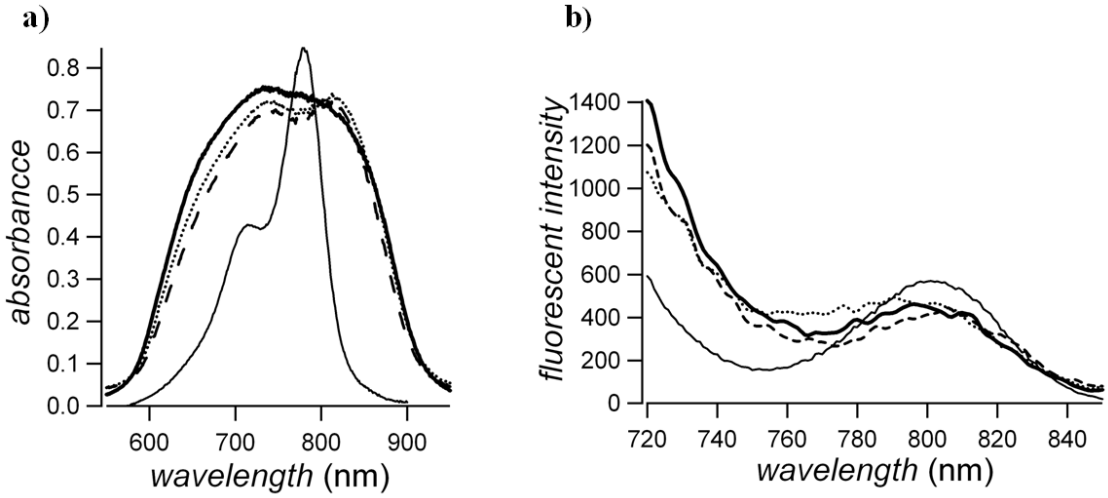

Figure 2 (a) Absorbance spectra, and (b) emission spectra of PEG-5k-coated ICG-NCs (doted line), PEG-30k-coated ICG-NCs (dashed line), uncoated ICG-NCs (solid thick line) and freely dissolved ICG in water (solid thin line). The emission spectra of uncoated and PEG-coated ICG-NCs were smoothed using IGOR Pro software with 2nd order binominal algorithm.

The fluorescence spectra indicate that there is reduced emission in the narrow 720-730 nm band for PEGylated ICG-NCs (Fig. 2(b)). Interestingly, over the 750-790 nm spectral band, there is increased emission from PEG-5k-coated ICG-NCs as compared to uncoated capsules. Overall, the spectra presented in Fig. 2 suggest that PEGylation does not compromise the absorbance and emission characteristics of ICG-NCs.

The characteristic peaks of PEG-ALD were observed in the FTIR spectra of ICG-NCs with the coating achieved by performing the reduction step (Fig. 3). The peak at ~3500 cm^{-1} in both spectra for PEG-ALD and PEG-coated ICG-NCs is attributed to the

N-H and O-H bonds. The sharp peak at ~2900 cm^{-1} in these two spectra corresponds to C-H stretching.

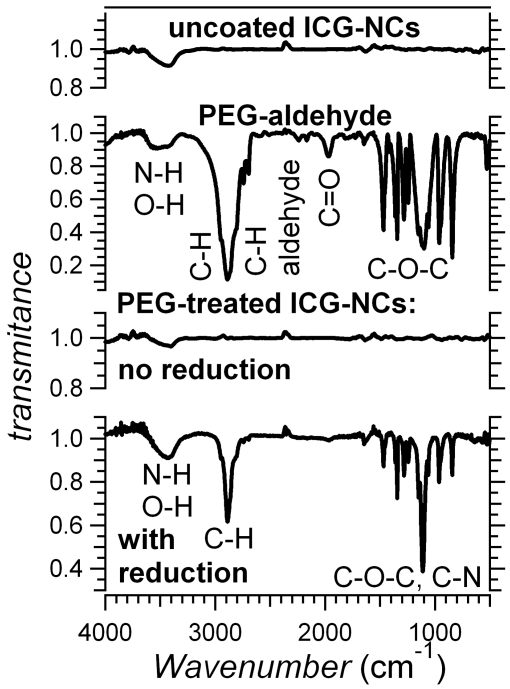

Figure 3 FTIR spectra of uncoated ICG-NCs, PEG-aldehyde, and PEG-treated ICG-NCs with and without the reductive amination step.

The peaks at ~2650-2750 cm^{-1} and ~1900 cm^{-1} in the pure PEG-ALD spectrum are attributed to the aldehyde (O=)C-H stretch, and the carbonyl group (aldehyde C=O stretching), respectively, and both of these peaks are absent in the spectrum of PEG-treated ICG-NCs with reduction step. The peaks in the 900-1500 cm^{-1} range correspond to vibrational modes of C-O-C bonds of PEG in the spectra of pure PEG-ALD and PEG-coated ICG-NCs. The sharp peak at ~1100 cm^{-1} in PEG-coated ICG-NCs spectra is vibrational mode of C-N bond. No specific peaks of PEG-ALD were detected for the PEG-treated ICG-NCs without the reduction step indicating the necessity to perform this

step in order to achieve successful PEGylation. That spectrum was similar to that of uncoated ICG-NCs, indicating that amination coupling in the absence of reducing agent did not yield PEG coatings on ICG-NCs.

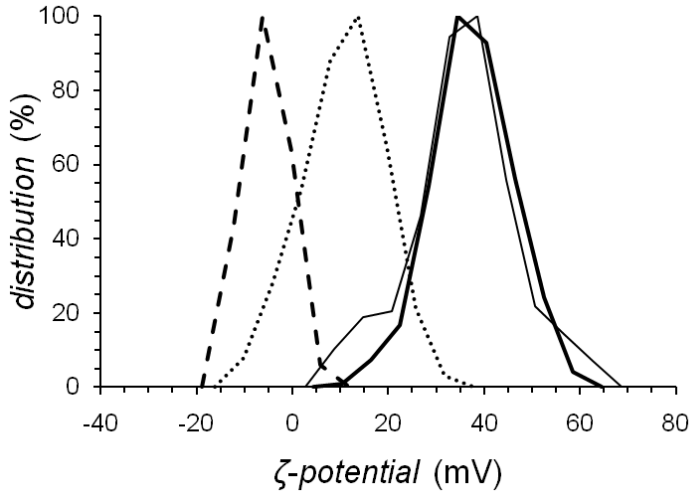

Figure 4 ζ-potential distributions for uncoated (solid thick line), PEG-30k-coated with no reduction (solid thin line), PEG-5k-coated with no reduction (doted line), and PEG-30k-coated ICG-NCs with reduction (dashed line) measured in water at room temperature.

The ζ-potential distribution (in -20 to +50 mV range), and its peak value (≈40 mV) for uncoated ICG-NCs were nearly identical to those of the capsules where formation of PEG-ALD coating was attempted without the reduction step (Fig. 4). These similarities indicate that in the absence of the reduction step, PEG-ALD coating cannot be successfully produced. When utilizing the reductive amination step, the ζ-potential distributions for PEG-5k-coated ICG-NCs, and PEG-3-k-coated ICG-NCs were altered with the respective peak values shifted to ≈12 and -7 mV, indicating successful formation of PEG-ALD coating on the surface of the capsules. The reduction in ζ-potential of PEGylated samples could be due to the increase in thickness of stern layer formed around

the PEG-coated ICG-NCs. Subsequently the position of the slipping plane at electrical double layer will change and move away from the surface of ICG-NCs.[74–76]

2.3.2 Fluorescence Imaging of Cells

None or minimal fluorescence was detected from human spleen macrophages at 30 minutes and two hours of incubation with PEG-5k-coated ICG-NCs, and PEG-30k-coated ICG-NCs (Fig. 5(a)-5(d)). The number of cells emitting fluorescence increased in response to incubation with uncoated ICG-NCs (Fig. 5(e)-5(f)), with the highest number of cells and the most intense signal emanating from macrophages incubated with freely dissolved ICG (Fig. 5(g)-5(h)).

2.3.3 Quantification of ICG Content within Macrophages

In Fig. 6, we present results that display the ICG content of human spleen macrophages incubated with PEG-5k-coated ICG-NCs, PEG-30k-coated ICG-NCs, uncoated ICG-NCs and free ICG for 30 minutes and two hours. The highest ICG content was associated with macrophages incubated with free ICG for both incubation times. The content of PEG-5k-coated ICG-NCs by the human spleen macrophages was significantly lower than that of PEG-30k-coated (p-value<0.05) and uncoated ICG-NCs (p-value<0.005) for up to 120 minutes of incubation time. The content of PEG-30k-coated ICG-NCs was significantly higher (p-value<0.05) than that of PEG-5k-coated ICG-NCs, but still lower than uncoated ICG-NCs (p-value<0.05).

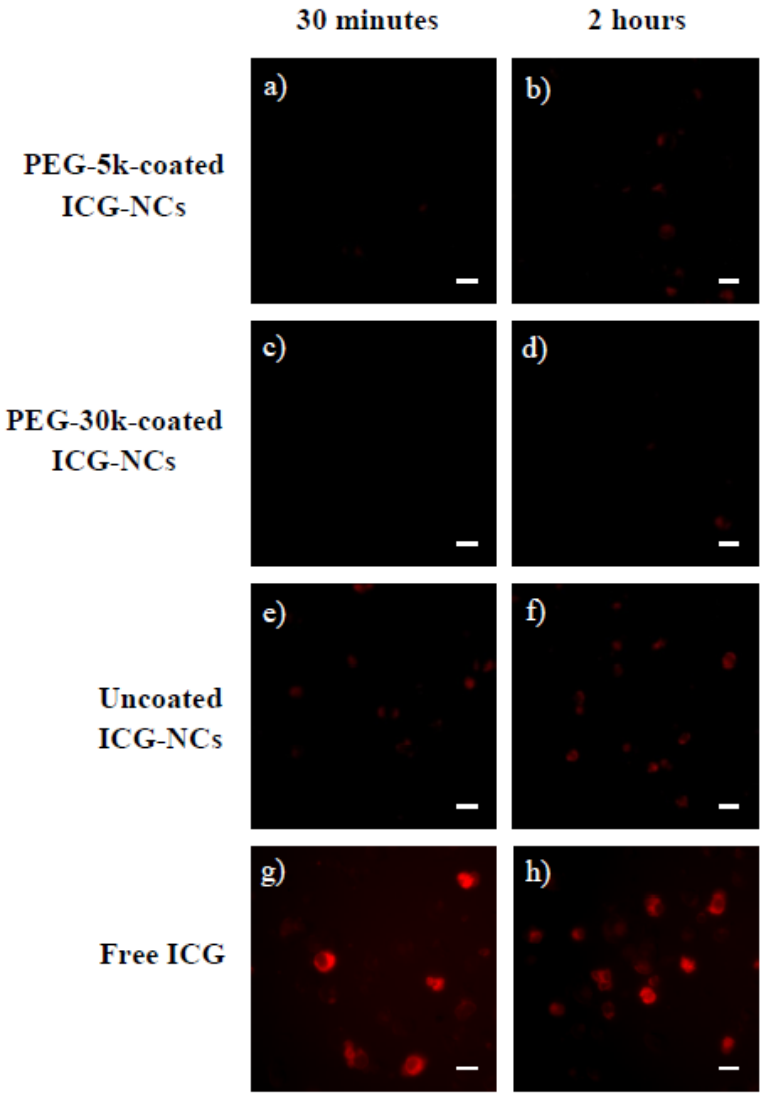

Figure 5 Fluorescent images of human spleen macrophages incubated with: (a,b) PEG-5k-coated ICG-NCs; (c,d) PEG-30k-coated ICG-NCs; (e,f) uncoated ICG-NCs; and (g,h) freely dissolved ICG in PBS, for 30 minutes and 2hours, respectively.

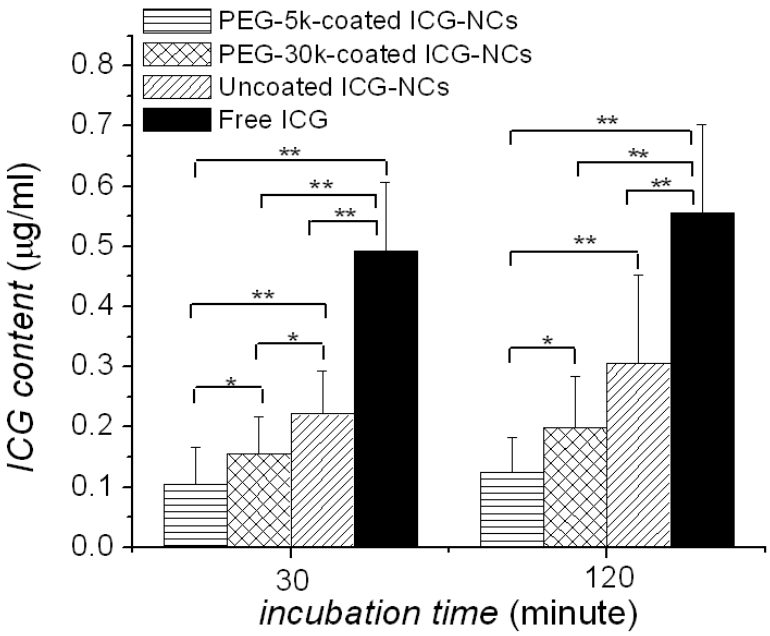

Figure 6 Mean ICG content of human spleen macrophages incubated with PEG-5k-coated ICG-NCs, PEG-30k-coated ICG-NCs, uncoated ICG-NCs and freely dissolved ICG in PBS for 30 and 120 minutes at 37 °C (cell density=5×10^5 cells/ml, n=7). Error bars on each panel represent the standard deviation. Single and double asterisks denote statistically significance differences between the shown pairs with p-value < 0.05, and p-value < 0.005, respectively.

2.3.4 Characterization of ICG-NCs Phagocytic Content

The population distribution of macrophages demonstrating various ICG fluorescent intensities after 15 minutes of incubation with free ICG or ICG-NCs, as determine by flow cytometry, are shown in Fig. 7(a). Macrophages incubated with free ICG exhibit the largest peak fluorescent value (≈1,600). For macrophages incubated with uncoated, PEG-30k-coated, or PEG-5k-coated ICG-NCs, the respective peak fluorescent values become progressively lower. These results suggest that the use of PEG-5k as the coating material tends to minimize the interactions between the spleen macrophages and ICG-NCs to result in reduced uptake level of the capsules for short incubation times (15 minutes). The MFI of macrophages incubated with free ICG and ICG-NCs between 15-

360 minutes are shown in Fig. 7 (b). For all incubation times, macrophages incubated with free ICG exhibited the highest MFI. Macrophages incubated with PEG-5k-coated ICG-NCs for up to 60 minutes had the lowest MFI values. Incubating the macrophages with PEG-coated ICG NCs resulted in significantly lower MFI values for up to 300 minutes as compared to cell that were incubated with uncoated ICG-NCs. For incubation times of two hours and longer, there were no significant difference in MFI values for PEG-5k and PEG-30k-coated ICG-NCs.

The content of ICG-NCs within the macrophages at any time is the sum of the uptaken capsules that are still intact plus the capsules that are undergoing degradation (partially degraded) and fully degraded capsules. With increased incubation time, all of these fractions may be present within the macrophages simultaneously. As ICG or ICG-NCs become degraded, it is likely that their fluorescence characteristics change to give rise to a net reduced MFI. For incubation times up to 60 minutes, the intact ICG-NCs appear to be the dominant fraction since the MFI values for macrophages incubated with either uncoated or PEG-coated ICG-NCs monotonically increase during this time interval (Fig. 7(b)). Beyond 60 minutes, the MFI values tend to fluctuate with incubation time, suggesting that all fraction types are likely to be present within the macrophages. Therefore, for long incubation time, the MFI will depend on the relative amount of each fraction type and its associated fluorescent emission characteristics.

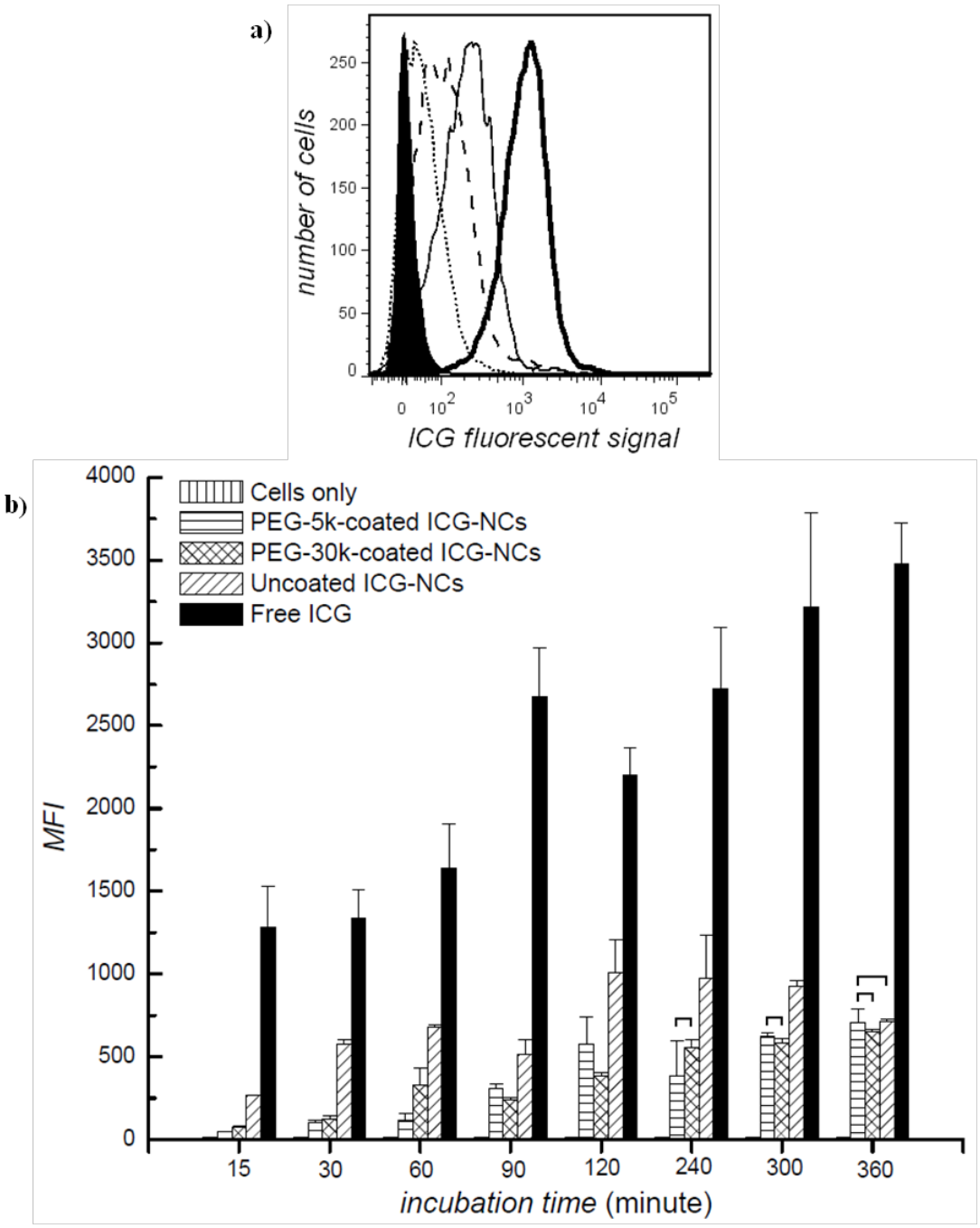

Figure 7 Characterizing the phagocytic content of ICG-NCs within macrophages by flow cytometry. (a) ICG fluorescent signal of macrophages incubated with free ICG (solid thick line), uncoated ICG-NCs (solid thin line), PEG-5k-coated ICG-NCs (doted line) and PEG-30k-coated ICG-NCs (dashed line) for 15 minutes. Cells not incubated with ICG or ICG-NCs were used as control (filled). (b) Mean fluorescent intensity (MFI) of macrophages (1×10^6 cells/well) after incubation with freely dissolved ICG, uncoated,

PEG-5k-coated, and PEG-30k-coated ICG-NCs for various times ranging from 15 minutes to 6 hours at 37 °C. Experiments were repeated three times, and 10,000 events were recorded for each sample. Brackets denote that there were no statistically significant differences between the shown bars.

In Fig. 8, we present the effect of ICG encapsulation and coating of ICG-NCs on the resulting side and forward scatterings by human spleen macrophages as determined with flow cytometry. Froward scattering is affected by the size of the cells, and side scattering by the granular content within the cells. Incubation with free ICG had minimal effect on forward and side scattering of macrophages as compared with the control cells (not incubated with any materials) (Fig. 8(b)). Therefore, uptake of ICG molecules did not alter size and granularity of macrophages. However, incubation of macrophages with uncoated ICG-NCs and PEG-coated ICG-NCs reduced the forward scattering, and slightly increased the side scattering (Fig. 8(c-e)). Reduced side scattering of macrophages incubated with ICG-NCs can be result of cytoplasmic granularity due to endocytosis of ICG-NCs.[77]

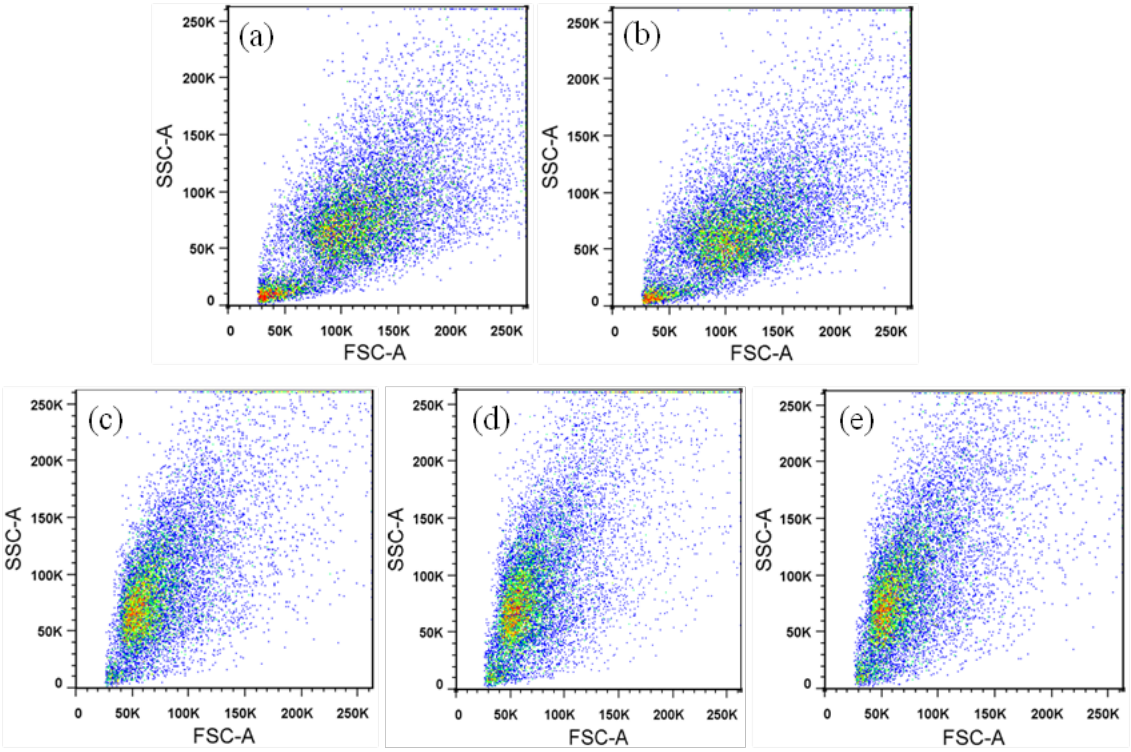

Figure 8 Integrated intensity of side scattering light with respect to time (SSC-A) *vs.* forward scattering (FSC-A) for human spleen macrophages: (a) negative control (cells only), and cell incubated with (b) free ICG, (c) uncoated ICG-NCs, (d) PEG-5k-coated ICG-NCs, and (e) PEG-30k-coated ICG-NCs.

The fluorescent intensity distribution of macrophages incubated with free ICG, uncoated ICG-NCs, PEG-5k-coated ICG-NCs, and PEG-30k-coated ICG-NCs for 15 minutes, 1, 4, and 6 hours are presented in Fig. 9 (a-d). The most intense peak in all different incubation times was associated with cells incubated with free ICG. The fluorescent intensity distribution of cells incubated with PEG-5k-coated ICG-NCs was the closest to the control sample (macrophages not incubated with free ICG or ICG-NCs) for up to one hour, suggesting that these constructs were least uptaken by macrophages. For four hours of incubation, the fluorescent intensity distribution of macrophages incubated with PEG-coated ICG-NCs became more comparable with that of macrophages

incubated with uncoated ICG-NCs. After six hours of incubation, macrophages incubated with uncoated or PEG-coated ICG-NCs had similar fluorescent intensity distributions, suggesting that ICG-NCs content of macrophages were similar at this time.

The percentage of ICG positive macrophages incubated with various constructs are shown in Fig. 9 (e). After 15 minutes of incubation, almost 95% of the cells had taken up free ICG. For macrophages incubated with uncoated ICG-NCs and PEG-coated ICG-NCs for 15 minutes, the percentage of ICG positive cells was reduced to less than 25% and 5%, respectively. The percentage of cells taking up PEG-5k-coated ICG-NCs remained less than 10% for up to one hour of incubation. For incubation times of two hours and longer, the uptake of PEG-5k coated ICG-NCs and PEG-30k-coated ICG-NCs were not statistically different from each other, but significantly lower than uptake of uncoated ICG-NCs and free ICG.

The results of flow cytometry experiments (Fig. 7(b) and 9(e)) are consistent with those obtained by cell lysis followed by optical absorbance measurements (Fig. 6) with the exception of the content of PEG-5k- and PEG-30k-coated ICG-NCs at two hours of incubation relative to each other. In the latter method, content quantification of ICG-NCs is based on the optical absorbance of ICG within the cell that includes the amount liberated from the intercellular phagocytic compartments after cell lysis. In flow cytometry studies, macrophages remain intact, and the measured MFI is related to the emission characteristics of internalized but not degraded ICG-NCs as wells as the degraded capsules and those undergoing degradation.

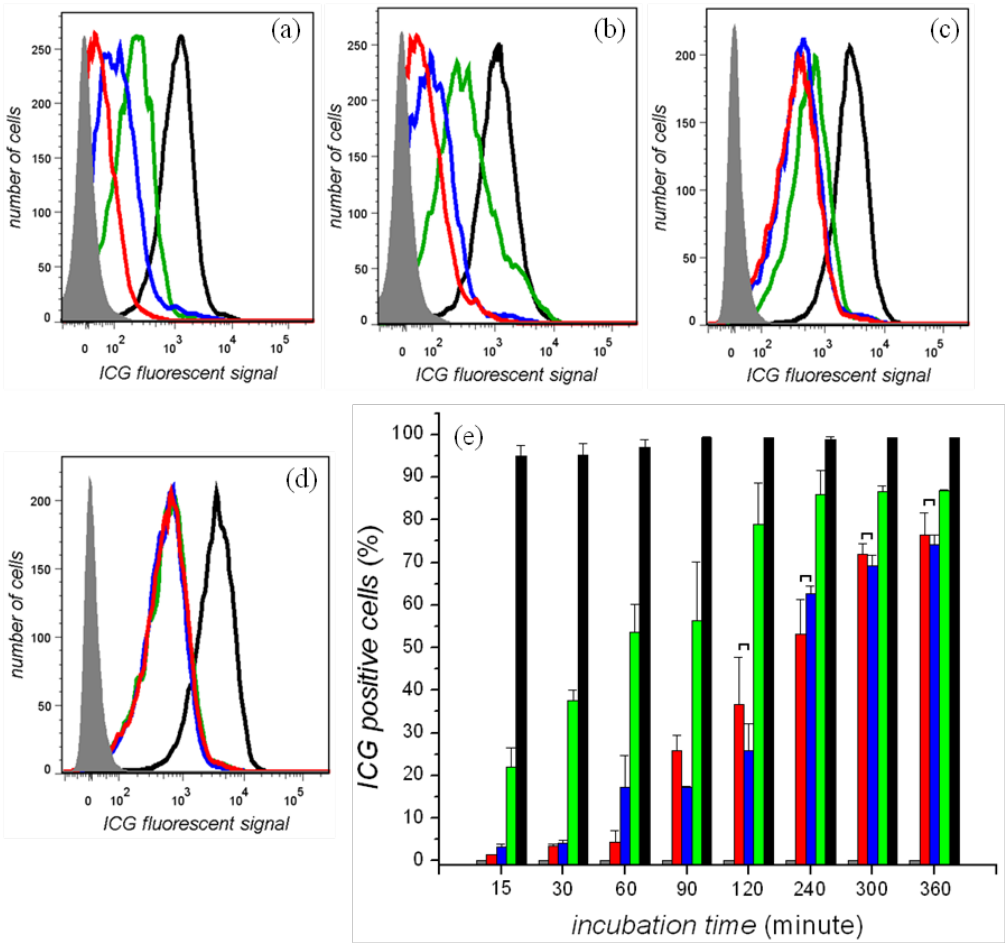

Figure 9 Fluorescent intensity distribution of human spleen macrophages incubated with free ICG (black histogram), uncoated ICG-NCs (green histogram), PEG-5k-coated ICG-NCs (red histogram), PEG-30k-coated ICG-NCs (blue histogram), and negative control (cells only, gray histogram) for different incubation times (a) 15 minutes, (b) 1 hour, (c) 4 hours, and (d) 6 hours. In panel (e), percentage of ICG positive cells for different incubation times are presented. Each bar represents the mean fluorescent intensity and each flow cytometry experiment was repeated three times. Error bars represent the standard deviation. Brackets denote that there were no statistically significant differences (p-value<0.05) between the shown bar pairs.

The statistically significant difference in content of PEG-5k and PEG-30k coated ICG-NCs within macrophages (Fig. 6) may be attributed to differences in conformation of PEG chains on the surface of nanocapsules. Due to the large surface curvature of the nanospheres compared to flat surfaces, an increase in the length of the PEG polymers will

provide conformational freedom at their distal termini that interfaces with the surrounding physiological media. Hence, as the PEG's MW increases, the conformation of PEG chains alters from brush-like structure to a mushroom-like arrangement. The protein resistivity of a PEGylated surface with either of these conformations is different. It has been reported that the brush-like conformation can reduce protein adsorption more as a result of higher entropic repulsion between proteins and the surface.[69,70] In low MW PEG, the chains on the surface are extended away from the surface and their mobility and flexibility is higher. However, in the mushroom conformation, PEG chains are more entrapped together and flexibility is reduced. In both conformations, the PEG layer can prevent penetration of large opsonins. The small opsonins can pass through PEG-30k layer easier due to the restricted range of motion of PEG chains compared to PEG-5k layer.[78]

The amount of ICG-NCs in macrophages also showed a correlation with the ζ-potential of the particles. Specifically, the greatest content was associated with uncoated ICG-NCs, which had the highest positive ζ-potential (≈+40 mV peak value). The content level decreased with PEG-5k-coated ICG-NCs and PEG-30k-coated ICG-NCs, which had lower peak ζ-potential values of approximately +12 and -7 mV, respectively. Our results are consistent with reports by Li & Huang,[18] Owens et al.[19] and Levch[78] that indicate reduced uptake of PEGylated liposomes and nanoparticles by macrophages. Li & Huang have reported rapid clearance of positively charged nanoparticles from vasculature with high accumulation levels in lungs and liver.[18] When liposomes were coated with PEG or

neutralized (-10 mV < ζ-potential < 10 mV), their uptake by RES cells was lowered, and their blood circulation half-life increased.[18]

Our results are very encouraging in that they suggest PEG-coated ICG-NCs may be used as a platform to increase the circulation time of ICG within the vasculature as result of reduced interaction with human macrophages. Such a platform can potentially be used for NIR imaging and phototherapy of vascular malformations, as well as tissue abnormalities when further enhanced with surface-expressed targeting moieties.

2.3.5 Interaction of ICG and ICG-NCs with human hepatocytes

The interaction of PEG-coated ICG-NCs with normal human hepatocytes was investigated for different incubation times from 15 minutes to 2 hours (Fig. 10). Hepatocytes incubated with freely dissolved ICG showed the highest MFI compared to uncoated and PEG-coated ICG-NCs. There was no statistically significant deference between MFI of hepatocytes incubated with PEG-5k-coated ICG-NCs, PEG-30k-coated ICG-NCs and the control sample for short incubation times (15 minutes). Up to two hours, the lowest MFI was associated with hepatocytes incubated with PEG-5k-coated and PEG-30k-coated ICG-NCs. However, uptake of PEG-5k-coated was not significantly different than that of PEG-30k-coated ICG-NCs. These results indicate that encapsulation of ICG in the nano-scale polymeric capsules and PEGylation diminishes the hepatic uptake of ICG *in-vitro*.

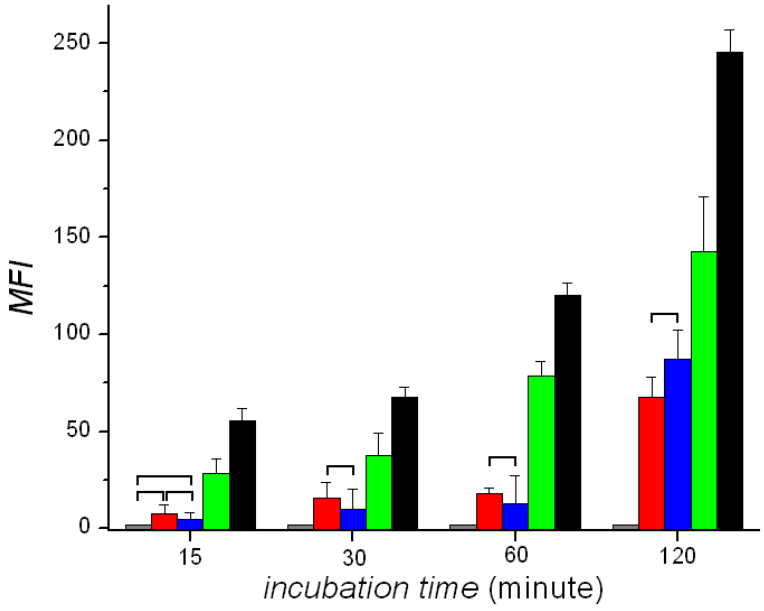

Figure 10 Mean fluorescent intensity of human hepatocytes incubated with free ICG (black), uncoated ICG-NCs (green), PEG-5k-coated ICG-NCs (red), PEG-30k-coated ICG-NCs (blue), and cells only as negative control (gray) for 15 minutes, 30 minutes, 1 hour and 2 hours. Each bar represents the MFI and each flow cytometry experiment was repeated three times. Error bars represent the standard deviation. Brackets denote that there were no statistically significant differences (p-value<0.05) between the shown bar pairs.

2.4 CONCLUSION

The surface of ICG-containing nanocapsuels (ICG-NCs) were successfully coated with aldehyde terminated PEG via reductive amination. PEG coating decreased the ζ-potential of ICG-NCs from high positive values to less positive potentials. Increased molecular weight (MW) of PEG from 5,000 to 30,000 Da resulted in further reduction of the ζ-potential towards the negative values. In comparison with free ICG and uncoated ICG-NCs, coating the surface of the capsules with PEG minimized the phagocytic content of ICG-NCs for up to 300 minutes, as characterized by statistically significant

reductions in the mean fluorescent intensity values. The phagocytic content of ICG-NCs was reduced through PEGylation. Low molecular weight PEG (5,000 Da) lowered the ICG-NCs content within human spleen macrophages up to 90 minutes as compared with the high molecular weight PEG (30,000 Da). For longer incubation times, there was no statistically significant difference in phagocytic content of ICG-NCs coated with either the high or low molecular weight PEG. Encapsulation within the polymeric nanocapsules reduced the hepatic content of ICG with normal human hepatocytes up to two hours, while the molecular weight of PEG did not have a statistically significant effect on the content of ICG-NCS in liver cells. Results of these *in-vitro* studies indicate the promising role of PEG coating as a method to prolong the vascular circulation time and reduce the clearance of ICG-NCs by RES.

CHAPTER 3: Effects of Nano-encapsulation and PEGylation on Biodistribution of Indocyanine Green in Healthy Mice: Quantitative Fluorescence Imaging and Analysis of Organs

3.1 INTRODUCTION

Nano-constructs containing near-infrared (NIR) exogenous chromophores are currently investigated as enabling platforms for site-specific optical imaging.[79–81] Use of NIR wavelengths is particularly advantageous in that it allows for relatively deep optical penetration, on the order of a few centimeters, in biological tissues due to reduced light absorption by water, and proteins.[82] Additionally, tissue autoflourescence is negligible over the NIR spectral band, allowing for increased contrast when using exogenous NIR fluorophores.[83,84]

We have engineered polymeric nanocapsules composed of Polyallylamine hydrochloride (PAH) chains cross-linked with sodium phosphate, and doped with Indocyanine green (ICG), the only FDA approved NIR chromophore for specific imaging applications.[11,13,73,85,86] For example, in ophthalmology, ICG is used to image the nature of choroidal circulation and its abnormalities including suspected polypoidal choroidal neovascularization, choroidal hemangioma, chronic central serous chorioretinopathy, and certain forms of neovascularization in age-related macular degeneration.[87–89] Other clinical applications of ICG are in assessment of cardiovascular and liver functions.[90,91] ICG has also been investigated in patients with breast, gastric, and skin cancer undergoing sentinel lymph node mapping,[92–98] and evaluation of lymphedema.[99,100]

Despite its proven efficacy in these applications, the utility of ICG for broader clinical usage has been limited due to its non-specific binging to albumin and high-density lipoproteins (HDLs) in plasma. Such binding results in rapid clearance of ICG from blood (with plasma half-life on the order of 2-4 minutes).[101] Others[10,54,102,103] and we[11,13,73,85,86] are pursuing encapsulation of ICG as a potential approach to increase its circulation time with the intention of broadening the medical applications of this clinically-proven optical material.

A common phenomenon associated with use of exogenous nano-constructs is that once administered into the vasculature, blood plasma proteins can bind to the surface of these materials. Macrophages of the reticuloendothelial system (RES) recognize the nanoparticles by the presence of these surface adsorbed proteins, and clear them from the vasculature through phagocytosis.[104] Circulation time of nanoparticles within the vasculature can be improved by minimizing non-specific protein binding and phagocytic recognition. Development of bioinert (non-fouling) surfaces that resist protein adsorption is a common strategy to prolong vascular circulation time of nanoparticles.[105]

Here, we modify surface of ICG-NCs with polyethylene glycol (PEG) as an approach to increase the circulation time of the constructs. In a previous study, we demonstrated that PEGylating the ICG-NCs reduced the uptake of the constructs by primary human hepatocytes in-vitro.[106] We have also investigated the effect of low (5 KDa) and high (30 KDa) molecular weight (MW) of PEG coating, and determined that coating the surface of ICG-NCs with 5 KDa PEG reduces the interaction between the particles and spleen macrophages, as determined by flow cytometry.[86] Motivated by these

previous in-vitro studies, herein, we extend our investigations to in-vivo studies using healthy mice. Specifically, the objectives of this study are to: (1) evaluate the effectiveness of encapsulation and coating the surface of ICG-NCs with 5 KDa PEG in extending the circulation time of ICG; and (2) investigate the utility of these ICG-NCs for in-vivo quantitative fluorescence imaging.

3.2 MATERIALS AND METHODS

3.2.1 Synthesis and PEGylation of ICG-NCs

We synthesized ICG-NCs by ionic cross-linking of the PAH chains with sodium phosphate, and subsequent diffusion-mediated ICG loading, as reported previously.[11,13,15,73,85,86,107] The amounts of PAH and sodium phosphate, and the aging time control the size of the ICG-NCs.[73] In this study, we fabricated the ICG-NCs by mixing 20 μl of PAH stock solution (2 mg/ml, 4 °C) and 10 μl of disodium hydrogen phosphate heptahydrate solution (0.01 M, 4 °C). The nanoparticle suspension was then diluted by addition of 1.2 ml pre-cooled deionized water (4 °C), immediately followed by addition of 240 μl of ICG aqueous solution (0.65 mM, 4 °C). The ICG-NCs suspension was aged for 15 minutes at 4 °C, and then washed through differential centrifugation. The suspension was centrifuged at 2,300g (5,000 rpm) for 5 minutes followed by another centrifugation at 845g (3,000 rpm) for 30 minutes to separate large ICG-NCs. Then, ICG-NCs suspension was washed twice at 845g for 2 hours.

ICG-NCs were subsequently coated with aldehdye-terminated PEG (PEG-ALD, MW=5,000 Da) using reductive amination as described before.[86] The PEG-ALD was

added to the ICG-NCs suspension to yield conjugation of one PEG chain/nm^2 of nanoparticle surface. We used approximately two equivalents of sodium dithionite, as reducing agent, per mole PEG-ALD. This suspension was then aged for two hours at 4 °C. This process results in formation of a covalent bond between the amine groups on the surface of ICG-NCs and the aldehyde group of the PEG-ALD. The PEG-coated ICG-NCs were washed through centrifugation twice (845g, 2hours). The uncoated and PEG-coated ICG-NCs were resuspended in PBS and stored at 4ºC in the dark.

3.2.2 Characterization of ICG-NCs

The morphology of ICG-NCs was determined using scanning electron microscopy (SEM, Philips, XL-30 FEG). Hydrodynamic diameters of the uncoated and PEGylated ICG-NCs were measured by dynamic light scattering (DLS) (Zetasizer Nanoseries, NanoZS90). Absorption spectra of ICG-NCs were obtained using a UV-Visible spectrophotometer (Cary 50 UV-Vis spectrophotometer) with a 1 cm path-length. Fluorescence spectra of ICG-NCs were obtained with a fluorometer (Jobin-Yvon Fluorolog) in response to 680 nm excitation wavelength, a wavelength at which both non-PEGylated and PEGylated constructs have nearly the same absorbance value. For comparison, we obtained the absorption spectrum of 9 μM ICG dissolved in water, and its corresponding fluorescence spectrum in response to 680 nm excitation.

3.2.3 Cytotoxicity Assessment

We incubated Human Dermal Microvascular Endothelial Cells (HDME, PCS-110 cell line) purchased from American Type Culture Collection (ATCC) with media

containing uncoated ICG-NCs (4.6 μg PAH/ml), PEG coated ICG-NCs (4.6 μg PAH/ml), or PAH (at 6 and 12 μg/ml) for 24 hours at 37 °C and %5 CO_2. Cells without exposure to any agent, and those incubated with phenol (100 μl) were used as negative and positive controls, respectively. After 24 hours, cells were washed twice with PBS and stained with propidium iodide (PI) to identify the dead cells. We used flow cytometry to determine the percentage of dead cells.

3.2.4 Animal Preparation and Administration of Imaging Agents

Female Swiss Webster mice, 25-30 g, 10-12 weeks old, were procured from Charles River Laboratories, and utilized in this study under a protocol (A-20080039) approved by UC Riverside Institutional Animal Care and Use Committee. Animals were anesthetized by inhalation of 2% Isoflurane in Oxygen. The ventral side of each mouse was shaved one hour prior to administration of ICG-NCs. The PEG-coated ICG-NCs, uncoated ICG-NCs, or freely dissolved ICG were administered intravenously via tail vein injection while the animal was anesthetized. The absorbance values of all samples at 800 nm were the same, and equivalent to the value associated with 12 μM of free ICG. The administered level of ICG in our experiments, 75 μg ICG/kg weight of mouse, is well below the LD50 (lethal dosage in 50% of animals) of 62 mg/kg in mice.[108] The injection volume for all samples was 150 μL.

3.2.5 Whole-Body Fluorescence Imaging

Whole-body images of the mice were captured using a luminescence dark box. The animal was placed in a supine position on a heating pad to maintain body

temperature. A constant flow of 2% Isoflurane in Oxygen was delivered using a plastic gas manifold during the imaging to immobilize the mice. Images were captured at various times and up to 60 minutes post injection of samples. Two LEDs equipped with an excitation filter (700 ± 30 nm) were used for illumination. Fluorescent emission was captured using a CCD Camera (Pixis 1024B, Roper Scientific) equipped with a long pass filter transmitting wavelengths greater than 810 nm. To prevent pixel saturation, the respective camera exposure times were set to 0.5 s for animals injected with free ICG, and 1.0 s for animals injected with other agents.

3.2.6 Quantitative Image Analysis

The acquired fluorescent images were analyzed using ImageJ software. The abdominal area of the mouse, corresponding to the liver and small intestine, was selected as the region of interest (ROI). The mean intensity (I) values of each fluorescent image acquired from the ROI at different post injection times were calculated as:

$$\bar{I} = \frac{\sum_{j=1}^{m} I_j}{m}$$

where m is the total number of pixels in the ROI, and I_j is the pixel intensity at j^{th} pixel. Subsequently, we computed the image contrast (C) associated with the ROI as:

$$C = \frac{\bar{I}_T - \bar{I}_B}{\bar{I}_B}$$

where $\bar{I}_T$ and $\bar{I}_B$ present the mean intensity of the ROI (abdominal area) and background, respectively.[85,109]

3.2.7 Biodistribution Characterization

Mice were euthanized by inhalation of compressed CO_2 gas at various times (15, 30 and 60 minutes) following injection with PEG-coated ICG-NCs, uncoated ICG-NCs, or freely dissolved ICG. Five mice were studied for each of the imaging agents and each time point, giving a total of 45 animals. After sacrificing each mouse, 500 μl of blood was collected from the heart by cardiac puncture. The blood sample was mixed with 5 ml of sodium dodecyl sulfate (SDS, 5% w/v in water) solution to lyse the blood cells, and release the ICG molecules or nanocapsules taken up by the cells. Various organs including heart, lungs, liver, kidneys, spleen, stomach and intestine were harvested at each time point and for each imaging agent. Organs were ground using disposable polystyrene tissue grinders (Fisherbrand). Smaller organs, such as heart, spleen, lungs, and kidneys, were incubated in 5 ml of SDS solution for one hour to lyse the cells. Liver, intestine and stomach were incubated in 10 ml of SDS solution (5% w/v in water) for one hour.

Lysed organs and blood samples were centrifuged in SDS solution at 12,000g (9,000 rpm) for 30 minutes at 4ºC. Subsequently, the supernatants of the blood sample and homogenized organs were collected, and the fluorescence emission spectrum of each sample was recorded using a fluorometer (Jobin-Yvon Fluorolog) in response to 680 nm excitation wavelength. The ICG content within each organ was calculated by comparing the integrated fluorescent signal (over 700-900 nm bandwidth) with a calibration curve that related the fluorescence emission over the same bandwidth to various concentrations of ICG in SDS solution.

3.3 RESULTS AND DISCUSSION

3.3.1 Characterization of ICG-NCs

An illustrative scanning electron microscopy (SEM) image shows the spherical morphology of ICG-NCs (Fig. 11(a)). Using DLS, the peak diameter of the uncoated ICG-NCs, based on the amounts of the reagents utilized, again time, and other experimental protocols as indicated in the Methods section, was 77 nm (Fig. 11(b)). PEGylation increased the peak diameter by nearly 10 nm, and resulted in a right shift in the population distribution. Both peak values were associated with 23% of the nanoparticles in the population distribution.

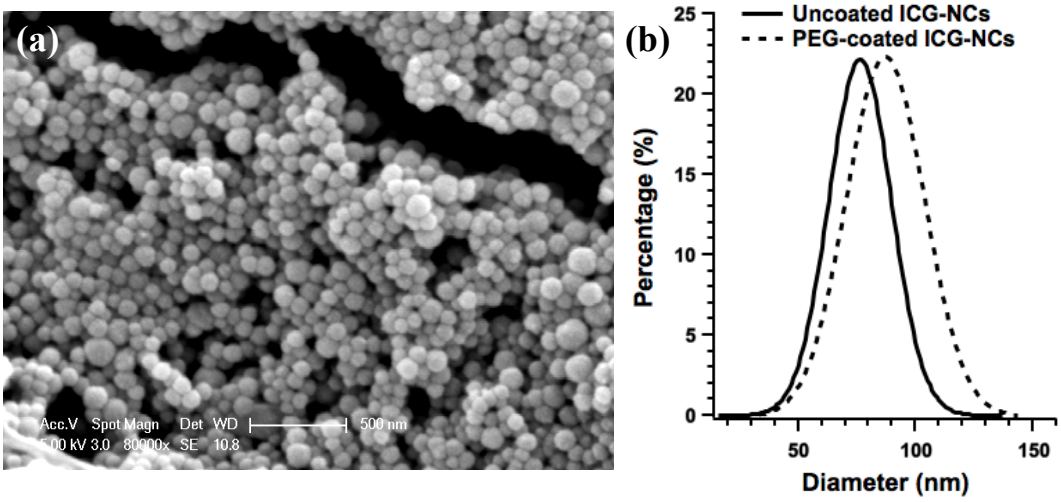

Figure 11 (a) SEM image of uncoated ICG-NCs, and (b) Gaussian fits to the size distribution profiles of uncoated and PEGylated ICG-NCs in water at 4 °C as measured by DLS.

In comparison to the absorption spectrum of free ICG, the spectra of ICG-NCs were broadened, and did not show distinct peaks corresponding to the monomeric and dimeric forms of ICG at 780, and 720 nm, respectively. This spectral broadening is consistent with our previous report.[73] Uncoated and PEG-coated ICG-NCs demonstrated

similar absorption and fluorescent emission spectra (Fig. 12), suggesting that PEGylation did not profoundly change these optical properties of the constructs. Absorbance values were slightly higher for the PEGylated particles in the 700-860 nm range (Fig. 12(a)). In response to 680 nm excitation, the fluorescence spectra for both uncoated and PEG-coated ICG-NCs illustrated peaks at nearly 720 and 790 nm, corresponding to emission from the dimeric and monomeric forms of ICG, respectively, with slightly higher values for the PEGylated constructs in the 720-730 nm and 750-805 nm emission bands.

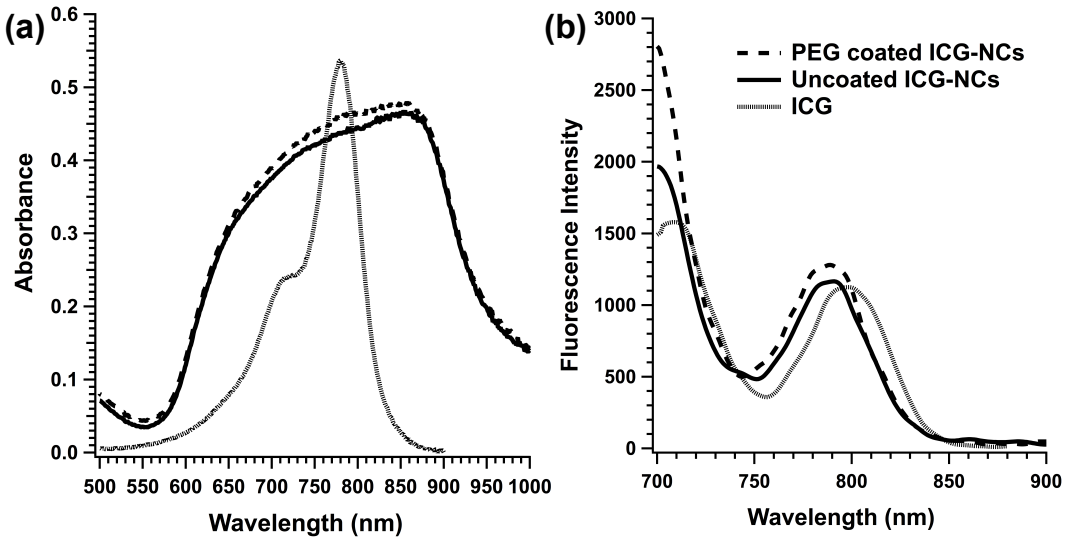

Figure 12 (a) Absorbance and (b) fluorescence spectra of ICG (9 μM), uncoated and PEG-coated ICG-NCs (λ_{ex}=680 nm).

We have previously reported on improved optical and thermal stability of ICG when encapsulated in these polymeric nanocapsules.[11] For example, exposure of ICG-NCs suspension and free ICG to broadband light for up to 2 hours resulted in increased degradation rate of the monomer form of free ICG from 0.0142 min^{-1} to 0.0042 min^{-1}. In

response to incubation of ICG-NCs and free ICG at 40 °C for 48 hours, the absorbance of the monomer form of free ICG decreased by ≈40%. In contrast, the absorbance of the monomer form of ICG-NCs was reduced by only 10%.[11]

We have also reported the release kinetics of ICG from these polymeric nanoparticles.[15] We incubated ICG-NCs in Dulbecco's Modified Eagle Medium (DMEM) supplemented with 10% fetal bovine serum (FBS) for up to 24 hours at 37°C water bath (without light exposure) to simulate a physiologically relevant environment. At various time points, capsules were centrifuged, and the supernatants were collected and optically analyzed for ICG released from the capsules. Only 5% of ICG was released from the nanocapsules after one hour under these physiological relevant conditions. At eight hours post-fabrication, the released level approached a near steady value of approximately 12%.[15]

We have measured the zeta potential distribution of non-coated ICG-NCs (40 mV) and PEGylated ICG-NCs (12 mV). We have used FTIR spectroscopy to confirm covalent attachment of PEG to the surface of ICG-NCs using the reductive amination process.[86]

3.3.2 Cytotoxicity of ICG-NCs

In Fig. 13, we present preliminary cell viability studies using the PI assay. Almost 100% of the cells incubated with uncoated ICG-NCs, PEG-5k-coated ICG- NCs, and 6 μg/ml PAH remained viable. Cell viability was reduced to 85% after incubation with PAH at 12 μg/ml for 24 hours, while almost the entire cell population was dead when incubated with phenol. These results are very promising since they suggest that PAH will

not compromise the cell viability when utilized at concentration of less than 12 μg/ml. Therefore, for these in-vivo studies we administered ICG-NCs containing PAH at concentrations lower or equal to 4.6 μg/ml.

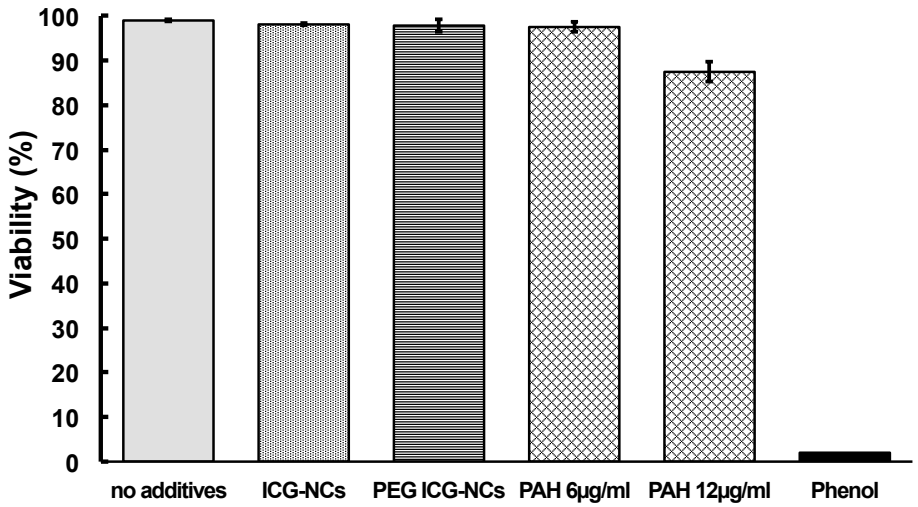

Figure 13 Viability of human dermal vascular endothelial cells after 24 hours incubation in media containing one of the following additives: uncoated nanocapsules doped with ICG (ICG-NCs, 4.6μg/ml); PEG coated nanocapsules doped with ICG (PEG ICG-NCs, 4.5 μg/ml); and polyallalamine hydrochloride (PAH) at two different concentrations. Incubation in media with no additive encompassed the negative controls; and incubation in the media with phenol provided the positive controls. Each bar represents average of three experiments. Error bars represents one standard deviation. Using statistics to analyze the results for ICG-NCs and PAH (6μg/ml) yielded p-values larger than 0.1 when compared with the negative controls and p-values smaller than 10^{-4} when compared with the positive control. Therefore, these three tests indicated for lack of the adverse effect on cell viability. The same analysis for PAH at 12μg/ml (which is 2.6 times more than the concentration administered in in-vivo studies) yielded p-values smaller than 10^{-3} when compared to the negative control and p-value smaller than 10^{-4} when compared with positive control.

3.3.3 Quantitative Fluorescence Imaging and Biodistribution of Constructs in Mice

Maximum fluorescence signal associated with injection of free ICG was detectable from the liver three minutes post-injection (Fig. 14(a)), indicating the rapid

clearance of ICG from the systemic circulation, consistent with previous studies.[5,50,110] Fluorescence emission levels from the liver remained near maximum for at least 60 minutes post-injection with free ICG (Fig. 14(b)-14(e)). In the case of uncoated and PEG-coated ICG-NCs, maximum fluorescence signals from the liver were detectable at 10 minutes (Fig. 14(g)) and 60 minutes (Fig. 14(o)) post-injection, respectively.

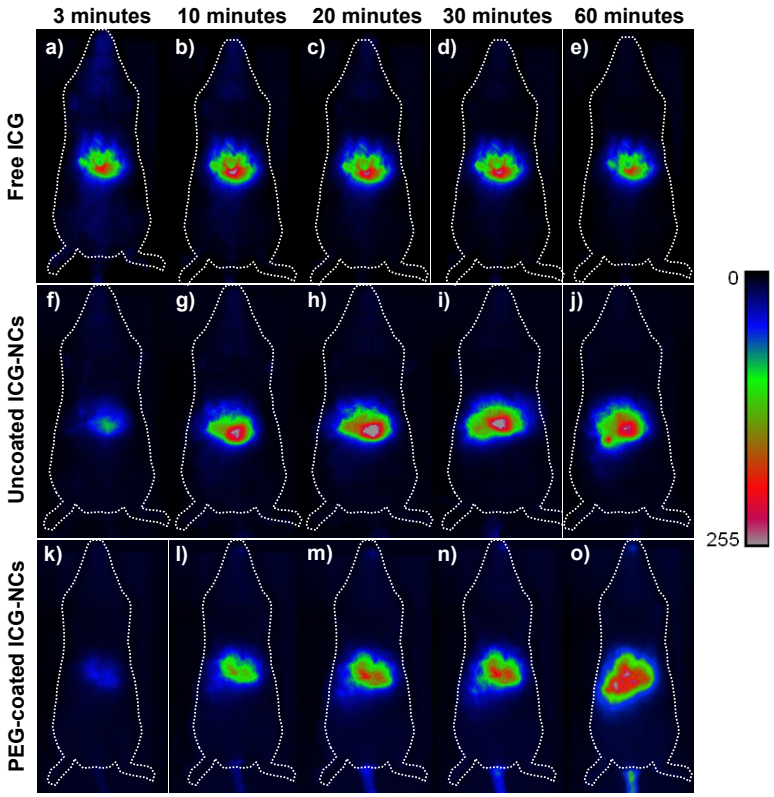

Figure 14 Whole-body fluorescent images of three different mice injected with freely dissolved ICG in PBS (a-e), uncoated ICG-NCs (f-j) and PEG-coated ICG-NCs (k-o) at various times post-injection.

We present the mean ± standard deviation values of the image contrasts (C) associated with the abdominal areas as the ROI at post-injection times between 3-60 minutes (Fig 15). The mean value of C was about eight-fold higher for mice injected with

free ICG as compared to that for mice injected with PEG-coated ICG-NCs at 3 minutes post injection.

We fitted the dynamics of the image contrast with single exponential profiles (Fig. 15), and define τ as the time over which the mean value of C increases by a factor of e. The mean value of C for the ROI increased rapidly up to approximately eight minutes post injection for free ICG (τ=1±0.06 minutes). The rapid increase of C demonstrates the quick accumulation of free ICG in the liver within a short time post-injection. ICG is secreted into the bile following uptake by the liver.[111] Consequently, bile that contains ICG is stored in the gallbladder, and discharged to the duodenum through the bile duct. After 10 minutes post-injection, the mean C value for the ROI associated with free ICG (Fig. 15) gradually decreased over a time interval greater than 60 minutes, suggesting either a reduced rate of accumulation in the liver or secretion of ICG to the bile, or both.

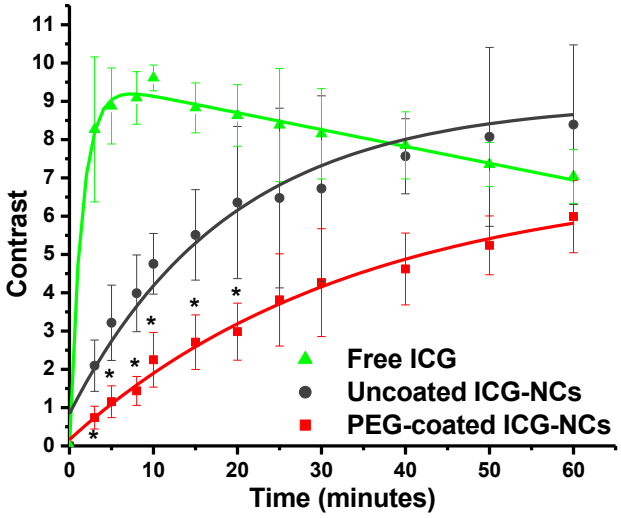

Figure 15 Computed image contrast of the abdominal area of mice injected with freely dissolved ICG in PBS, uncoated ICG-NCs and PEG-coated ICG-NCs at various times

post-injection. The exponential fit to each data set is presented as green (Free ICG, R^2=0.95), dark grey (uncoated ICG-NCs, R^2=0.96) and red (PEG-coated ICG-NCs, R^2=0.99). Error bars represent the standard deviation. Asterisks denote that there were statistically significant differences (p-value< 0.05) between the PEG-coated ICG-NCs and Uncoated ICG-NCs and free ICG contrast.

Upon injection of uncoated ICG-NCs, a different dynamic was observed; a gradual increase in the mean *C* value for the ROI up to 60 minutes post injection with τ=18.98±1.61 minutes. The longer τ of uncoated ICG-NCs compared to that associated with free ICG implies lower clearance rate of uncoated ICG-NCs from the systemic circulation and accumulation in the liver. The mean *C* value for the ROI associated with PEG-coated ICG-NCs gradually increased until 60 minutes post injection with a τ=34.2±1.39 minutes (Fig. 15). The mean *C* for mice injected with PEG-coated ICG-NCs remained statistically significantly lower than the corresponding values for mice injected with uncoated ICG-NCs and free ICG for up to 20, and 50 minutes post-injection, respectively. The lower mean values of *C* and longer τ associated with PEG-coated ICG-NCs, imply reduced accumulation of PEGylated ICG-NCs within the liver; an indication of prolonged circulation time of these nanoparticles.

We present illustrative fluorescent images of various organs obtained from six mice euthanized at 30 and 60 minutes post-injection (Fig. 16). For mice injected with free ICG, only the liver and intestine could be fluorescently visualized, confirming that these are two organs in which free ICG is accumulated (Fig. 16(a) & 16(b)). For mice injected with uncoated ICG-NCs, fluorescence emission from the liver, intestine, stomach, spleen and kidneys were detectable at 30 minutes post-injection. At 60 minutes post-injection of

uncoated ICG-NCs, the presence of ICG in only the liver, intestine and stomach could be fluorescently detected (Fig. 16(c) & 16(d)). However, for mice injected with PEG-coated ICG-NCs, all organs except heart were distinguishable in the fluorescent images at 30 and 60 minutes post injection (Fig. 16(e) & 16(f)). The fluorescence emission detected from the highly vascularized organs including spleen, lungs and kidneys up to 60 minutes post-injection of PEG-coated ICG-NCs may be due to the circulating PEG-coated ICG-NCs within the vasculature or tissues of these organs.

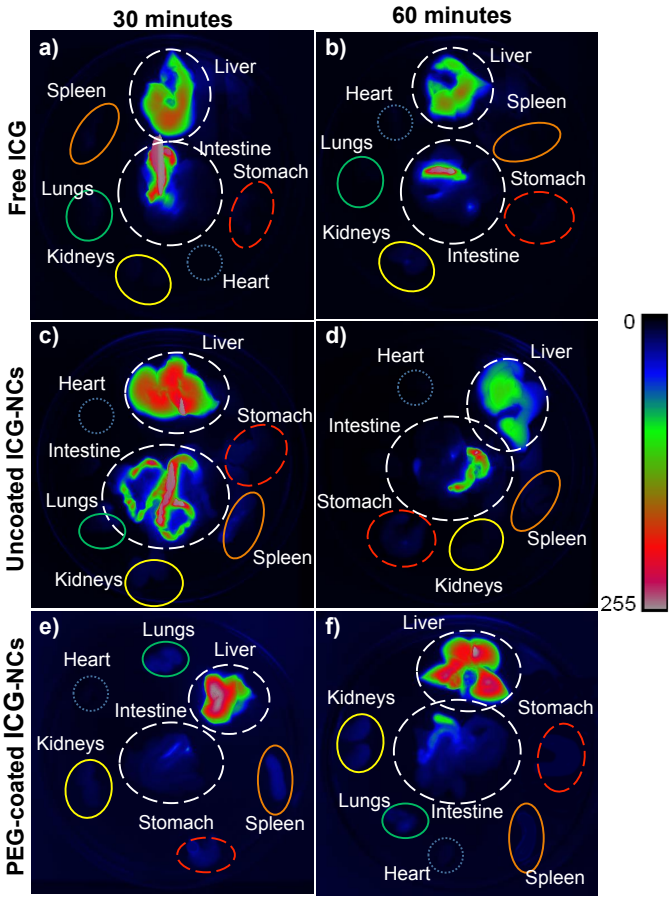

Figure 16 Fluorescent images of harvested organs of six mice at 30 and 60 minutes post tail vein administration with free ICG (a,b), uncoated ICG-NCs (c,d) and PEG-coated ICG-NCs (e,f).

3.3.4 Quantification of ICG Content in Blood Sample and Harvested Organs

We determined the relative ICG content of blood and various organs at three different post-injection times of 15, 30 and 60 minutes (Fig. 17). Nearly 57% of administered PEG-coated ICG-NCs remained within the vasculature at 15 minutes post-injection (Fig. 17(a)). This fraction was approximately three-fold higher than those for uncoated ICG-NCs and free ICG. The remainder of PEG-coated ICG-NCs was mostly recovered from the liver (12%), lungs (6.5%), kidneys (5.7%), spleen (4%), heart (3%) and intestine (1.7%).

The majority of administered free ICG was recovered from blood (21.5%), intestine (21%) and liver (14%) at 15 minutes post injection. Based on the high level of ICG recovered form the intestines, we suggest that the passage of free ICG from the liver to the small intestine occurs as early as 15 minutes post-injection (Fig. 17(a)).

The ICG content in blood dropped for all three agents at longer post-injection times; nevertheless, the level of PEG-coated ICG-NCs in blood remained significantly the highest at 15, 30 and 60 minutes post-injection as compared to uncoated ICG-NCs and free ICG. The ICG content within blood at 30 minutes post-injection of PEG-coated ICG-NCs (Fig. 17(b)) was nearly equal to blood ICG content, 15 minutes post-injection of free ICG or uncoated ICG-NCs (Fig. 17(a)).

At 30 minutes post injection, the amount of ICG in blood and liver dropped dramatically to 7% and 6% respectively (Fig. 17(b)); conversely an increase in ICG content of the intestine to 41% was observed. This rise is indicative of ICG transport to the duodenum. In case of uncoated ICG-NCs, the amount of ICG recovered from blood,

heart and kidneys dropped to 6.8%, 0.3% and 4.4%, respectively. However, the ICG content remained the same in lungs and spleen. A significant increase in ICG concentration was observed in intestine and liver at longer post injection times of uncoated ICG-NCs (Fig. 17(b) & 17(c)).

At 30 and 60 minutes post-injection of PEG-coated ICG-NCs, the amount of ICG dropped significantly in blood and all organs except the liver and intestine (Fig. 17(b) & 17(c)). The dramatic increase in liver ICG content from nearly 12% at 15 minutes to 22% at 30 minutes, and 42% at 60 minutes post-injection is consistent with the whole-body fluorescent images (Fig. 14) and the associated ROI image contrast (Fig. 15), and illustrates the delayed uptake of PEG-coated ICG-NCs by the liver. The recovered ICG amount from lungs, kidneys, spleen and heart decreased at 30 and 60 post injection times of PEG-coated ICG-NCs.

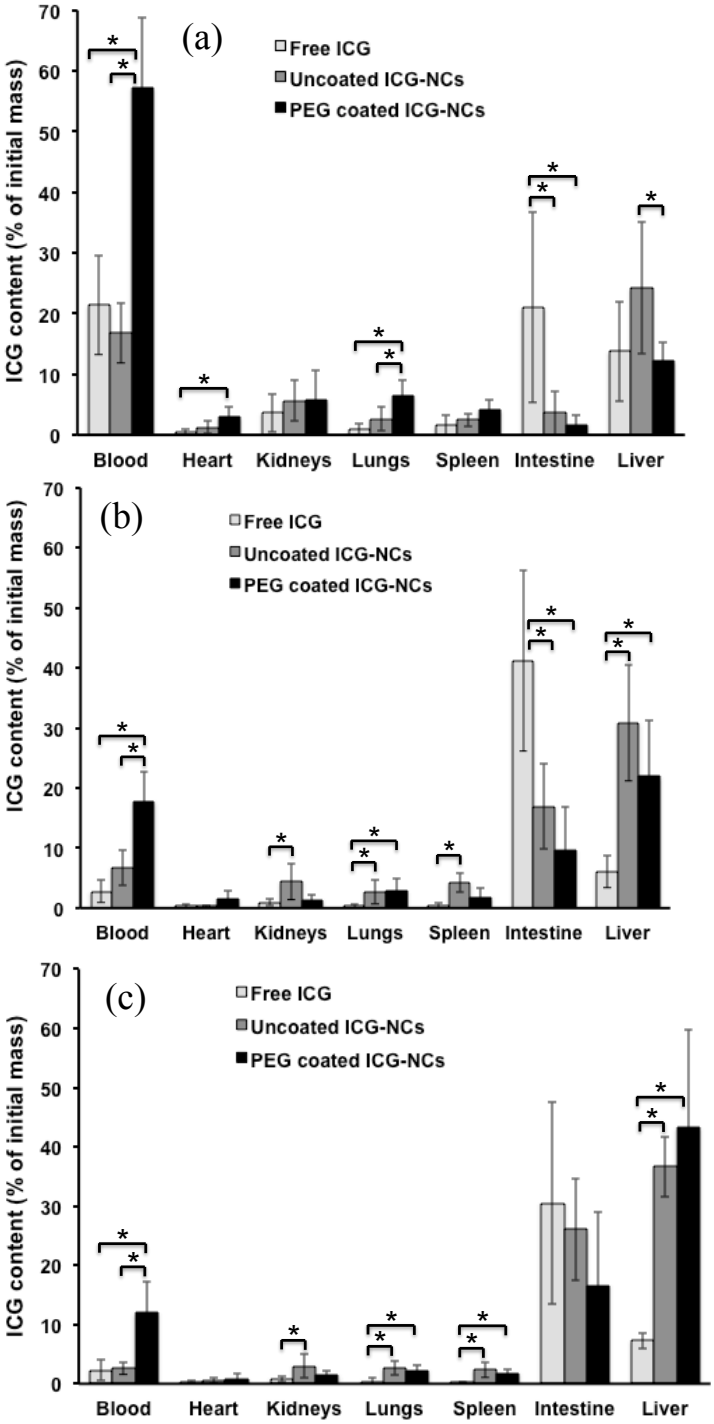

Figure 17 Estimated percentage of ICG recovered from blood, heart, kidneys, lungs, spleen, intestine and liver of the mice injected with freely dissolved ICG in PBS, uncoated ICG-NCs and PEG-coated ICG-NCs at (a) 15 minutes (b) 30 minutes and (c) 60 minutes post-injection. Each experiment was repeated 5 times. Error bars represent

standard deviation. Single asterisks denote statistically significance differences between the shown pairs with p-value < 0.05.

Spleen is one of the organs of the immune system responsible for filtering the foreign body materials, and dead or damaged erythrocytes from blood.[112] We note that about 4% of the PEG-coated ICG-NCs was recovered from spleen at 15 minutes post-injection. However, the recovered ICG level had a statistically significant reduction to 2% at 60 minutes post-injection. Therefore, we associate the high level of PEGylated ICG-NCs recovered from the spleen at 15 minutes post-injection to the nanoparticles circulating within the vasculature of spleen. In the open blood circulation system of the spleen, the capillaries discharge openly into the pulp cord before reaching the sinusoids. The pulp cords contain reticular cells, macrophages, plasma cells and lymphocytes.[113] The PEGylated ICG-NCs in the blood has to pass through the pulp cord before entering the venous sinusoids. We attribute the initial rise in fluorescent signal detected from spleen and the concentration of recovered nanocapsules from this organ to the portion of the PEG-coated ICG-NCs passing through the pulp cord and not to the uptake by splenic macrophages.

Lungs, as the organs receiving the entire cardiac output, are prone to nanocapsules accumulation.[114] Our results demonstrated that a statistically significant level of ICG was recovered from the lungs (6.5%) at 15 minutes post injection of PEG-coated ICG-NCs compared to uncoated ICG-NCs and free ICG (Fig. 17(a)). The drop in ICG content of the lungs to 2.5% after one hour of administering the PEG-coated ICG-NCs suggests that the particles were in the vasculature of the lungs.

Some features of our ICG-doped nanocapsules (ICG-NCs) are: (1) spontaneous self-assembly via green chemistry; (2) fabrication of capsules with tunable diameters in the range of ≈ 60 nm to 1 μm; and (3) the presence of amine groups on the surface of the constructs, which enables the covalent attachment of various moieties for molecular targeting.

To suppress the propensity of the ICG-NCs for non-specific adsorption of proteins, we coated them with PEG, which is widely used to produce bioinert surfaces by suppressing non-specific interactions.[115] To attain stability of the passivation coating, we covalently grafted the PEG chains to the amines on the surface of the nanoparticles. Employing chemical reactions that proceed through small intermediates with quantitative yields, such as reductive amination, ensures sufficiently well-packed PEG layers.[66]

The bioinertness of the PEG coatings strongly depends on the length of the polymer chains. Our goal encompassed not only suppressing molecular-level non-specific interactions, which can be achieved even with ethylene glycol oligomers (i.e., with 3 to 6 repeating ethylene glycol units), but also preventing non-specific adhesion at mesoscopic (micron and sub-micron) levels. Coatings of too short PEG polymers would not provide sufficient separation between the nanoparticle and surfaces, to which they have tendency for non-specific adsorption. Concurrently, too long PEG chains would result in layers in which the polymer termini have non-helical "mushroom" conformation that compromises the ability of such coatings to suppress non-specific interactions.[63] Using force measurements, as implemented with magnetic pullers, we previously determined that PEG with MW of 5 KDa, among the PEG molecules investigated with MW ranging

between 1-20 KDa, provided the optimal covalently grafted coatings for suppressing non-specific adhesion.[116] The higher flexibility and mobility of low MW PEG chains result in higher entropic repulsion between proteins and the surface.[69,70] Our in vitro studies confirmed the choice of PEG-5 KDa for passivation coatings of ICG-NCs and for impeding their uptake by macrophages.[86] Conversely, reduced flexibility of high MW PEG chains, due to the entrapment of long chains, induces low protein resistivity. Herein, we examine the biodistribution of ICG-NCs coated with passivation coating of PEG-5 KDa.

In previous studies by other groups, ICG-containing constructs composed of poly(DL-lactic-co-glycolic-acid) (PLGA) whose surfaces were functionalized by both PEG and folic acid were administered into tumor bearing mice.[117,118] While these studies demonstrate the efficacy of targeted fluorescence imaging of tumors using functionalized ICG-containing constructs, they cannot isolate the effects of ICG encapsulation, and the additional PEGylation of the constructs in the absence of targeting moieties such as the folic acid, in modulating the biodistribution of encapsulated ICG in a non-diseased mammalian system.

In another study by Zheng et al, ICG was entrapped within PLGA, and the construct in turn was coated with a lipid-2 KDa PEG-folic acid assembly.[118] Although the investigators report the utility of these structures in targeted fluorescent imaging of tumor bearing mice, the lipid-2 KDa PEG-folic acid assembly was not covalently attached to the inner PLGA construct. Furthermore, since PEG was simply a linker between the lipid and the folic acid, its role in suppressing non-specific interactions is not clear.

Saxena et al investigated the biodistribution of PLGA nanoparticles entrapping ICG in healthy mice.[110] Although these constructs were not PEGylated, the investigators report that ICG encapsulation into these constructs resulted in nearly six times higher ICG levels within plasma at one hour post tail vein injection in mice, as compared to non-encapsulated ICG. In a previous study, our group reported biodistribution of ICG-NCs coated non-covalently with dextran or 10 nm ferromagnetic iron oxide nanoparticles, themselves individually coated with PEG, in healthy mice.[15] The half-life of these particles in blood and their circulation kinetics appeared unaffected compared to free ICG, presumably due to the non-covalent attachment of the coating materials. Therefore, to the best of our knowledge, our study presented here is the first aimed at characterizing the biodistribution of encapsulated ICG in a construct system composed of an inner ICG core entrapped by a polymeric shell with covalent outer surface PEGylation by both in-vivo quantitative fluorescence imaging and subsequent analysis of the various extracted organs.

Consistent with results of Saxena et al,[110] we observed a similar increase in ICG levels within plasma at one hour post injection in the case of the PEGylated ICG-NCs (Fig. 17(c)). We did not observe any significant differences in plasma ICG levels at one hour post-injection when administered in non-encapsulated form or as non-PEGylated ICG-NCs.

Higher ICG levels within various organs including the spleen, heart, lungs, and kidneys were reported by Saxena et al. when ICG was delivered in the PLGA-entrapped form. These investigators also reported that as early as five minutes post-injection, the

amount of ICG within the liver was nearly 2.5 times greater when it was administered in the PLGA-entrapped form as compared to free ICG. This result suggests that entrapment of ICG within the PLGA construct was not quite effective in delaying the accumulation of ICG within the liver. In comparison to our results, we detected higher ICG levels within the liver at 30 minutes post-injection with both non-PEGylated and PEGylated ICG-NCs (Fig. 17(b)).

In addition to the lack of PEGylation in the PLGA constructs, another factor that may be responsible for the differences between ours and those by Saxena et al. is the size of the constructs. The reported mean diameter of the PLGA constructs is 300 nm, nearly three times larger that the constructs used in our study. It has been indicated that PEGylated nanoparticles smaller than 100 nm have reduced plasma protein adsorption on their surfaces, and the blood clearance of such nanoparticles is slower than larger (> 100 nm) nanoparticles.[104,119]

Our results show that covalent coating of ICG-NCs with 5 KDa PEG can increase blood circulation time of ICG. Our findings are consistent with reports by Ballou et al.[120], and Ohno et al.,[121] who have indicated prolonged systemic circulation of PEGylated silica nanoparticles in-vivo. Ballou et al. have reported dramatic increase in circulating halftime of core-shell zinc sulfide-cadmium selenide QDs coated with PEG (5,000 Da). Their results have demonstrated extended circulation half-life of these particles to nearly 70 minutes compared to QDs coated with shorter length (750 Da and 3,400 Da) PEG chains with half-life of less than 12 minutes.[120] Ohno et al have reported prolonged blood half-life (~20 hours) of PEGylated Silica nanoparticles in healthy mice with preferentially

high accumulation in tumor tissue when injected into tumor-bearing mice.[121] Shah et al studied the effect of PEG coating on blood retention of gold nanoparticles. They indicate that the longer the particles stay in the systemic circulation, the chance of accumulation in tumor increases.[122]

The prolonged vascular circulation time of ICG as mediated by its encapsulation in these constructs can open up new possibilities for further clinical applications of ICG, which currently remain limited due to its rapid clearance from the vasculature and accumulation in the liver. The presence of ICG combined with the ability to functionalize the capsules provides the potential for ICG-NCs to serve as theranostic materials for targeted optical imaging of specific molecular biomarkers of a disease, and phototherapy. Previously, our group reported targeted fluorescence imaging of head and neck squamous cells, cervical squamous cell, and breast cancer cell, with various expression levels of epidermal growth factor receptor (EGFR) using anti-EGFR conjugated ICG-NCs.[73] We have also reported targeted fluorescent imaging of ovarian cancer cells using anti-HER2 functionalized ICG-NCs.[123]

The ICG-NCs can potentially be used as a phototherapeutic agent by generating heat in response to laser irradiation. In a previous study,[12] our group investigated the heat generating capability of ICG-NCs in response to 808 nm laser irradiation, and demonstrated the ability of ICG-NC suspensions to produce temperature rises to ≈80°C. In another study,[13] using a tissue phantom consisting of chicken breast, simulating normal tissue, and an embedded gelatin cylinder (simulating abnormal vasculature mass) loaded with ICG-NCs, we observed a nearly 20°C temperature rise within the gelatin cylinder at

depth of 3 mm below the surface in response to laser irradiation at 808 nm with incident power of 4.2 W. These results demonstrate the ability of ICG-NCs to induce a temperature rise in response to laser irradiation when embedded within an optically turbid tissue-like structure. In another study,[73] we demonstrated the capability of ICG-NCs coated with anti-EGFR in photothermal destruction of cancer cell lines.

3.4 CONCLUSION

In summary, the biodistribution of ICG-NCs coated with 5 KDa PEG in mice, as assessed by whole-body fluorescent imaging and individual organ uptake analysis, indicates prolonged vascular circulation time and delayed hepatic accumulation of these particles as compared to the uncoated constructs and non-encapsulated ICG. Encapsulation of ICG in such PEGylated constructs can potentially extend the current clinical applications of ICG as a result of its increased bioavailability.

CHAPTER 4: Development of Anti-HER2 Conjugated ICG-loaded Polymeric Nanoparticles for Targeted Optical Imaging of Ovarian Cancer

4.1 INTRODUCTION

Ovarian cancer is the deadliest type of gynecological cancer in the United States due to nonspecific symptoms in the early stages.[23,124] Although the 5-year survival rate of ovarian cancer in the early and localized stages is 94%, but the current screening methods can only diagnose 15% of all cases. The remaining majority of cases are diagnosed at advance stages when the 5-year survival rate can even decrease to 28%.[23,124] The low survival rate is attributed in part to effectiveness of the therapy at advance stages. The current therapeutic methods are surgery, cytoreduction or complete removal of ovaries, followed by chemotherapy. The challenge in cytoreduction surgery is successful detection and removal of all the tumor masses specially the ones smaller than 3 mm in diameter.[24] Current screening methods including CT, CT/PET, MRI or visual inspection won't be able or are not accurate in detecting very small tumor masses. The recognition that novel imaging techniques may have the potential to enhance prognosis and treatment of ovarian cancer and reduce the mortality, prompts development of enhanced and targeted imaging methods. Targeted fluorescence intraoperative imaging utilizing fluorescent probes could be one approach to enhance visualization of small tumor masses.[25]

Near infrared imaging probes are one category of probes with outstanding potential in imaging biological tissues owing to low absorption and scattering of light in this imaging window. The penetration depth of near infrared light in biological tissues could be up to several centimeters facilitating visualization of non-superficial tissue abnormalities.[79,81] Our group has previously reported development of near infrared theranostic nanoagents with applications in optical diagnostic and laser-induced phototherapy.[13,15,73,85,86,125] These theranostic nanoagents are polymeric nanocapsules loaded with indocyanine green (ICG-NCs), the only FDA approved NIR chromophore. The distinctive features of ICG-NCs are: (1) fabrication through green chemistry self-assembly, (2) tuning the diameter of ICG-NCs between 50 nm- 1 μm during the synthesis process, and (3) multi-functionality through covalent coupling of the targeting moieties to the surface of ICG-NCs. Monoclonal anti-epidermal growth factor receptor2 (anti-HER2) is a suitable candidate for targeting ovarian cancer, since not only HER2 receptors are over expressed in ovarian cancer cells but also the over-expression is specifically associated with increased risk of progression and death.[126–128]

Here in this study, we have investigated the effectiveness of covalent coupling of monoclonal anti-HER2 to the surface of ICG-NCs in targeted fluorescent imaging and laser-based phototherapy of ovarian cancer. Previously, we have demonstrated prolonged vascular circulation time and delayed hepatic accumulation of ICG-NCs when they were covalently coated with poly ethylene glycol (PEG, MW = 5000 Da) in mice.[125] We used same covalent coupling strategy to conjugate antibody to the surface of ICG-NCs using PEG chains. We modified the PEG layer on the surface of ICG-NCs by utilizing two

different PEG molecules, single aldehyde terminated PEG (PEG-ALD, MW = 5000 Da) and double aldehyde terminated PEG (ALD-PEG-ALD, MW = 10,000 Da). The monoclonal anti-HER2 was conjugated to the surface of ICG-NCs through double aldehyde terminated PEG molecules. We investigated targeted imaging potentials of anti-HER2 functionalized ICG-NCs to ovarian cancer cells using fluorescent confocal microscopy and two mammalian ovarian cancer cells lines with high and low levels of HER2 receptor expression. We further studied ICG-NCs mediated photodestruction of ovarian cancer cells in-vitro.

4.2 MATERIALS AND METHODS

4.2.1 Fabrication of ICG-loaded Nanocapsules

Sodium phosphate dibasic heptahydrate ($Na_2HPO_4.7H_2O$, Fisher Scientific), poly(allylamine) hydrochloride (PAH, Sigma-Aldrich), indocyanine green (Sigma-Aldrich), methoxy-poly(ethylene glycol)-butyraldehyde (PEG-ALD, MW = 5000 Da, Laysan Bio Inc.) and butyraldehyde-poly(ethylene glycol)-butyraldehyde (ALD-PEG-ALD, MW = 10,000 Da, Laysan Bio Inc.), Sodium dithionite ($Na_2S_2O_4$, Sigma-Aldrich), and phosphate buffer saline (PBS, Fisher BioReagents), monoclonal antibody to HER-2 (anti-HER2, Diagnostic Biosystems Inc.) were used as purchased.

Two different human ovarian cancer cell lines, SKOV3 cell line (ATCC®) and OVCAR3 cell line (ATCC®) were cultured separately in McCoy's 5a Medium Modified supplemented with 10% fetal bovine serum, and 1% penicillin.

4.2.2 ICG-NCs Synthesis and Antibody Conjugation

The polymeric nanocapsules (NCs) were fabricated through ionic cross-linking between Pollyallylamine hydrochloride (PAH) chains and sodium phosphate ions. The ICG was loaded into the NCs through a diffusion-mediated step to form ICG-NCs. We have previously reported fabrication of ICG-NCs in details.[16,86] In order to covalently conjugate anti-HER2 antibody to the surface of ICG-NCs, we use Polyethylene glycol (PEG) as a linker. We coat the surface of ICG-NCs with single and double aldehyde terminated PEG to reduce non-specific protein adsorption to the surface of ICG-NCs.[86] Besides creating non-fouling surface, the double aldehyde terminated PEG chains are used as linker to covalently conjugate anti-HER2 to ICG-NCs. The anti-HER2 antibody was added to the PEGylated ICG-NCs followed by addition of sodium dithionite as the reducing agent. The suspension was gently mixed for 10 seconds and aged 1 hour at 4 ºC followed by a washing step using centrifugation twice. The anti-HER2 PEG-ICG-NCs were resuspended in PBS and stored at 4 ºC in dark.

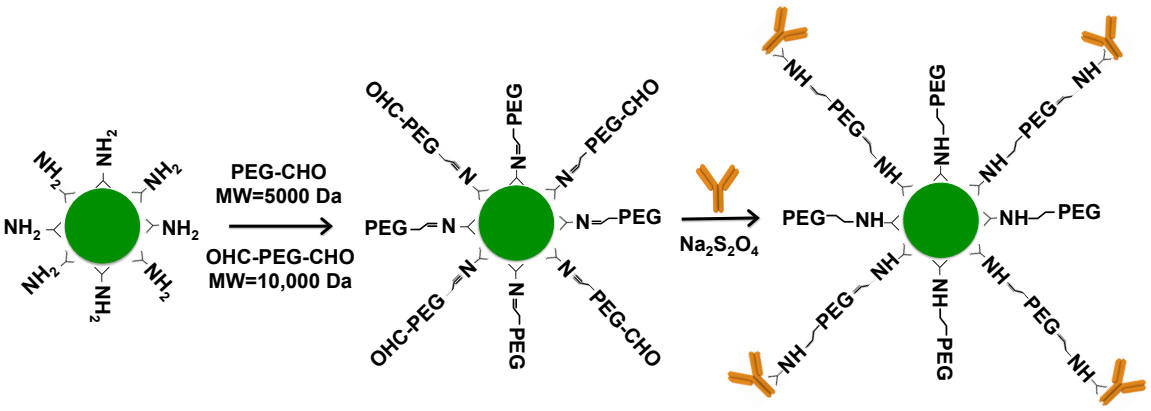

Scheme 2 Schematic of covalent conjugation of the anti-HER2 antibody to PEGylated ICG-NCs

4.2.3 Characterization of functionalized ICG-NCs

The hydrodynamic diameter and zeta-potential of non-functionalized and anti-HER2 functionalized ICG-NCs was measured using a Zetasizer nanoseries (NanoZS90). The absorption spectra of non-functionalized and functionalized ICG-NCs were obtained using a UV-Visible spectrophotometer (Cary 50 UV-Vis spectrophotometer) with optical pathlength of 1 cm. The fluorescence spectra of ICG-NCs in response to 680 nm excitation with a 450 W xenon lamp were measured using a fluorometer (Fluorolog-3 spectrofluorometer, Horiba Jobin Yvon).

4.2.4 Fluorescence Microscopy Sample Preparation

To prepare samples for fluorescence microscopy, 100 µl of SKOV3 or OVCAR3 cell suspension in fresh media ($\approx 10^6$ cells/ml) was added to each well of a 96-well flat-bottomed micro-titer plate. The cells suspensions were incubated at 37 °C supplied with 5% CO_2 over night to ensure adherence of the cells to the bottom of the plate. The next day, the old culture media was replaced with fresh media and 100 µl non-functionalized ICG-NCs and anti-HER2 PEG-ICG-NCs were added to different wells.

The samples were incubated at 37 °C supplied with 5% CO_2 for two hours to prepare samples for confocal fluorescence microscopy. Similar procedure was followed to prepare samples of SKOV3 and OVCAR3 cells to be incubated with non-functionalized and anti-HER2 PEG-ICG-NCs at 4 °C for three hours. The cells were washed twice with cold PBS and incubated with 4',6-diamidino-2-phenylindole (DAPI) for 10 minutes to stain cell nuclei prior to fluorescence imaging.

We used an Atto Pathway High Throughput Automated Confocal Imager to fluorescently image the cells incubated with functionalized ICG-NCs at 37 °C. An excitation wavelength of 740 nm and a long pass emission filter (>780 nm) were used to acquire near infrared (NIR) images. The camera exposure time was set at 1 seconds. The nucleus of the cells, labeled with DAPI, was imaged using an excitation wavelength of 350 nm and a long pass filter (>400).

We used another fluorescent microscope to image SKOV3 and OVCAR3 cells incubated with functionalized ICG-NCs at 4 °C. The fluorescence emission from DAPI (in the range of 435-485 nm) was collected in response to 360 ± 20 nm excitation. The NIR emission (>770 nm) was captured through a long pass filter with an electron multiplier gained CCD camera (Quant EM- CCD, Hamamatsu).

4.2.5 Flow Cytometry Sample Preparation

A BD flow cytometer (BD FACSAria cell sorter) was used to characterize interaction of the functionalized ICG-NCs with SKOV3 cells. SKOV3 cells were cultured in 12 wells plates a night before the experiments to ensure cell density of 10^6 cells/ml. The following day, SKOV3 cells were incubated with free ICG, functionalized and non-functionalized ICG-NCs for various time intervals ranging between 30 minutes to 3 hours in dark at 37 °C supplied with 5% CO_2. We used cells without ICG-NCs or free ICG as negative control. Following each incubation time, cells were washed with PBS twice through centrifugation (1200 rpm for 4 min) and resuspended in PBS. Propidium iodide (PI) was used to identify dead cells in order to exclude them from the analysis. The prepared samples were analyzed using 633 nm excitation and 785 nm emission

wavelength for ICG detection.

4.2.6. Laser-based Phototherapy Sample Preparation

We measured photothermal response of the functionalized ICG-NCs to NIR irradiation prior to investigating photo-destruction capability of ICG-NCs. A continuous wave near-infrared 808 nm diode laser with irradiation spot diameter of 2.2 mm, and incident irradiance (I_o) of 19.7 W/cm^2 was used to irradiate ICG-NCs samples. Functionalized and non-functionalized ICG-NCs and free ICG samples were prepared in concentrations that yielded same absorbance values at 808 nm in all three samples. PBS was irradiated as the negative control. The temperature changes after irradiation of 120 µl of each sample was measured using a negative temperature coefficient thermistor (20 kV, Vernier) connected to a Vernier LabQuest placed 2 mm outside the irradiation spot.

In order to study photo-destructive capability of functionalized ICG-NCs, we cultured SKOV3 cells in 96-well-plate over night to yield cell density of 10^6 cells/ml. The next day, cells were incubated with anti-HER2 functionalized ICG-NCs, non-functionalized ICG-NCs and freely dissolved ICG in PBS, in separate wells for three hours in dark at 37 °C supplied with 5% CO_2 to ensure uptake of nanocapsules by ovarian cells. Cells were washed twice with PBS prior to laser irradiation experiments. The cells incubated with PBS were irradiated as negative control. Each well was irradiated at two different spots (each spot diameter 5 2.2 mm) for 200 s. Cells were stored for two hours post irradiation at 37 °C supplied with 5% CO2. Cell damage in each well was analyzed using a live/dead assessment kit for mammalian cells (L3224, Invitrogen) and a fluorescent microplate reader (Molecular Devices FlexStation II 384,

Harlow Scientific). Specifically, live cells were identified using Calcein ($\lambda_{excitation}$ = 494 nm, $\lambda_{emission}$ = 517 nm) and dead cells using Ethidium homodimer-1 (($\lambda_{excitation}$ = 528 nm and $\lambda_{emission}$ = 617 nm).

4.3 RESULTS AND DISCUSSION

4.3.1. Characterization of nanoparticles

We have measured diameter of the non-functionalized ICG-NCs and anti-HER2 functionalized ICG-NCs using dynamic light scattering (Fig. 18(a)). The estimated mean diameter of ICG-NCs increases from 58 nm to 102 nm after PEGylation of ICG-NCs surface and conjugation of anti-HER2. Upadhyayula et al. have measured the average thickness of PEG layers with different molecular weights using spectroscopic elipsometry.[116] They have measured the thickness of the 10,000 Da PEG layer about 33 nm. Our results are consistent with their result showing about 44 nm increase in diameter of ICG-NCs due to both PEGylation and conjugation of antibody.

The absorption spectrum of non-functionalized and anti-HER2 functionalized ICG-NCs consists of two broadened spectral peaks at 730 nm and 810 nm in NIR region. Absorption spectrum of anti-HER2 functionalized ICG-NCs confirms conjugation of antibody to the nanoparticles as evidenced by presence of amino acids signature peaks in UV region (Fig. 18(c)).

The fluorescent emission spectra of non-functionalized and anti-HER2 functionalized ICG-NCs in response to photo-excitation at 680 nm have been shown in Fig. 18(d). The spectral peaks of fluorescence for anti-HER2 functionalized ICG-NCs are

at 792 nm and 700 nm and correspond to the monomeric form and aggregated form of ICG within nanoparticles, respectively. The monomeric spectral fluorescence peak of anti-HER2 functionalized ICG-NCs shows a slight red shift compared to non-functionalized ICG-NCs.

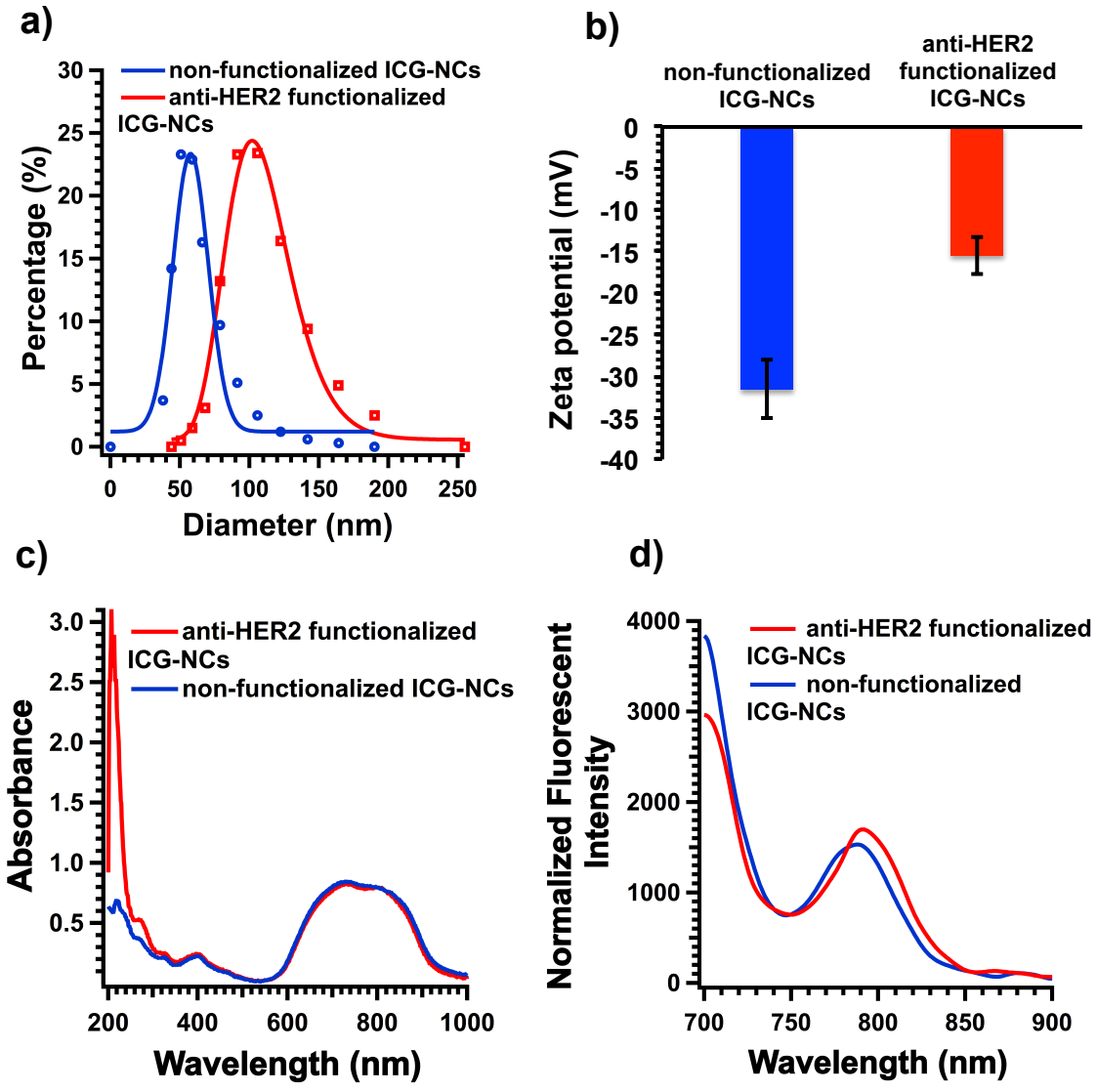

Figure 18 (a) Diameter distribution of non-functionalized and anti-HER2 functionalized ICG-NCs measured by dynamic light scattering. Circles and squares presents mean of three different measurements. The curves are fitted Gaussian and Lognormal functions to the non-functionalized and anti-HER2 functionalized ICG-NCs, respectively. (b) Zeta-

potential of non-functionalized and anti-HER2 functionalized ICG-NCs suspended in PBS. Each bar presents mean of three different measurements and error bars are showing single standard deviation. (c) Absorption spectra of non-functionalized and anti-HER2 functionalized ICG-NCs. (d) Normalized fluorescence spectra of non-functionalized and anti-HER2 functionalized ICG-NCs in response to 680 nm photo-excitation. Emission spectra were smoothed using IGOR Pro software with second order binominal algorithm.

4.3.2 Fluorescent Confocal Imaging of Ovarian Cancer Cells

Confocal fluorescent images of ovarian cancer cells (SKOV3) after two hours of incubation with freely dissolved ICG in PBS, non-functionalized ICG-NCs and anti-HER2 functionalized ICG-NCs at 37 °C has been presented in Fig.19. The maximum NIR emission intensity was recorded from SKOV3 cells incubated with anti-HER2 functionalized ICG-NCs (Fig. 19(j)). The overlay of the confocal fluorescent NIR and DAPI images of the cells incubated with anti-HER2 functionalized ICG-NCs illustrates internalization of particles with localization around nuclei of the ovarian cancer cells (Fig. 19(l)). However, SKOV3 cells incubated with freely dissolved ICG and non-functionalized ICG-NCs emitted none or very minimal NIR signal. This result indicates enhanced uptake of anti-HER2 functionalized ICG-NCs by Ovarian cancer cells (SKOV3) compared to very minimal uptake of non-functionalized ICG-NCs by same cells.

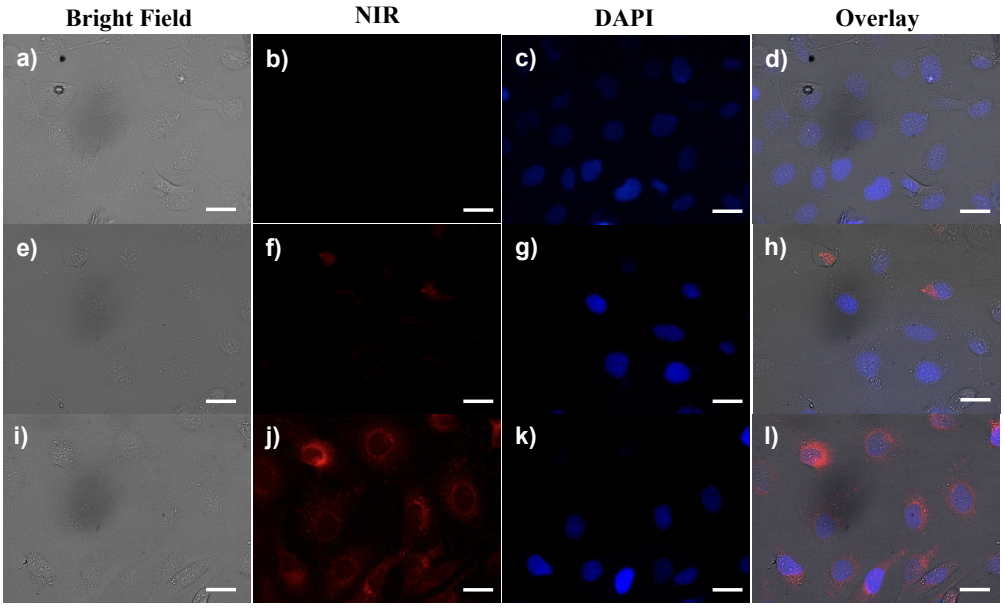

Figure 19 Bright field, and false-color confocal fluorescent images of ovarian cancer cells (SKOV3) after 2 hours of incubation with (a-d) freely dissolved ICG in PBS, (e-h) non-functionalized ICG-NCs and (i-l) anti-HER2 functionalized ICG-NCs. (Scale bar = 20 μm)

4.3.3 Fluorescent imaging of SKOV3 and OVCAR3 cells

To confirm specific interaction between anti-HER2 functionalized ICG-NCs and HER2 receptors on the surface of ovarian cells, we incubated two different ovarian cancer cells line with high (SKOV3) and low (OVCAR3) levels of HER2 receptor expression,[127] with functionalized ICG-NCs. The fluorescent images of SKOV3 and OVCAR3 cells incubated with freely dissolved ICG in PBS, non-functionalized ICG-NCs and anti-HER2 functionalized ICG-NCs for three hours at 4 °C are shown in Fig. 20. The incubation temperature of 4 °C was chosen to prevent non-specific endocytosis of either non-functionalized or anti-HER2 functionalized ICG-NCs by ovarian cancer cells. The cells were washed twice with cold PBS prior to imaging. The overlay of the NIR

fluorescent image and visible fluorescent image of the SKOV3 cells incubated with anti-HER2 functionalized ICG-NCs revealed localization of functionalized particles at SKOV3 cell membrane. This phenomenon can be noticeably visualized in Fig. 20(f) as the red ring represents the cell membrane. On the contrary, minimal NIR signal was detected from the membrane of the OVCAR3 cells incubated with anti-HER2 functionalized ICG-NCs (Fig. 20(d)). These results suggest that interaction of anti-HER2 functionalized ICG-NCs with SKOV3 cells are specific and receptor mediated.

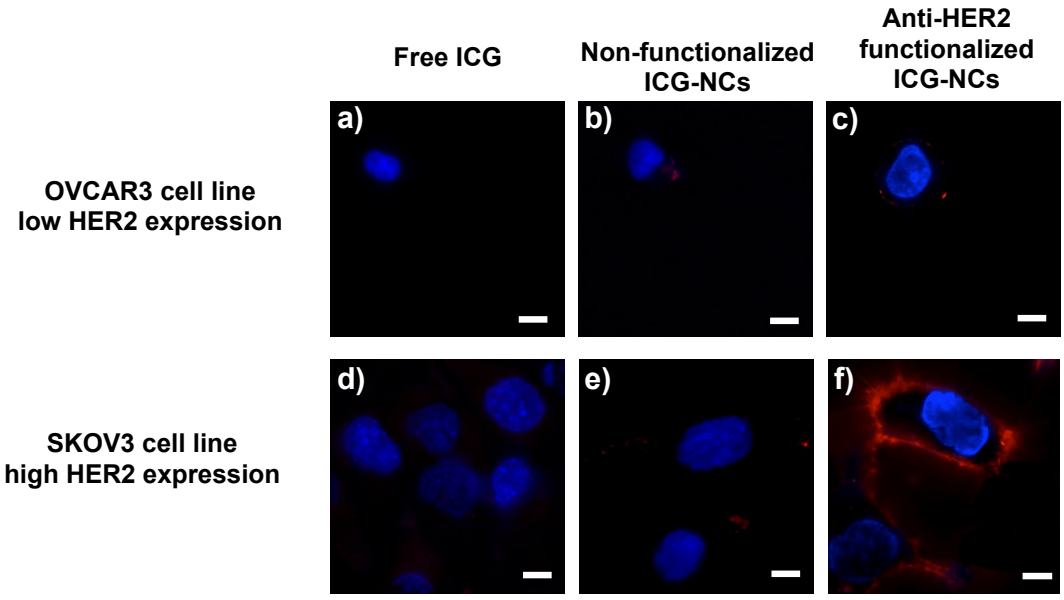

Figure 20 Fluorescent images of OVCAR3 cells incubated with media containing (a) freely dissolved ICG in PBS, (b) non-functionalized and (c) anti-HER2 functionalized ICG-NCs and SKOV3 cells incubated with media containing (a) freely dissolved ICG in PBS, (b) non-functionalized and (c) anti-HER2 functionalized ICG-NCs at 4 °C for three hours. Cells nuclei were stained by DAPI and falsely colored in blue using ImageJ software. The NIR fluorescent signal from ICG was falsely colored in red. The scale bars correspond to 10 μm.

4.3.4 Characterization of ovarian cancer cells targeting by anti-HER2 functionalized ICG-NCs

We investigated the concentration of ICG at different times post incubation (30 min, 1 hr, 2 hr and 3 hr) in SKOV3 cell populations using flow cytometry (Fig. 21 (a)-(d)). The population distribution of SKOV3 cells incubated with anti-HER2 functionalized ICG-NCs demonstrates a shift to the right (higher ICG fluorescent signal) as incubation time increases. Moreover, at all different incubation times, notably larger population of SKOV3 cells were detected in ICG fluorescent channel. The population distribution of SKOV3 cells incubated with non-functionalized ICG-NCs was very close to the negative control at 30 minutes and 1 hour post incubation. The cell count increases at 2 hours post injection with non-functionalized ICG-NCs, however, the ICG fluorescent signal of the cells remained low. The most intense peak in all different incubation times was associated with cells incubated with anti-HER2 functionalized ICG-NCs for 3 hours.

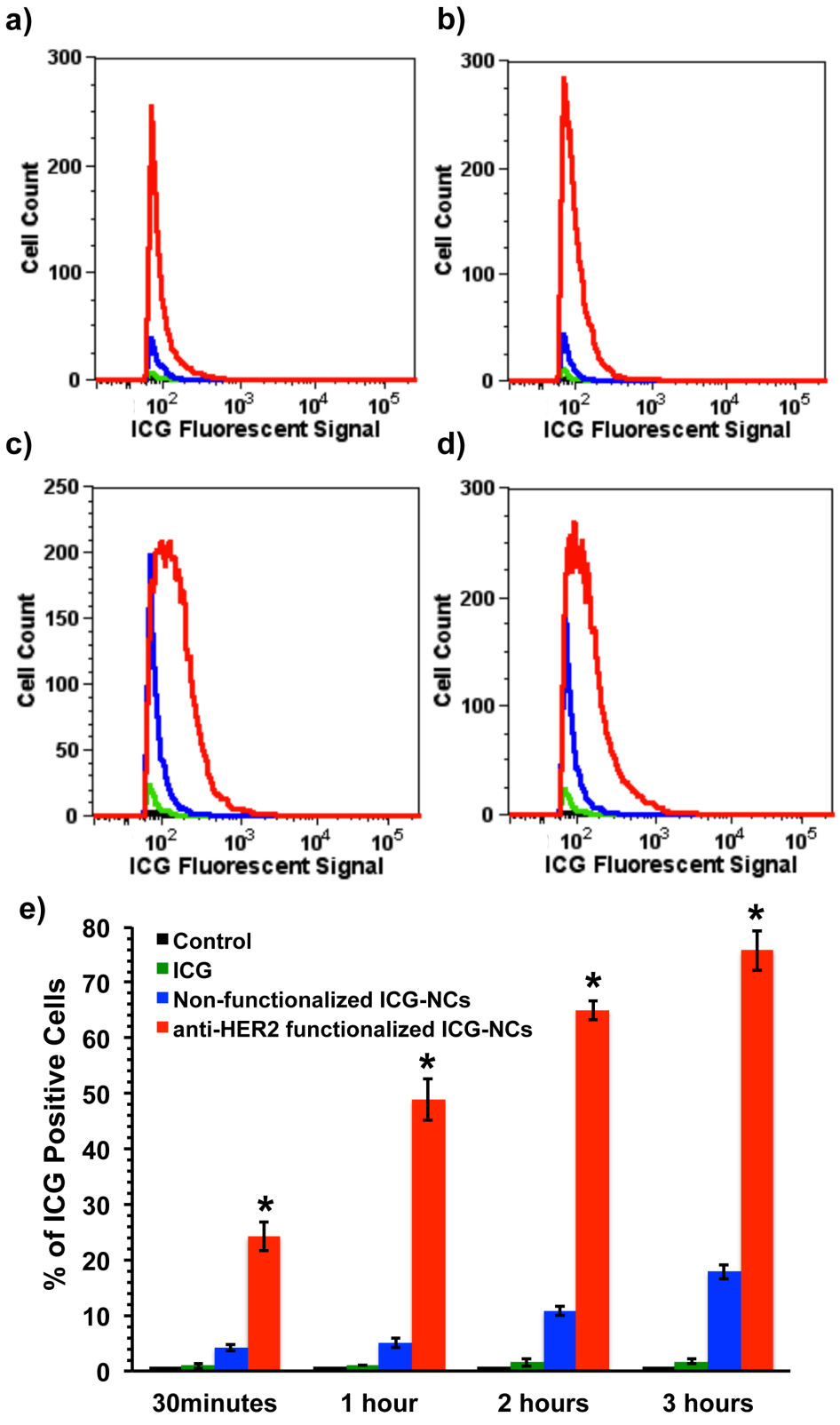
a)
b)
c)
d)
e)
Cell Count
ICG Fluorescent Signal
% of ICG Positive Cells
Control
ICG
Non-functionalized ICG-NCs
anti-HER2 functionalized ICG-NCs
30minutes
1 hour
2 hours
3 hours

Figure 21 Characterization of anti-HER2 functionalized ICG-NCs by ovarian cancer cells (SKOV3) using flow cytometry. (a) Histogram of ICG fluorescent signal for population of SKOV3 cells incubated with anti-HER2 functionalized ICG-NCs (red), non-functionalized ICG-NCs (blue), free ICG (green) and media containing none of these reagents (black, negative control) for (a) 30 minute, (b) 1 hour, (c) 2 hours, and (d) 3 hours. (e) Percentage of ICG positive cells after incubation with free ICG, non-functionalized and anti-HER2 functionalized ICG-NCs for 30 min, 1 hr, 2 hr and 3 hr. Each bar represent mean of measurement in three different samples. Error bars are presenting single standard deviation. Asterisks denote statistically significant difference in the percentage of ICG positive cells when cells were incubated with anti-HER2 functionalized ICG-NCs as compared to non-functionalized ICG-NCs, free ICG or negative control.

In order to quantify number of SKOV3 cells emitting NIR signal, we use percentage of ICG positive cells defined as the ratio of cells emitting NIR signal to the total number of cells. The highest percentage of ICG positive cells, 76%, was detected in cells incubated with anti-HER2 functionalized ICG-NCs for 3 hours (Fig. 21(e)). This number was almost 4 times higher than percentage of ICG positive cells when cells where incubated with non-functionalized ICG-NCs for 3 hours. The highest percentage of ICG positive cells at all post incubation times was associated with cells incubated with anti-HER2 functionalized ICG-NCs and the percentage increased significantly by increasing incubation time.

4.3.5 Laser-induced photodestruction of ovarian cancer cells

The temperature rise due to continuous laser irradiation of functionalized and non-functionalized ICG-NCs has been shown in Fig. 22(a). The samples were prepared with concentration of ICG to yield same absorbance value at 808 nm. Same volume of each sample was irradiated for 200 seconds and temperature was measured 2 mm outside the irradiation spot. A rapid temperature rise was observed in the first 100 seconds of

irradiation of functionalized and non-functionalized ICG-NCs and freely dissolved ICG, which was followed by a slow decay in the next 100 seconds. The highest temperature recorded for each sample was 52 °C, 52 °C and 50 °C for anti-HER2 functionalized ICG-NCs, non-functionalized ICG-NCs and freely dissolved ICG, respectively. Temperature measurements indicate photothermal response of the ICG-NCs in response to continuous 808 nm laser irradiation. The maximum temperature rises reported above are not the actual temperature rise in the irradiation spot since it was recorded 2 mm outside the irradiation spot.

To evaluate potential ICG-NCs-mediated photodestruction of ovarian cancer cells, we incubated SKOV3 cells with five different dosages of anti-HER2 functionalized, non-functionalized ICG-NCs or freely dissolved ICG for three hours. The cells were washed twice with cold PBS prior to laser irradiation at 808 nm with irradiance of 19.7 W/cm^2 for 200 seconds. Each sample was irradiated at two different spots with the irradiation parameters mentioned above. We used SKOV3 cells not exposed to ICG-NCs or free ICG as negative control. Using the mammalian live/dead assay, our results indicated that anti-HER2 functionalized ICG-NCs are capable of photothermally destructing ovarian cancer cells (Fig. 22(b)). Anti-HER2 functionalized ICG-NCs with concentration of 4X resulted in 85.5% ovarian cancer cell dead which was the highest percentage of cell destruction among all samples and concentrations and was 2 times higher than cell dead caused by non-functionalized ICG-NCs. Decreasing the concentration of anti-HER2 functionalized ICG-NCs to 2X resulted in 55% cell dead, however, same concentration of non-functionalized ICG-NCs caused only 30% cell dead.

There was a statistically significant difference (p-value < 0.005) between the percentage of ovarian cancer cells photothermally destroyed after incubation with all five different concentrations of anti-HER2 functionalized ICG-NCs and those cell incubated with non-functionalized ICG-NCs, free ICG and control. These results are very promising in demonstrating capabilities of anti-HER2 functionalized ICG-NCs as theranostic agents for NIR fluorescent imaging and photothermal therapy of ovarian cancer cells.

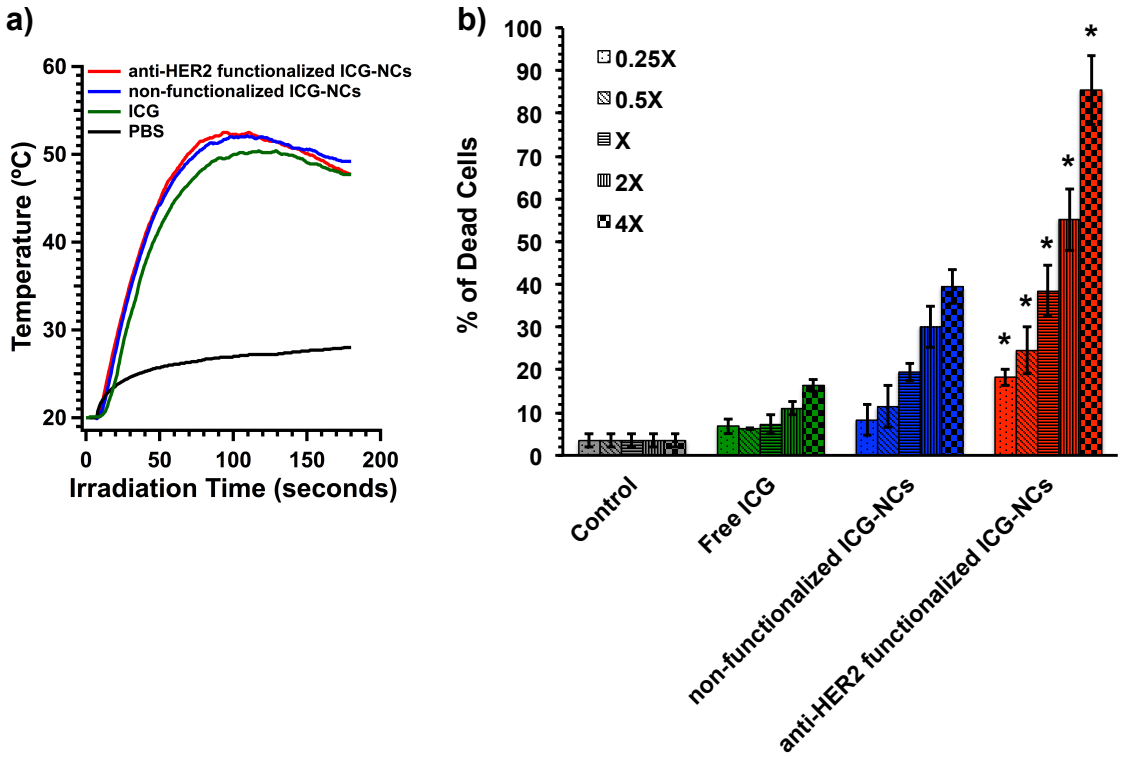

Figure 22 (a) Photothermal response of freely dissolved ICG in PBS, non-functionalized and anti-HER2 functionalized ICG-NCs and PBS solution (negative control) in response to continuous 808 nm laser irradiation with intensity of 19.7 W/cm^2. (b) Percentage of ovarian cancer cells (SKOV3) photothermally destroyed by anti-HER2 functionalized ICG-NCs and continuous 808 nm laser irradiation. Cells were incubated with five different concentrations of free ICG or non-functionalized or anti-HER2 functionalized ICG-NCs for three hours. SKOV3 cells incubated with PBS were used as negative control. The cell injury was assessed using mammalian live/dead assay kit and a fluorescence microplate reader. Two different spots were irradiated in each sample, each for 200 seconds. Bars represent mean of three different samples and error bars are

presenting single standard deviation. Asterisks denote statistically significant difference in the percentage of cells destroyed by anti-HER2 functionalized ICG-NCs as compared to non-functionalized ICG-NCs, free ICG or PBS.

4.4 CONCLUSION

Here, we have demonstrated successful covalent coupling of HER2 receptor antibody to the surface of ICG loaded polymeric nanocapsules using PEG chains as linkers and reductive amination procedure. The presence of amine groups on the surface of these constructs acts as a suitable platform for attaching targeting moieties and enables covalent conjugation on the surface of ICG-NCs.

In a previous study by our group, we reported laser-induced photothermal destruction of three different cancer cell lines, human head and neck squamous cells, human cervical squamous cells, and cancerous human breast cells, using anti-EGFR coated ICG-NCs.[16] However, the monoclonal EGFR antibody was coated on the surface of ICG-NCs through physisorption and EGFR receptors were targeted on the surface of carcinoma cells. We were motivated by the results of this study to intensely investigate optical imaging and laser-mediated photothermal therapy applications of functionalized ICG-NCs using modified covalent antibody-coupling procedures.

In another study, we investigated the heat-generation capability of ICG after being loaded into polymeric mesocapsules (MCs) in response to 808 nm laser irradiation and observed that ICG retains its heat generation ability.[13] Additionally, efficiency of ICG-loaded MCs to induce thermal damage was studied using tissue phantoms. The tumorous tissue was simulated using cylindrical phantoms made of gelatin and intralipid loaded

with ICG-MCs. The cylindrical phantoms were embedded within fresh chicken breast tissue. Temperature rises up to 20 °C were measured within the phantom 3 mm below the surface in response to continuous 808 nm laser irradiation with 4.2 W power.[13] The results of this study were promising since demonstrating the ability of ICG-MCs to generate heat in an optically turbid media simulating human tissue in response to NIR laser irradiation.

The anti-HER2 functionalized ICG-NCs are providing a platform for active targeting, deep optical diagnostic and photothermal therapy of ovarian cancer simultaneously. We have developed these nanotheranostis using ICG as the only agent providing fluorescent imaging and laser-induced heat generation. Using anti-HER2 receptor antibody offers specific targeting toward cells with overexpression of HER2 receptor. Our results demonstrated that endocytosis of our anti-HER2 conjugated ICG-NCs by Ovarian cancer cells is receptor-mediated. The fluorescent microscopy images of SKOV3 and OVCAR3 cells at 4 °C revealed elevated binding of anti-HER2 functionalized ICG-NCs by higher HER2 receptor expressed SKOV3 cells compared to OVCAR3 cells. Almost minimal binding was observed for non-functionalized ICG-NCs to either of the cell lines. Therefore, these theranostic nanoparticles have promising application in targeting the cells with high levels of HER2 receptor and evading healthy cells. Furthermore, post active targeting of overexpressed HER2 receptor cells; these theranostic nanoparticles can induce heat in response to NIR laser irradiation and cause thermal damage to the cells. Fortunately, the thermal damage can be restricted to the ovarian cells only due to initial evasion of healthy cells by functionalized nanoparticles.

Having said all the advantages of utilizing these theranostic nanoparticles for diagnosis and treatment of ovarian cancer, further in-vivo studies need to be done to demonstrate ability of such constructs for intraoperative diagnostic and therapeutic applications.

CHAPTER 5: Erythrocyte-derived photo-theranostic agents: hybrid nano-vesicles containing indocyanine green for near infrared imaging and therapeutic applications

5.1 INTRODUCTION

Transduction of light by specific molecules into other types of energy such as heat, chemical energy, and acoustic waves, has provided the basis for the development of photothermal therapy and photodynamic therapy (PDT) procedures, as well as diagnostic methods based on fluorescence and photoacoustic imaging. The use of near infrared (NIR) wavelengths (λ), particularly in the range of $\approx$ 650-1450 nm, is especially advantageous since in this "optically transparent window," light can penetrate relatively deeply into biological materials as there is minimal photons absorption by endogenous molecules.[129]

Delivering NIR-transducing exogenous materials to a particular target of interest (e.g., abnormal vasculature, tumor mass) provides an approach to enhance the local optical absorption of the target. Once activated by NIR light, the exogenous material may be used as a photo-theranostic agent to enhance both the optical contrast of the target, and phototherapeutic efficacy, particularly in deeply seated targets.

A particular NIR-transducing molecule is Indocyanine green (ICG) ($C_{43}H_{47}N_2NaO_6S_2$; molecular weight $\approx$ 775 Da). It is composed of two polycyclic (benzoindotricarbocyanine) lipophilic moieties, linked with a polyene bridge. A sulfonate group, bound to the nitrogens of each polycyclic part, provides net negative charge and

water solubility. Therefore, the entire molecular structure leads to amphiphilic characteristics of ICG.

ICG's medical applications began in late 1950's for measurements of cardiovascular output to characterize valvular and septal defects,[130] and soon after it was used to assess hepatic function.[131] It received supplemental approval by United Stated Food and Drug Administration (FDA) for ophthalmic angiography in 1975. In ophthalmological applications, ICG is recommended for imaging selective chorioretinal disorders including suspected polypoidal choroidal neovascularization (CNV), chronic central serous chorioretinopathy (CSC), and choroidal hemangioma.[87] To-date, ICG remains the only NIR dye approved by FDA for cardiocirculatory measurements, liver function tests, and ophthalmological imaging.

In addition to its current clinical utility, ICG has been investigated for sentinel lymph node mapping in patients with melanoma, prostate, breast, and other types of cancer.[132–135] Its utility in fluorescence-guided PDT of choroidal disease has also been reported.[136,137] Additionally, ICG has been studied for potential phototherapeutic applications including treatment of CSC,[138] cutaneous hypervascular malformations,[139] and PDT of choroidal melanoms.[140]

Despite usage in clinical medicine, ICG's major drawbacks are its short half-life within plasma (≈ 2-4 minutes), and exclusive uptake by hepatic parenchymal cells followed by biliary excretion. Given its amphiphilic nature, ICG binds to various molecular species including albumin, and high- and low-density lipoproteins within the vasculature. Given these limitations, the potentials of this clinically-proven exogenous

material as a theranostic agent for broader medical applications, which may require extended circulating lifetimes, remain limited.

Encapsulation has been investigated to shield ICG from non-specific interactions within the plasma, and extend its circulation time in the vasculature. Our group has reported that encapsulation of ICG into synthetic polymer-based nano-constructs enhances the contrast of in vivo fluorescent images from the heart and lungs for at least up to 90 minutes,[14] and delays maximal hepatic accumulation to at least 60 minutes after tail vein injection in mice.[125]

Recently, attention has been given to the use of biological materials as platforms for the delivery of therapeutic or imaging agents. We have reported the use of genome-depleted plant infecting brome mosaic virus doped with ICG as a nano-construct for NIR fluorescence and photoacoustic imaging.[141,142]

Mammalian cells, particularly erythrocytes, present another type of biological vectors for the delivery of therapeutic and imaging agents.[143–146] In relation to cell-based imaging, hemoglobin-depleted red blood cells (erythrocyte ghosts (EGs)) have been used to encapsulate iron oxide for potential magnetic resonance imaging (MRI) applications.[147–149] Gold nanoparticles have been incorporated into human erythrocytes to produce tracers with enhanced contrast for potential dynamic X-ray imaging of blood flow.[150] Fluorescein isothiocyanate, a non-NIR dye, has been successfully loaded into EGs having diameters of ≈ 5 μm, with the intention of developing such constructs as plasma analyte or extracellular pH sensors.[151,152] Flower et al. recently loaded ICG into micron-sized EGs, and utilized the constructs as a fluorescent analogue of erythrocytes to

characterize the movement of erythrocytes in retinal capillaries and choriocapillaris of monkeys and rabbits.[153]

Here, we report the first proof-of-principle to demonstrate the successful engineering of ICG-loaded nano-sized vesicles derived from EGs, and their utility as photo- theranostic agents for fluorescence imaging and photothermal destruction of cells. We refer to these nano-vesicles as near infrared erythrocyte-mimicking transducers (NETs).

5.2 MATERIALS AND METHODS

5.2.1 Fabrication of NETs

The schematic of the NETs fabrication procedure is shown in Fig. 23. We collected whole blood from mice through cardiac puncture using heparin coated tube and syringe. Whole blood was centrifuged at 800×g for five minutes at 4 °C to separate the erythrocytes. The erythrocytes were then washed in 1 ml of cold 1× phosphate PBS (310 mOsm, pH=8), and centrifuged at 800×g for five minutes at 4 °C. Subsequently, 500 µl of packed erythrocytes were suspended in one ml of hypotonic buffer (0.25×PBS buffer solution, 80 mOsm, pH=8) and incubated at 4 °C for 20 minutes. The erythrocytes were centrifuged at 800×g for five minutes at 4 °C to separate the hemoglobin. The resulting erythrocyte ghosts (EGs) were sonicated in an ice bath sonicator at 60 W for five minutes. The EGs were extruded 20 times through 400 nm polycarbonate porous membranes, followed by 20 more extrusions through 100 nm polycarbonate porous membranes using an Avanti mini extruder.

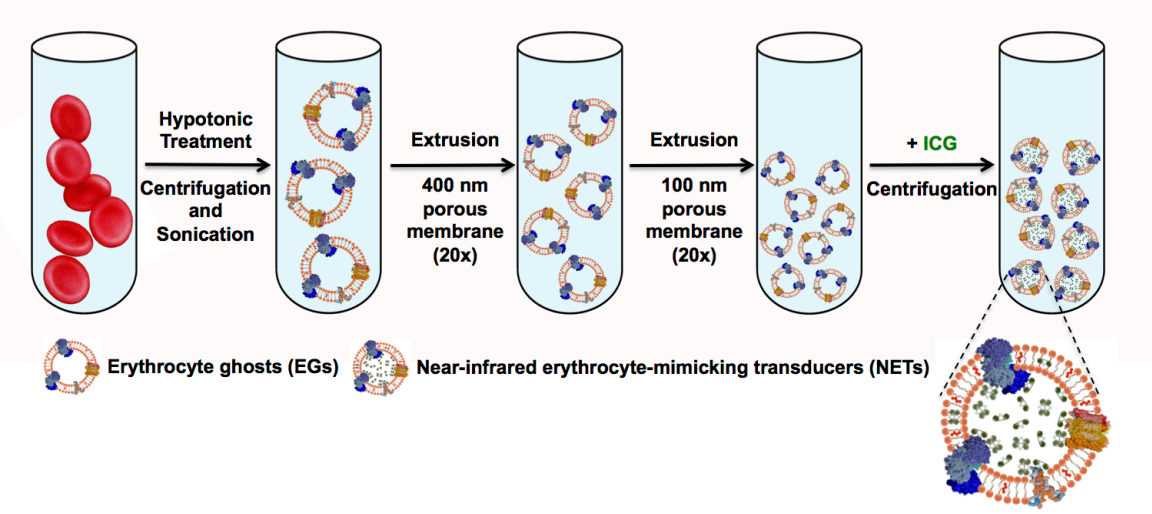

Figure 23 Schematic of NETs fabrication process. Erythrocytes isolated from whole blood were re-suspended in hypotonic buffer for 20 minutes followed by centrifugation to separate the hemoglobin. The erythrocyte ghosts (EGs) were sonicated and extruded 20 times through 400 nm polycarbonate porous membranes, followed by 20 additional 20 extrusions through 100 nm membranes. ICG dissolved in phosphate buffer saline (PBS) was added to the EGs suspended in the hypotonic buffer solution.

To load ICG into the EGs, 300 µl of EGs suspended in PBS was incubated with 300 µl of ICG (500 µg/ml ≈ 0.65 mM) dissolved in PBS and 300 µl of hypotonic buffer (Na_2HPO_4/NaH_2PO_4, 140 mOsm, pH=8) for five minutes at 4 °C in dark. The suspension was then centrifuged, and washed twice at 14,000×g for 10 minutes at 4 °C. The ICG-loaded EGs were re-suspended in cold 1×PBS buffer solution to restore tonicity.

5.2.2 Characterization of NETs

The hydrodynamic diameters of NETs suspended in PBS were measured by dynamic light scattering (Zetasizer NanoZS90, Malvern Instruments Ltd). To prepare samples for TEM, a drop of NETs suspension in PBS was placed on a carbon-coated grid for 10 minutes. The grid was rinsed twice with distilled water. To stain the NETs, a drop

of 1% uranyl acetate solution was deposited on the grid and dried in air. The grid was imaged using a Philips TECNAI 12 Transmission Electron Microscope. The absorption spectra of NETs suspended in 2.4 ml of PBS were obtained using a UV-Visible spectrophotometer (Jasco-V670 UV-Vis spectrophotometer) with optical pathlength of 1 cm. The fluorescence spectra of NETs in response to 650 nm excitation with a 450 W xenon lamp were obtained using a fluorometer (Fluorolog-3 spectrofluorometer, Horiba Jobin Yvon). We obtained the normalized fluorescence spectra ζ (λ) as:

$$\zeta(\lambda) = \frac{F(\lambda)}{1 - 10^{-A(\lambda)}}$$

where A and F are the wavelength-dependent absorbance, and intensity of the emitted fluorescent light, respectively.

5.2.3 Fluorescence microscopy imaging of human dermal microvascular (HDME) endothelial cells

To illustrate the effectiveness of NETs as photo-theranostic agents, we utilized HDME cells (ATCC®) as model cell systems for fluorescence imaging and photothermal destruction. We cultured the HDME cells in 96 well culture plates containing vascular cell basal medium supplemented with 5% Fatal Bovine Serum (FBS) and endothelial cell growth Kit-VEGF for 24 hours in advance of imaging to ensure adhesion and cell density growth to ≈106 cells/ml. The cells were then incubated with complete vascular cell basal media containing NETs or 13 μM ICG (control) for three hours. We then washed the cells incubated with NETs or free ICG twice with PBS prior to imaging. The cells nuclei were stained using 4',6-diamidino-2-phenylindole (DAPI). The fluorescence emission

from DAPI in the range of 435-485 nm was collected in response to 360 ± 20 nm excitation. In response to photo-excitation by a Nikon Mercury/Xenon are lamp providing light over the 740±35 nm spectral band, the NIR emission (>770 nm) transmitted through a long pass filter was captured using an electron multiplier gained CCD camera (Quant EM- CCD, Hamamatsu) at integration time of 0.1 s and gain of 1.0.

Photothermal response and photostability of NETs, and photodestruction of HDME cells.

To investigate the photothermal response of the NETs, we used a continuous wave near-infrared 808 nm diode laser with irradiation spot diameter of 2.2 mm, and incident irradiance (I_o) of 19.7 W/cm^2. NETs suspended in PBS, and ICG dissolved in PBS were prepared in concentrations that gave the same absorbance value at 808 nm for both samples. As the negative control sample, we irradiated the PBS solution at the same irradiation parameters as above. Same volume of each sample (120 µl) was irradiated, and temperature changes were measured using a negative temperature coefficient thermistor (20 kΩ, Vernier) connected to a Vernier LabQuest placed 2 mm outside the irradiation spot.

We investigated the photostability of the NETs by collecting their absorption spectra following laser irradiation of 120 ml of the NETs suspensions for various radiant exposure times (60, 90, 140, and 200 s) at 808 nm and I_o = 19.7 W/cm^2. Additionally, we performed a cyclic laser irradiation, and measured the resulting temperature response.

To investigate the photo-destructive capability of the NETs, we cultured the HDME cells in a 96 well-plate as described above. On the following day, cells were incubated with 200 µl of NETs suspended in PBS, or 200 µl (13 µM) of free ICG dissolved in PBS, in

separate wells for three hours in dark at 37 °C supplied with 5% CO_2. These levels of NETs or ICG were used to ensure the same absorbance value (0.6) at 808 nm in both NETs- and ICG-treated cells. Both the NETs- and ICG-treated cells were washed twice with PBS prior to laser irradiation experiments. We irradiated the cells incubated in PBS as negative control agent. Each well was irradiated at three different spots (each spot diameter = 2.2 mm), for 200 s. By using three spots, approximately 80% of the cells could be irradiated. Cells were stored for two hours post irradiation at 37 °C supplied with 5% CO_2. The live/dead viability kit (L3224, Invitrogen) for mammalian cells was used to assess injury. Cell damage in each well was analyzed using a live/dead assessment kit for mammalian cells and a fluorescent microplate reader (Molecular Devices FlexStation II 384, Harlow Scientific). Specifically, live cells were identified using Calcein (λexcitation=494 nm, λemission=517 nm) and dead cells using Ethidium homodimer-1 ((λexcitation=528 nm and λemission=617 nm).

5.2.4 Cytotoxicity assessment of NETs

To evaluate the potential cytotoxicity of the NETs, we cultured the HDEM cells in 96 well-plates as described above. On the following day, cells were washed with PBS and then incubated with complete cell culture media containing NETs for three and 24 hours. The effective dosage (D_{eff}) of the NETs for cytotoxicity experiments was 12 ml21 where we define D_{eff} as the absorbance of the NETs population (1.2 at 808 nm) suspended in 100 ml of PBS solution. Cells incubated with complete cell culture media for 24 hours without any additional reagents were used as the positive control population. Cells incubated with 100 ml methanol for 24 hours were used as the negative control

population. Cells were washed twice with PBS post incubation with NETs, and stained using the live/dead assay described above.

5.3 RESULTS & DISCUSSION

5.3.1 NETs size characterization

We can manipulate the diameter distribution of the NETs, and subsequently, their photophysical properties by varying the extrusion procedures required to fabricate nano-sized constructs, and the time of the EGs exposure to the hypotonic solution containing ICG at a given concentration. With the exception of the transmission electron microscope (TEM) image of the NETs, all results presented herein are based on 20 initial extrusions of EGs through 400 nm diameter polycarbonate porous membranes, followed by 20 additional extrusions through 100 nm diameter membranes, subsequent addition of 215 μM ICG into the hypotonic buffer solution containing the suspension of the nano-sized EGs, and incubation for five minutes. The mean peak (d_{peak}) and estimated mean ($\overline{d}_{mean}$) diameters of EGs are 80.77 nm and 95.26nm, respectively (Fig. 24(a)). When doped with ICG, d_{peak} and $\overline{d}_{mean}$ increase to 134.78 nm and 124.61 nm, respectively. Only about 5% of ICG leaks from the NETs after one hour.

Transmission electron microscope (TEM) imaging confirms the nano-sized diameter of the NETs (Fig. 24(b)). NETs imaged by TEM were fabricated by six extrusions through 100 nm membranes, and using 215 μM ICG.

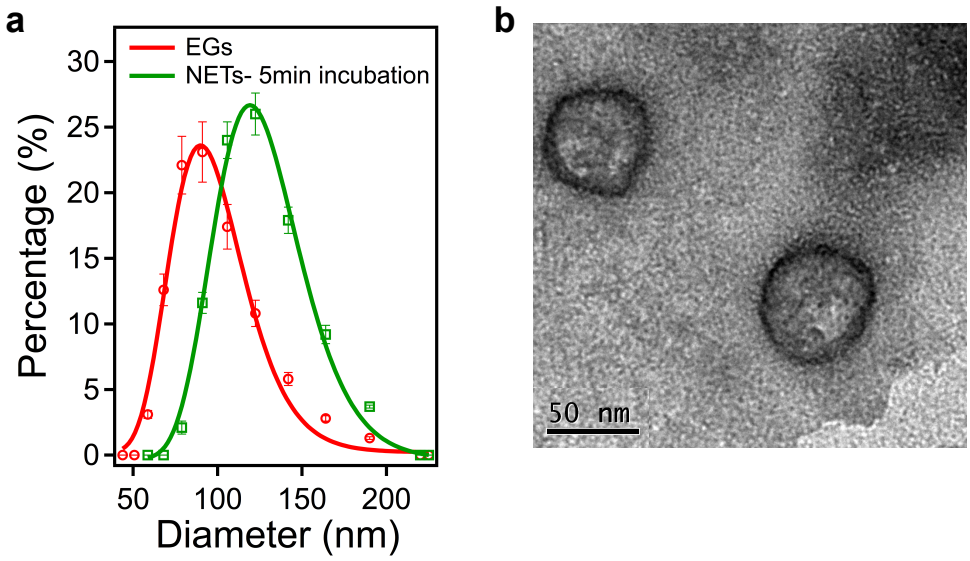

Figure 24 Size distribution profiling and TEM image of NETs. a, Diameter distributions of EGs and NETs. Using dynamic light scattering, the ranges of the measured diameters are 58-190 nm for the EGs, and 78-190 nm for the NETs formed after five minutes of incubation in hypotonic solution and PBS containing 215 μM ICG. Each measurement was repeated using at least three samples. We present the mean of each measurement, represented as circles for EGs, and squares for NET. The error bars represent standard deviations from the mean values. We fitted Lognormal functions to the measured diameter distributions (solid curves). The estimated mean diameters, as determined by the Lognormal fits, are 95.26 nm (R^2=0.97), and 124.61 nm (R^2=0.98) for EGs and NETs, respectively. b, Illustrative TEM image of NETs.

5.3.2 Absorbance of NETs

Absorption spectrum confirms the elimination of EG's hemoglobin content as evidenced by the absence of the signature absorption peaks of oxygenized hemoglobin at 542 and 576 nm, and that of deoxygenized hemoglobin at 556 nm (Fig. 25(a)). The UV absorption for both non-loaded erythrocyte ghosts and NETs is attributed to membrane proteins. Doping the EGs with ICG endows the constructs with NIR absorption capability.

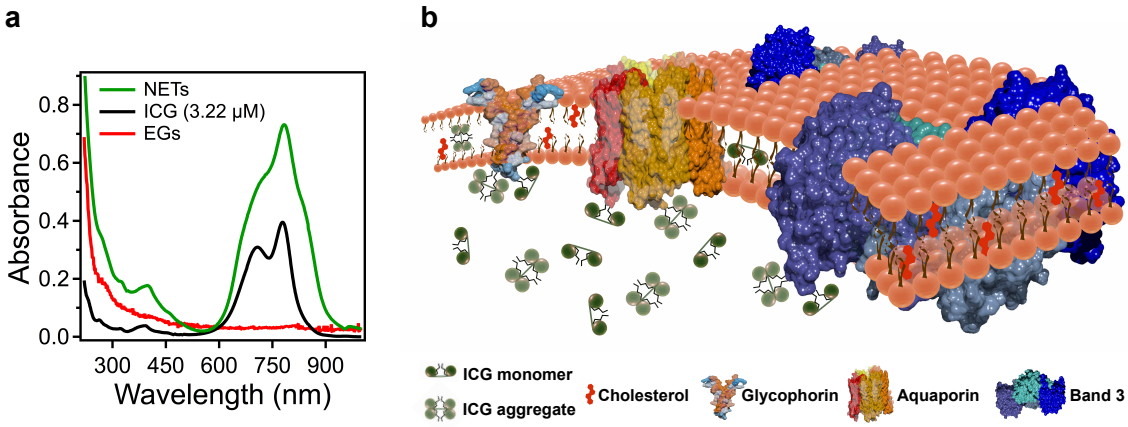

Figure 25 Absorption spectra and a physical model of a NET containing ICG. a, Absorption spectra corresponding to free (non-encapsulated) ICG (3.22 μM) dissolved PBS, and EGs and NETs re-suspended in PBS after fabrication. b, A physical model of a NET shows an ensemble of ICG conformational states comprised of ICG monomers, ICG aggregates, and monomers and aggregates of ICG bound to membrane lipids and/or membrane proteins. For illustration purposes, we present three main membrane integral proteins of erythrocytes: Aquaporin, Band3 and Glycophorin.

The absorption spectrum of free ICG consists of spectral peaks at 780 and 707 nm, corresponding to the monomeric and dimeric (H-like aggregate) forms of ICG (Fig. 25 (a)), consistent with the well-established spectra of diluted (μM level) ICG in distilled water29. In comparison to free ICG, the absorption spectrum of NETs has several differences: (1) increased absorbance values for $\lambda > 600$ nm, explained by the fact that higher ICG concentration was used to fabricate the NETs; (2) elimination of the previously distinct absorption peak associated with the H-like aggregate form of free ICG at 707 nm; (3) broadened absorption spectrum over the 600-935 nm band; and (4) bathochromic (red) shift from 780 to 783 nm (with respect to the spectral peak associated with the monomer form of ICG). We attribute these differences to the presence of various conformational states of ICG, and induced changes in molecular dipoles and

polarizability of ICG when encapsulated into these constructs (Fig. 25(b)). We offer further explanations in the discussion section.

5.3.3 Effects of incubation time on diameter of NETs, ICG loading efficiency, and optical absorption

During the last step of fabrication process, the EGs suspended in the hypotonic buffer solution are incubated with PBS-dissolved ICG. At this step, diameter of NETs can be manipulated by changing the incubation time of the EGs with ICG. All results presented in the main text of manuscript correspond to NETs fabricated with five minutes of ICG incubation time. Here, we present results to demonstrate the effects of incubation time (8, 10, and 15 minutes) on diameter of NETs, ICG loading efficiency, and optical absorption.

Extending the incubation time from five to eight minutes increased the estimated mean diameter ($\overline{d}_{\text{mean}}$) of the NETs from 134.78 nm (Fig. 24(a)) to 141.95 nm (Fig. 26(a)), as determined from the Lognormal fits to the measured diameters by dynamic light scattering. Further increases in the incubation time to 10 and 15 minutes resulted in broadening of size distribution. The measured diameter distribution of NETs fabricated after 10 minutes of incubation with ICG was fit with two Gaussian profiles. The $\overline{d}_{\text{mean}}$ values associated with the two Gaussian profiles were 167.1 and 338.37 nm. The $\overline{d}_{\text{mean}}$ value of the NETs fabricated after 15 minutes, as determined by the Lognormal fit, was 252.61 nm.

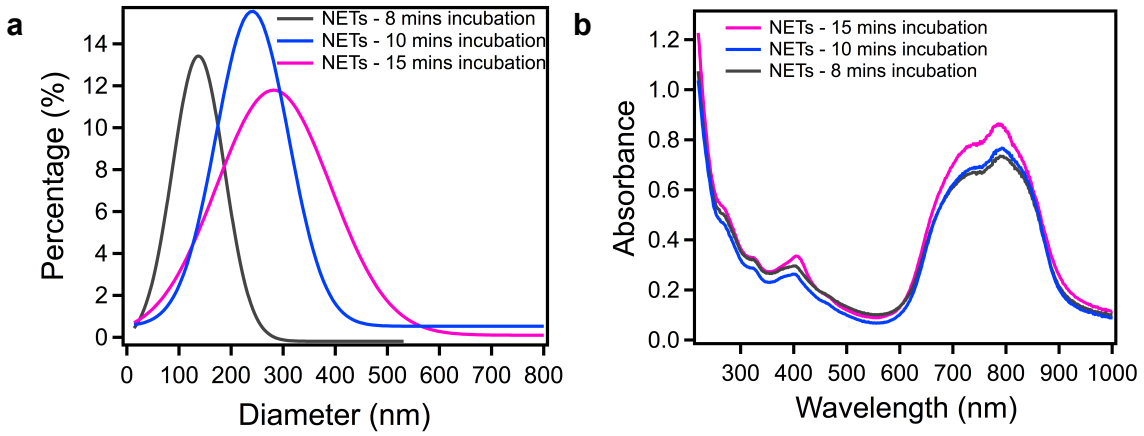

Figure 26 Effect of ICG incubation time on diameter distribution and absorption of NETs. a, Diameter distributions of NETs. Using dynamic light scattering, the respective ranges of the measured diameters were 91-225 nm (black triangles), 122-714 nm (blue rhombi), and 105-825 nm (magenta rhombi) for the NETs fabricated after 8, 10, and 15 minutes of incubation with ICG. Each measurement was repeated using at least three samples. We present the mean of each measurement, and standard deviations from the mean values (error bars). We fitted Lognormal functions to the measured diameter distributions (solid curves) to the NETs fabricated after 8 and 15 minutes of incubation with ICG. The respective estimated mean diameters, as determined from the Lognormal fits, were 141.95 nm (R^2 =0.98), and 252.61 nm (R^2 =0.94) for NETs fabricated after 8 and 15 minutes of incubation with ICG. The diameter distribution of NETs fabricated after 10 minutes of incubation with ICG was fit with two Gaussian curves. For the 1st Gaussian curve: estimated peak diameter = 167.1 nm, and R^2 = 0.96. For the 2nd Gaussian curve: estimated peak diameter = 338.37 nm, and R^2 = 0.94. b, Absorption spectra of NETs fabricated after 8, 10, and 15 minutes of ICG incubation time.

With increased ICG incubation time from 8 to 15 minutes, there was a corresponding increase in absorbance over the range of ≈ 660-840 nm (Fig. 26(b)). For example, the monomer absorbance value for NETs fabricated after 15 minutes increased by ≈ 14% from 0.73 to 0.85 as compared to the NETs fabricated after 8 minutes of incubation time.

To determine the loading efficiency of ICG into NETs, we first obtained the absorbance value of the ICG monomers within the supernatant after centrifugations at the

last step of NETs fabrication. We then compared this absorbance to a calibration curve that related the values of the ICG monomer absorbance to various concentrations of ICG dissolved in the mixture of PBS and hypotonic buffer solution. The loading efficiency was subsequently determined from the knowledge of the initial concentration of ICG introduced into the mixture solution, and the concentration remaining within the supernatant at the end of the fabrication process. The loading efficiencies of ICG into NETs fabricated after 5, 8, 10, and 15 minutes of incubation were 30%, 36%, 43%, and 45%, respectively.

5.3.4 ICG release kinetics from NETs

We investigated the release kinetics of ICG from NETs at physiological temperature. The suspension of NETs in PBS was stored at 37 °C for various time intervals (5, 10, 15, 30, 45 and 60 minutes) followed by centrifugation to pellet down the NETs. Three samples were tested for each time point. After centrifugation of the samples for 10 minutes at 14,000×g, we determined the concentration of ICG released from NETs and recovered from the supernatant by comparing the absorbance of the ICG monomeric form with calibration curve of ICG monomeric absorbance at different concentrations of ICG dissolved in the mixture of PBS and hypotonic buffer solution. The ICG release kinetics could be fitted by a rising exponential function (Fig. 27). The percentage of ICG released form NETs reached a plateau at nearly 60 minutes, with less than 5% ICG released at that time.

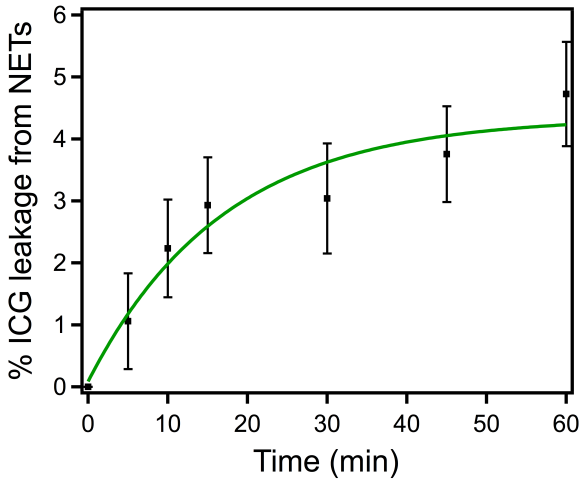

Figure 27 Release kinetics of ICG from the NETs suspension in PBS at 37 °C. The experimental value (squares) at each time point is the average of three experiments. Each error bar represents a single standard deviation. An exponential curve ($f(t) = k_1 - k_2 * \exp(-t/\tau)$), was fitted to the measured data ($R^2 = 0.99$) with $\tau = 16.96 \pm 2.78$ minutes, $k_1 = 4.35 \pm 2.2$ and $k_2 = 4.27 \pm 2.5$. We define τ as the time over which the mean value of ICG leaked from NETs increases by factor of *e*.

5.3.5 Fluorescence emission properties of NETs

The spectral peak of fluorescent emission from NETs in response to photo-excitation at 650 nm is at 695 nm, and originates from the aggregated forms of ICG within the constructs (Figure 28). Spectral peaks of fluorescence for free 3.22 μM ICG in response to 650 nm excitation are at 695 nm and 793 nm, and correspond to the H-like aggregate and monomeric forms of ICG, respectively. Fluorescence emission of free ICG at the higher concentration of 43 μM is quenched, and resembles that of the EGs, which do not contain ICG. We summarize the spectral features of the NETs fabricated under the protocol reported here in Table 1.

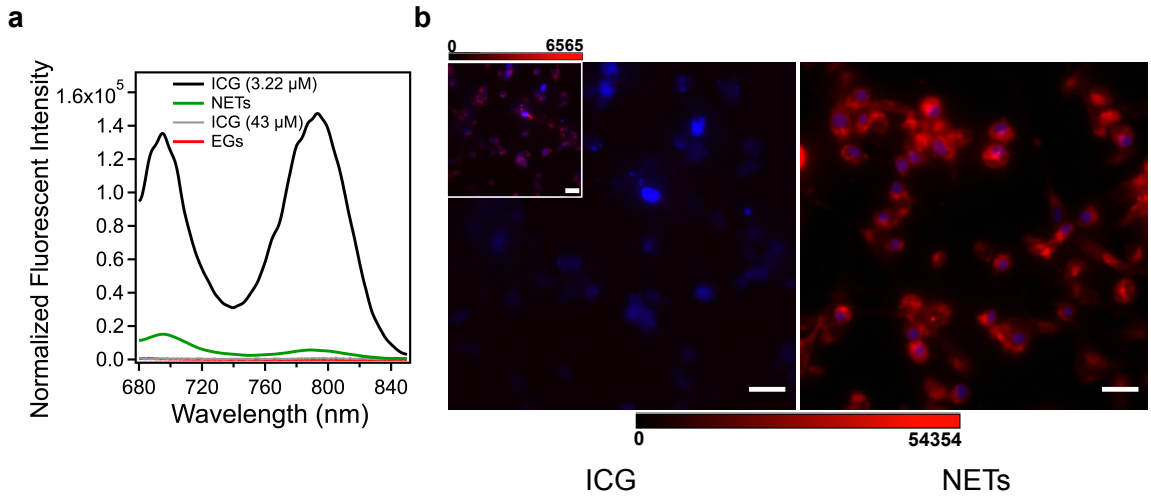

Figure 28 Fluorescence spectra and fluorescent images of human dermal microvascular endothelial (HDME) cells incubated with ICG or NETs. a, Normalized fluorescence spectra in response to 650 nm photo-excitation of free ICG (3.22 and 43 μM) dissolved in PBS, and EGs and NETs re-suspended in PBS. Emission spectra were smoothed using IGOR Pro software with second order binominal algorithm. b, Fluorescent images of HDME cells after three hours of incubation in vascular cell basal medium containing 13 μM ICG (control) dissolved in PBS (left panel), or NETs (right panel) at 37 °C and 5% CO_2 in dark. A Mercury/Xenon arc lamp was used for photo-excitation at 740 ± 35 nm. Cells nuclei were stained by DAPI, and falsely colored in blue using the ImageJ software. A filter transmitting λ>780 nm was used to collect the emitted NIR fluorescent, falsely colored in red.

Table 1
Spectral Features of 3.2 μM free ICG, and NETs*

Absorption peak of monomers in free ICG	780 nm
Absorption peak of ICG monomers in NETs	783 nm
Absorption peak of dimers (H-like aggregates) in free ICG	707 nm
Absorption peak of dimers (H-like aggregates) in NETs	Not distinct
Fluorescence peak of monomers in free ICG (650 nm excitation)	793 nm
Fluorescence peak of monomers in NETs (650 nm excitation)	790 nm
Fluorescence peak of dimers (H-like aggregates) in free ICG (650 nm excitation)	695 nm
Fluorescence peak of dimers (H-like aggregates) in NETs (650 nm excitation)	695 nm

* The spectral features of the NETs correspond to the constructs fabricated by 20 initial extrusions of EGs through 400 nm diameter porous membranes followed by 20 additional

extrusions through 100 nm diameter membranes, using 215 μM ICG in hypotonic buffer solution, and five minutes of incubating the EGs with ICG.

Human dermal micorvascular endothelial (HDME) cells were incubated with NETs or free ICG for three hours, and subsequently washed twice with PBS prior to fluorescent imaging induced by photo-excitation at 740 ± 35 nm spectral band provided by a Nikon Mercury/Xenon arc lamp. Co-registration of the NIR fluorescent emission from the constructs, and the visible fluoresce emitted by staining the nuclei of the cells produced images that suggest the NETs were internalized and localized to the nuclei periphery (Fig. 28(b)). The maximum NIR emission intensity from HDME cells incubated with free ICG (Fig. 28(b), left panel) was ≈ eight times lower than that from the cells incubated with NETs (Fig. 28(b), right panel). This result indicates that free ICG was not effectively uptaken by the HDME cells since most of it was removed after washing the cells. However, cell wash was not as effective in removing the NETs, indicating that the uptake of the NETs by the HDME cells was greater than ICG uptake.

5.3.6 Photothermal response of NETs, and NETs-mediated photothermal destruction of HDME cells

Temperature measurements indicate that NETs, suspended in PBS, are capable of eliciting a photothermal response in response to laser irradiation at 808 nm and incident intensity (I_o) of 19.7 W•cm^{-2} for 200 s (Fig. 29(a)); however, sustained laser irradiation was accompanied by a reduction in temperature. This result suggests that ICG within the NETs can be photo-degraded. To further investigate the photo-stability of NETs, we

obtained the absorption spectra of the NETs following laser irradiation at 808 nm and I_o = 19.7 W•cm^{-2} for different radiant exposure times (60 s-200 s). There was a progressive reduction in the absorption of NETs over the 630-950 nm spectral band, and increased UV absorption at 213 and 245 nm with increasing radiant exposure time (Fig. 29(b)).

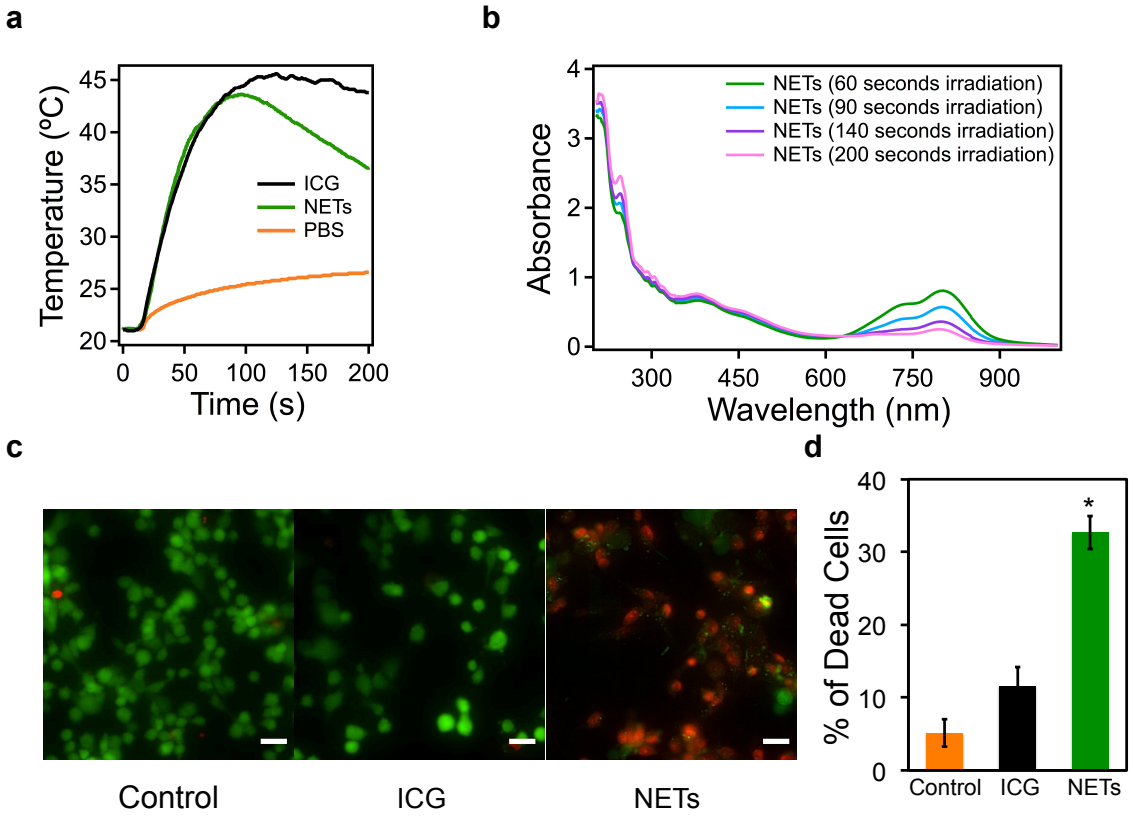

Figure 29 Photothermal response of NETs, and NETs-mediated photothermal destruction of HDME cells. a, Photothermal response of NETs suspended in PBS, 13 µM free ICG dissolved in PBS (positive control), and PBS solution (negative control) in response to laser irradiation at λ = 808 nm with incident intensity (Io) of 19.7 W•cm^{-2}. The volume of all samples was 120 µl. The free ICG solution and NETs suspension samples were prepared to have nearly the same absorbance value of 0.6 at 808 nm. Temperatures were measured using a thermistor placed 2 mm outside the irradiated spot. c, Fluorescent images of HDME cells after three hours of incubation with PBS (negative control), 13 µM free ICG (positive control) and NETs, followed by laser irradiation (λ=808 nm, Io = of 19.7 W•cm^{-2}).The radiant exposure time in all three samples was 200 s. The volume of NETs suspension or free ICG added to the cells was 200 µl with nearly the same absorbance value of 0.6 at 808 nm. Live cells were stained using Calcein, and falsely

colored in green. Dead cells were distinguished using Ethidium homodimer-1 (EthD-1), and falsely colored in red (Scale bars =10 μm). d, Percentage of HDME cells photothermally destroyed by NETs as assessed by a fluorescence microplate reader. Three different spots (each spot diameter = 2.2 mm) were irradiated in each well, resulting in irradiation of ≈ 80% of cells. Scale bars on both panels correspond to 10 μm. The scale bar, 0-54354, corresponds to the NIR fluorescent emission intensity for both panels. The inset on the left panel represents the same image shown on the panel at the scale of 0-6565. b, Absorbance spectra of four different PBS-suspended NETs samples (each 120 μl) following laser irradiation for various durations (60, 90, 140, and 200 s) at 808 nm and Io = 19.7 W/cm^2. Each bar represents the mean fraction of the dead cells for three different wells. Error bars correspond to single standard deviations. There was a statistically significant difference in fraction of cells photothermally destroyed by NETs (identified by the asterisk) as compared to those incubated in PBS or free ICG (p-value $<10^{-4}$).

HDME cells were incubated with NETs or free ICG (positive control) for three hours, and subsequently washed twice with PBS prior to laser irradiation at 808 nm laser irradiation with I_o = 19.7 W•cm^{-2} for 200 s. Cells incubated in PBS without exposure to NETS or ICG were used as the negative control population. Live/dead assays demonstrate that NETs are capable of mediating photothermal destruction of the HDME cells (Fig. 29(c)). There was a statistically significant difference ($p < 10^{-4}$) between the fraction of photo-thermally destroyed HDME cells incubated after three hours of incubation with NETs, and those incubated with free ICG or PBS (Fig. 29(d)). The results presented in Fig. 28(b), 29(c), and 29(d) collectively demonstrate the effectiveness of NETs as photo-theranostic agents for combined fluorescence imaging and photothermal destruction.

5.3.7 Effects of cyclic laser irradiation

To investigate the heat generating ability of the NETs to repeated laser exposure, we irradiated the NETs using a cyclic irradiation pattern. PBS-suspended NETs (120 µl solution) were irradiated at 808 nm using a spot diameter of 2.2 mm, and incident irradiance (I_o) of 19.7 W/cm^2 for 60 s followed by 30 s of no laser exposure. We repeated this cycle of irradiation five times. As the positive control sample, we irradiated 120 µl of PBS solution containing 13 µM of ICG using the same laser irradiation parameters and cycles. The negative control sample was 120 µl of PBS solution without any additional reagents irradiated under the same conditions. NETs suspended in PBS, and ICG dissolved in PBS had the same absorbance value (0.6) at 808 nm.

Temperature changes in the solution were measured using a thermistor placed 2 mm outside the irradiation spot and connected to a Vernier LabQuest. The peak temperature associated with both the NETs and ICG samples at the end of each 60 s of laser irradiation progressively decreased (Fig. 30). The percentage reduction in the peak temperature at the end of the first 60 s to the end of the 5th 60 s of laser irradiation for the solution containing the NETs was ≈ 24%. For the solution containing free ICG, the percentage reduction in the peak temperature over the same time interval was ≈ 21%.

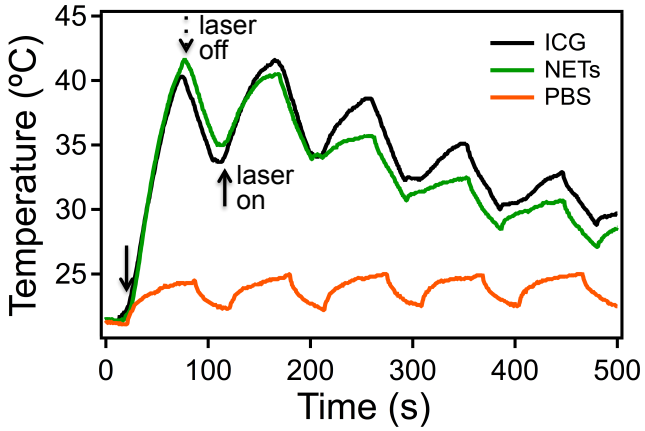

Figure 30 Temperature measurements in response cyclic 808 nm laser irradiation. Samples (120 µl) of PBS solution without any additional reagents (negative control), containing 13 µM free ICG (positive control), or NETs were irradiated at I_o = 19.7 W/cm^2. Temperatures were measured using a thermistor placed 2 mm outside the 2.2 mm irradiated spot (2.2 diameter). Samples were irradiated for 60 seconds, followed by 30 seconds of no irradiation. Irradiation cycle was repeated five times. Solid arrows point to illustrative times when laser irradiation was turned on. Dotted arrow points to an illustrative time when laser irradiation was turned off.

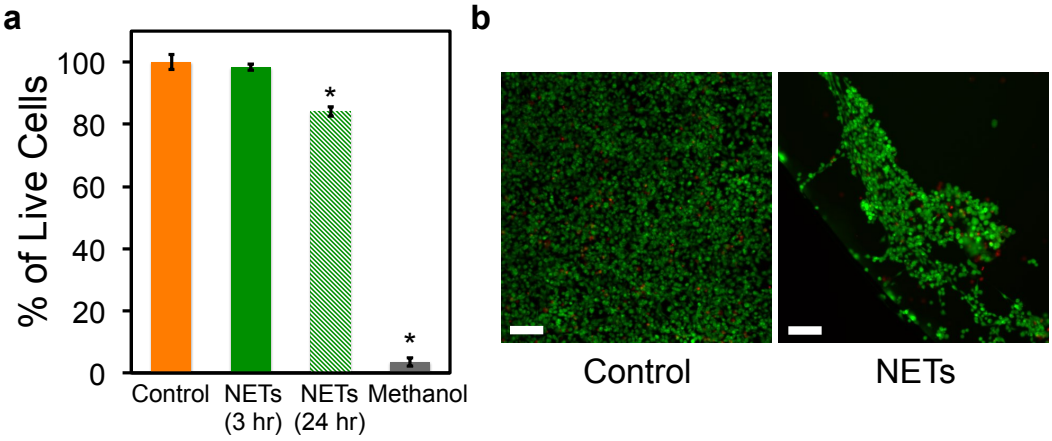

Figure 31 Cytotoxicity assessment of NETs. a, Percentage of live cells post incubation with NETs for 3 hours (solid green bar) and 24 hours (dashed green bar). Cells incubated with culture medium for 24 hours without any additional reagent were used as the positive control population. Cells incubated with 100 µl methanol for 24 hours were used as negative control. Each bar represents the mean fraction of the live cells for three different wells. Error bars correspond to single standard deviations. Statistical analysis of the results for NETs (3 hours) compared to positive control yielded no significant difference in cell viability. Cells treated with methanol (negative control) and NETs for

24 hours (identified by asterisks) yielded statistically significant viability results as compared to the positive control population (p-value<10^{-3}). Fraction of the viable cells treated with NETs for 24 hours was significantly higher than those treated with methanol (p-value<10^{-4}). b, Fluorescent images of HDME cells 24 hours post incubation with NETs (right panel) and culture medium (positive control) (right panel). Live cells were stained using Calcein, and falsely colored in green. Dead cells were distinguished using Ethidium homodimer-1 (EthD-1), and falsely colored in red (Scale bars =100 μm).

To evaluate the potential cytotoxicity of the NETs, we incubated the HDME cells for three and 24 hours in the culture medium containing the NETs at effective dosage (D_{eff}) of 12 ml^{-1} suspended in PBS (see Methods section for definition of D_{eff}). Nearly all the HDME cells remained viable after three hours of incubation with NETs at D_{eff} = 12 ml^{-1} (Fig. 31(a)). After 24 hours of incubating the HDME cells with NETs at D_{eff} = 12 ml^{-1}, nearly 80% of the cells remained viable. In comparison, there was more than 90% cell death following 24 hours of incubation with methanol as the positive control. Illustrative fluorescent image of the HDME cells demonstrate the viability of most of the cells after 24 hours of incubation with NETs at D_{eff} = 12 ml^{-1} (Fig. 31(b)).

Spectral broadening of the NETs absorption, and the elimination of a distinct dimeric (H- like aggregate) peak are indicative of different conformations of ICG. Specifically, when ICG is incorporated into the EGs, an ensemble of ICG conformational states comprised of ICG monomers, ICG aggregates, and monomers and aggregates of ICG bound to membrane lipids and/or membrane proteins can form (Fig. 25(b)). The excited energy levels associated with these ICG ensemble components, confined within the nano-scale volume of NETs, can be different than those associated with non-

encapsulated (free) ICG. The effective NIR absorption cross section of the ensemble ($\sigma_{ensemble}$), which is directly related to NIR absorbance of the NETs, can be expressed as:

$$\sigma_{ensemble}(\lambda) = f_M\sigma_M(\lambda) + f_A\sigma_A(\lambda) + \sum_{i=1}^{n} f_{M_i^B}\sigma_{M_i^B}(\lambda) + \sum_{i=1}^{n} f_{A_i^B}\sigma_{A_i^B}(\lambda)$$

where f_M and f_A are the respective fractions of the monomeric and aggregated forms of ICG in the ensemble; σ_M and σ_A are the absorption cross sections of the monomeric and aggregated forms of ICG respectively; $f_{M_i^B}$ and $f_{A_i^B}$ are the respective fractions of the ensemble comprised of the monomeric and aggregated forms of ICG bound to a given membrane-associated molecule (i); $\sigma_{M_i^B}$ and $\sigma_{A_i^B}$ are the absorption cross sections of the monomeric and aggregated forms of bound ICG, respectively.

The observed bathochromic shift of the monomer absorbance in NETs is indicative of the changes in molecular dipoles and polarizability of ICG. We use the exciton theory for molecular assemblies to explain the origin of this bathochromic shift.[154] In accordance with this theory, the excitonic state of the ICG monomer bound to membrane lipids or proteins can split into two levels (E" and E'). The in-phase arrangement of transition dipoles leads to an electrostatic attraction that produces the lower excited state (E'). Photo-excitation of the bound monomer produces a transition from ground to E', resulting in a bathochromic shift for the bound ICG monomer. A similar bathochromic shift in the monomer absorbance is reported for ICG dissolved in aqueous solution containing human serum albumin, and attributed to the interaction between albumin and ICG.[151]

Fluorescence spectra in response to photo-excitation at 650 nm demonstrate that the emission intensity at 790 nm, associated with the monomer form of ICG in NETs, is diminished in comparison with the emission intensity of 3.22 μM free ICG at 793 nm (Fig. 28(a)). The 650 nm excitation wavelength does not correspond to the spectral peaks associated with the monomeric forms of ICG in its free form or in the NETs (Fig. 25(a)). The fact that in response to 650 nm excitation, we still observed a distinct fluorescence emission peak at 793 nm from the monomeric form of 3.22 μM free ICG, which was more intense than that from the monomer form of ICG in NETs, suggests that the fraction of ICG in its aggregated is greater than its monomeric fraction within the NETs. However, in the 3.2 μM free ICG solution, there were sufficient number of monomers to elicit fluorescence emission.

While fluorescence is quenched in the case of 43 μM free ICG, NETs are still fluorescent despite the fact that they were fabricated using 215 μM ICG (with loading efficiency of 30% to give an effective loaded concentration of 64.5 μM distributed into the population of the constructs) (Fig. 28(a)). This result suggests that the presence of the erythrocyte-derived membrane, as an encapsulating shell, protected the entrapped ICG molecules within each NET from interactions with other such entrapped ICG molecules to ultimately prevent fluorescence quenching. While ICG molecules still form aggregates within the NETs, the effective concentration of such aggregates within the NETs fabricated under the protocols described herein, was not sufficient to induce fluorescence quenching that would otherwise take place at high (e.g., 43 μM) concentrations of free ICG in solution. Therefore, by loading the ICG into the NETs, higher ICG concentrations

that could otherwise results in fluorescence quenching of its free form, may be used. In our future studies, we will characterize the effects of ICG concentration over a broad range on the resulting excitation-emission spectra of the NETs and fluorescence quantum yields.

Continuous laser irradiation at the specific parameters investigated here can result in photo-degradation of the NETs (Fig. 29(b)). The progressive increase in absorbance values at the spectral peaks of 213 and 244 nm with increased radiant exposure time is indicative of the conformational changes in the membrane proteins of the NETs due to photothermal denaturation. Our observed progression in reduction of the NET's NIR absorption with sustained laser irradiation can result from photo-addition to the alternating double bonds in the polyene bridge of the ICG molecule to produce a leuco form of the dye with converted sp^2 to sp^3 carbon hybridization, and/or induce cleavage of the π–conjugation along the bridge while keeping the aromatic benzoindotricarbocyanine moieties intact. The observation that NETs appeared somewhat more susceptible to photo-degradation than free ICG (Fig. 29(b) and 30) suggests that entrapment of ICG within the NETs may weaken the alternating double bonds along the polyene bridge, and/or alter its electronic localization and polarizability, a proposition consistent with the excitonic theory described earlier. Our results are in agreement with those reported by Holzer *et al*. where there were progressively increased optical transmissions (i.e., lower absorption) through various solvents (e.g., H_2O, D_2O, human plasma) containing free ICG as the laser exposure time increased.[155] For example, these investigators reported nearly 12% increase in transmission of 785 nm light through a sample containing 10 μM

ICG dissolved in H_2O after 600 s of laser irradiation at this wavelength and I_o = 0.17 mW•cm^{-2}; transmission subsequently increased to about 25% after 2,400 s of laser irradiation.[155]

The major potential advantages of NETs as compared to other types of dye-loaded nano-constructs are their safety, and longevity within the circulation. As constructs that can be engineered autologously, NETs offer the potential of being biodegradable, and non-immunogenic photo-theranostic platforms for use in personalized nanomedicine. Flower et al. reported no immune or allergic responses, even after multiple injections of ICG-loaded EGs into monkeys and rabbits despite the fact human-derived erythrocytes were used to fabricate the constructs.[153]

The natural lifetime of erythrocytes in systemic circulation is on the order of 90-120 days. While further studies are needed to determine the biodistribution and vascular retention time of NETs, the reported circulation times of erythrocytes-based carrier systems exceed those of synthetic vectors, which are on the order of several hours (e.g., <10 hours for polyethylene glycol-liposomes with diameters in the range of 50-500 nm).[144] Hu et al., investigated the circulation dynamics of nano-constructs (≈ 80 nm diameter) composed of a poly (lactic-co-glycolic acid) core coated with erythrocyte-derived membranes in mice.[156] The investigators reported that the constructs were retained in blood for three days with circulation half-life of nearly 40 hours.[146,156] In a clinical study, patients with acute lymphoblastic leukemia (ALL) were injected with erythrocytes encapsulating L-asparaginase (L-ASNase) to treat ALL. L-ASNase loaded erythrocytes were still detectable within the vasculature at 24 days following the first

injection.[157] As compared to non-encapsulated L-ASNase, the investigators reported a reduction in the number and severity of allergic reactions in those patients receiving the L-ASNase loaded erythrocytes.

In another study, 20 patients with ulcerative colitis received autologously-derived erythrocytes encapsulating dexamethasone 21-P (Dex 21-P) as the therapeutic agent.[158] At 14 days post-infusion, there were still detectable levels of Dex 21-P within the plasma. There were no steroid-related adverse effects in patients treated with erythrocyte encapsulating Dex 21-P as compared to 8 of the 10 patients receiving oral steroids.

5.4 CONCLUSION

In summary, we have engineered a new type of optical nano-construct composed of erythrocyte-derived membranes encapsulating the organic NIR chromophore, ICG. To- date, only iron oxide nanoparticles are approved by the FDA for use in conjunction with MRI. There are currently no FDA-approved nano-constructs as contrast agents for use in optical imaging modalities, and furthermore, as a photo-theranostic material for combined optical imaging and phototherapy. Given the existing FDA-approved status of ICG and prior clinical studies with erythrocytes-based delivery systems, NETs present a promising photo-theranostic candidate for clinical translation. For example, the enhanced permeability and retention effect in tumors may provide the basis for the delivery of NETs into tumors. Since particles with diameters < 200 nm are more effective for extravasation into tumors,[80] NETs may prove a suitable material for combined optical imaging and photothermal destruction of tumors. Other potential applications may

include dynamic imaging and photo-destruction of vascular abnormalities, and longitudinal evaluations to assess therapeutic interventions.

CHAPTER 6: CONCLUSION

This study describes development of two different types of thernaostic nano-constrcuts loaded with indocyanine green with optical diagnostic and phototherapeutic applications. In the second chapter, we demonstrated reduced phagocytic content of PEGylated polymeric nanocapsules loaded with ICG through in-vitro studies using human spleen macrophages. Low molecular weight PEG (5,000 Da) lowered the ICG-NCs content within human spleen macrophages up to 90 minutes as compared with the high molecular weight PEG (30,000 Da). For longer incubation times, there was no statistically significant difference in phagocytic content of ICG-NCs coated with either the high or low molecular weight PEG. Encapsulation within the polymeric nanocapsules reduced the hepatic content of ICG with normal human hepatocytes up to two hours, while the molecular weight of PEG did not have a statistically significant effect on the content of ICG-NCS in liver cells. Results of these *in-vitro* studies specify the promising role of PEG coating as a method to prolong the vascular circulation time and reduce the clearance of ICG-NCs by RES.

We showed prolonged blood circulation time and delayed hepatic accumulation of ICG when loaded into polymeric nanocapsules and coated with PEG (MW=5 KDa) in third chapter. The biodistribution of PEGylated ICG-NCs in healthy mice was assessed using whole-body fluorescent imaging and individual organ uptake analysis. The prolonged vascular circulation time of ICG achieved through PEGylation of ICG-loaded NCs could introduce new possibilities for ICG clinical applications. First of all, by loading ICG into PEGylated NCs, we can overcome the rapid clearance of ICG from

vasculature. Second, the surface of ICG-NCs can be coated with different materials or functionalized with various targeting moieties. The concurrent increased bioavailability of ICG and possibility to functionalize ICG-NCs provides the potential to use ICG-NCs as theranostic nano-constructs for targeted optical imaging of specific molecular biomarkers of a disease and phototherapy.

One of the applications of ICG-NCs as theranostic nano-constructs studied here was targeted fluorescent imaging and laser-mediated phototherapy of ovarian cancer. Due to the lack of efficient and precise screening methods, ovarian cancer has remained the number one cause of cancer related death among women in United States. In chapter 4, we showed effectiveness of functionalization of ICG-NCs in targeting HER2 receptors on the surface of ovarian cancer cells in-vitro. The quantification of intracellular uptake of anti-HER2 functionalized ICG-NCs using flow cytometry demonstrated significantly higher uptake by SKOV3 cells compared to non-functionalized ICG-NCs and freely dissolved ICG. After three hours incubation of anti-HER2 functionalized ICG-NCs with SKOV3 cells, majority of cells interacted with functionalized nanocapsules and were detected as ICG positive. Cell viability analysis of SKOV3 cells after laser treatment showed about 80% death for cells incubated with anti-HER2 functionalized ICG-NCs. These levels of cell death was significantly higher than that associated with the population of the cells incubated with non-functionalized ICG-NCs. Our results are very promising and demonstrate the capabilities of anti-HER2 functionalized ICG-NCs to be used as theranostic agents for intraoperative fluorescent imaging and laser-induced

photodestruction of ovarian cancer cells. Targeted imaging and phototherapy of ovarian cancer can enhance detection, improve treatment and increase patients survival rate.

In the last chapter, we introduced engineering of a new type of biological optical theranostic nano-construct made of erythrocyte-derived membranes for the first time. These nano-constructs were loaded with ICG and we named them NETs. The major advantages of loading ICG into erythrocyte-derived membranes over other types of nano-constructs are safety and lastingness within the vasculature. Moreover, less than 5% of ICG leaks out of NETs in one hour and seems to reach a plateau at 5%. NETs were successfully used for fluorescent imaging of human dermal microvascular endotheial cells (HDME) in-vitro. We showed NETs can generate heat in response to continuous 808 nm laser irradiation and demonstrated such temperature increases were enough to destroy HDME cells. Therefore, NETs are promising candidates of photo-theranostic nano-constructs to be used in personalized nanomedicine for dynamic imaging and photo-destruction of vascular abnormalities, and longitudinal evaluations to assess therapeutic interventions.

REFERENCES

1. Landsman ML, Kwant G, Mook GA, Zijlstra WG. stabilization of indocyanine green Light-absorbing properties , stability , spectral stabilization of indocyanine. 2013:575–583.

2. Benson RC, Kues H a. Fluorescence properties of indocyanine green as related to angiography. *Physics in medicine and biology*. 1978;23(1):159–63.

3. Webster JG. Measurement of Flow and Volume of Blood. In: Webster G, ed. *Medical Instrumentation: Application and Design*. John Wiley & Sons, Inc. 1998.

4. El-Desoky a, Seifalian a M, Cope M, Delpy DT, Davidson BR. Experimental study of liver dysfunction evaluated by direct indocyanine green clearance using near infrared spectroscopy. *The British journal of surgery*. 1999;86(8):1005–11.

5. Desmettre T, Devoisselle JM, Mordon S. Fluorescence Properties and Metabolic Features of Indocyanine Green (ICG) as Related to Angiography. *Surv Ophthalm*. 2000;45(1).

6. Scharschmidt B.F. WJG, Berk PD. Hepatic organic anion uptake in the rat. *Journal of Clinical Investigation*. 1975;56(5):1280–1292.

7. Paumgartner G, Probst P, Kraines R, Leevy CM. Kinetics of Indocyanine Green Removal from the Blood. *Annals of the New York Academy of Sciences*. 1970;170:134–147.

8. Mordon S, Devoisselle JM, Begu S, Desmettre T. Laser-Induced Release of Liposome-Encapsulated Dye: A New Diagnostic Tool. *Lasers in Medical Science*. 1998;13(3):181–188.

9. Kim G, Huang S-W, Day KC, et al. Indocyanine-green-embedded PEBBLEs as a contrast agent for photoacoustic imaging. *Journal of biomedical optics*. 2007;12(4):044020.

10. Rodriguez VB, Henry SM, Hoffman AS, Stayton PS, Li X, Pun SH. Encapsulation and stabilization of indocyanine green within poly(styrene-alt-maleic anhydride) block-poly(styrene) micelles for near-infrared imaging. *Journal of biomedical optics*. 2008;13(1):014025.

11. Yaseen M a, Yu J, Wong MS, Anvari B. Stability assessment of indocyanine green within dextran-coated mesocapsules by absorbance spectroscopy. *Journal of biomedical optics*. 2007;12(6):064031.

12. Yu J, Yaseen MA, Anvari B, Wong MS, Chemical D, Engineering B. Synthesis of Near-Infrared-Absorbing Nanoparticle-Assembled Capsules. *Chem Mater*. 2007;19(6):1476–1483.

13. Yaseen M a, Yu J, Wong MS, Anvari B. Laser-induced heating of dextran-coated mesocapsules containing indocyanine green. *Biotechnol Prog*. 2007;23(6):1431–1440.

14. Yaseen M a, Yu J, Wong MS, Anvari B. In-vivo fluorescence imaging of mammalian organs using charge-assembled mesocapsule constructs containing indocyanine green. *Optics express*. 2008;16(25):20577–87.

15. Yaseen M a, Yu J, Jung B, Wong MS, Anvar. Biodistribution of Encapsulated Indocyanine Green in Healthy Mice. *Mol Pharm*. 2009;6(5):1321–1332.

16. Yu J, Javier D, Yaseen M a, et al. Self-assembly synthesis, tumor cell targeting, and photothermal capabilities of antibody-coated indocyanine green nanocapsules. *J Am Chem Soc*. 2010;132(6):1929–38.

17. Hashida PDM, Opanasopit P, Nishikawa M. Factors Affecting Drug and Gene Delivery: Effects of Interaction with Blood Components. *Critical Reviews™ in Therapeutic Drug Carrier Systems*. 2002;19(3):44.

18. Li S, Huang L. Pharmacokinetics and Biodistribution of Nanoparticles. *Mol Pharm*. 2008;5(4):496–504.

19. Owens DE, Peppas N a. Opsonization, biodistribution, and pharmacokinetics of polymeric nanoparticles. *International journal of pharmaceutics*. 2006;307(1):93–102.

20. Kaul G, Amiji M. Long-circulating poly(ethylene glycol)-modified gelatin nanoparticles for intracellular delivery. *Pharmaceutical research*. 2002;19(7):1061–7.

21. Zahr AS, Davis C a, Pishko M V. Macrophage uptake of core-shell nanoparticles surface modified with poly(ethylene glycol). *Langmuir : the ACS journal of surfaces and colloids*. 2006;22(19):8178–85.

22. Jeon SI, Lee JH, Andrade JD, Gennes PG De. Protein-Surface Interactions in the Presence of Polyethylene Oxide 1. Simplified Theory. *Journal of Colloid and Interface Science*. 1991;142(1):149–158.

23. Cancer Facts & Figures. *American Cancer Society*. 2011.

24. Holschneider CH, Berek JS. Ovarian Cancer : Epidemiology , Biology , and Prognostic Factors. *Seminars in Surgical Oncology*. 2000;19:3–10.

25. Van Dam GM, Themelis G, Crane LM a, et al. Intraoperative tumor-specific fluorescence imaging in ovarian cancer by folate receptor-α targeting: first in-human results. *Nature medicine*. 2011;17(10):1315–9.

26. Hirsch LR, Gobin AM, Lowery AR, et al. Metal nanoshells. *Annals of biomedical engineering*. 2006;34(1):15–22.

27. Moin K, McIntyre OJ, Matrisian LM, B.F. S. Fluorescent Imaging of Tumors. In: Shields AF, Price P, eds. *In vivo imaging of cancer therapy*. Humana Press; 2007:281–302.

28. Sun C, Yang J, Li L, Wu X, Liu Y, Liu S. Advances in the study of luminescence probes for proteins. *Journal of chromatography. B, Analytical technologies in the biomedical and life sciences*. 2004;803(2):173–90.

29. Hamblin MR, Demidova TN. Mechanisms of low level light therapy. In: Hamblin MR, Waynant RW, Anders J, eds. *Mechanisms for Low-Light Therapy*. SPIE; 2006:614001–614013.

30. Patonay G, Strekowski L, Raszkiewicz A, Kim JS. Near-Infrared Probes: Design and Applications. Achilefu S, Bornhop DJ, Raghavachari R, eds. 2006;6097:609709–609709–9.

31. Jaiswal JK, Simon SM. Potentials and pitfalls of fluorescent quantum dots for biological imaging. *Trends in cell biology*. 2004;14(9):497–504.

32. Michalet X, Pinaud F, Lacoste TD, et al. Properties of Fluorescent Semiconductor Nanocrystals and their Application to Biological Labeling. 2001;2:261–276.

33. Park J, Estrada A, Sharp K, et al. imaging of tumors using near-infrared excited gold nanoshells. 2008;16(3):214–221.

34. Altınoglu EI, Adair JH. Near infrared imaging with nanoparticles. *Wiley Interdisciplinary Reviews: Nanomedicine and Nanobiotechnology*. 2010;2(5):461–477.

35. Altinoğlu EI, Russin TJ, Kaiser JM, et al. Near-Infrared Emitting Fluorophore- for In Vivo Imaging of Human Breast. 2008;2(10):2075–2084.

36. Abels C, Fickweiler S, Weiderer P, et al. Indocyanine green (ICG) and laser irradiation induce photooxidation. *Archives of dermatological research*. 2000;292(8):404–11.

37. Babilas P, Shafirstein G, Baier J, et al. Photothermolysis of blood vessels using indocyanine green and pulsed diode laser irradiation in the dorsal skinfold chamber model. *Lasers in surgery and medicine*. 2007;39(4):341–52.

38. Yaseen M a., Diagaradjane P, Pikkula BM, Yu J, Wong MS, Anvari B. Photothermal and Photochemical Effects of Laser Light Absorption by Indocyanine Green (ICG). Jacques SL, Roach WP, eds. *Proceeding of SPIE*. 2005;5695:27–35.

39. Genina E a, Bashkatov AN, Simonenko G V, Odoevskaya OD, Tuchin V V, Altshuler GB. Low-intensity indocyanine-green laser phototherapy of acne vulgaris: pilot study. *Journal of biomedical optics*. 2004;9(4):828–34.

40. Rho NK, Lee DK, Kim S, Lee DP, Jeong CW. Efficacy of acne treatment using a combination of radiofrequency energy and indocyanine green-mediated pulsed light phototherapy. *Laser in Surgery and Medicine*. 2008;40:32.

41. Urbanska K, Romnaowska-Dixon B, Matuszak Z, Oszajca J, Nowak-Sliwinska P, Stochel G. Indocyanine green as a prospective sensitizer for photodynamic therapy of melanomas. *Acta Biochem. Pol.* 2002;49(2):387–391.

42. Tseng WW, Saxton RE, Deganutti A, Liu CD. Infrared laser activation of indocyanine green inhibits growth in human pancreatic cancer. *Pancreas*. 2003;27(3):e42–5.

43. Bozkulak O, Yamaci RF, Tabakoglu O, Gulsoy M. Photo-toxic effects of 809-nm diode laser and indocyanine green on MDA-MB231 breast cancer cells. *Photodiagnosis and photodynamic therapy*. 2009;6(2):117–21.

44. Bäumler W, Abels C, Karrer S, et al. Photo-oxidative killing of human colonic cancer cells using indocyanine green and infrared light. *British journal of cancer*. 1999;80(3-4):360–3.

45. Mauerer M, Penzkofer A, Zweck J. Dimerization , J-aggregation and J-disaggregation dynamics of indocyanine green in heavy water. 1998;20.

46. Philip R, Penzkofer A, Biiumler W, Szeimies RM, Abels C. Absorption and fluorescence spectroscopic investigation of indocyanine green. 1996;96:137–148.

47. Saxena V, Sadoqi M, Shao J. Degradation kinetics of indocyanine green in aqueous solution. *Journal of pharmaceutical sciences*. 2003;92(10):2090–7.

48. Baker KJ. Binding of sulfobromophthalein (BSP) sodium and indocyanine green (ICG) by plasma α1-lipoprotein. *Proc Soc Exp Biol Med.* 1966;122:957–63.

49. Kamisaka K, Yatsuji Y, Yamada H, Kameda H. The binding of indocyanine green and other organic anions to serum proteins in liver diseases. *Clinica chimica acta; international journal of clinical chemistry*. 1974;53(2):255–64.

50. Sakka SG, Koeck H, Meier-Hellmann A. Measurement of indocyanine green plasma disappearance rate by two different dosages. *Intensive Care Med*. 2004;30(3):506–9.

51. Sakka SG, Van Hout N. Relation between indocyanine green (ICG) plasma disappearance rate and ICG blood clearance in critically ill patients. *Intensive care medicine*. 2006;32(5):766–9.

52. Saxena V, Sadoqi M, Shao J. Enhanced photo-stability, thermal-stability and aqueous-stability of indocyanine green in polymeric nanoparticulate systems. *Journal of photochemistry and photobiology. B, Biology*. 2004;74(1):29–38.

53. Gomes AJ, Lunardi LO, Marchetti JM, Lunardi CN, Tedesco AC. Indocyanine Green Nanoparticles Useful for Photomedicine. *Photomedicine and Laser Surgery*. 2006;24(4):514–521.

54. Desmettre TJ, Soulie-Begu S, Devoisselle JM, Mordon SR. Diode laser-induced thermal damage evaluation on the retina with a liposome dye system. *Laser Surg Med*. 1999;24(1):61–8.

55. Opanasopit P, Nishikawa M, Hashida M. Factors affecting drug and gene delivery: effects of interaction with blood components. *Crit Rev Ther Drug Carrier Syst.* 2002;19(3):191–233.

56. Alexis F, Pridgen E, Molnar LK, Farokhzad OC. reviews Factors Affecting the Clearance and Biodistribution of Polymeric Nanoparticles. 2008;5(4):505–515.

57. Illum L, Davis S, Müller R, Mak E, West P. The organ distribution and circulation time of intravenously injected colloidal carriers sterically stabilized with a block copolymer--poloxamine 908. *Life Science*. 1987;40(4):367–374.

58. Illum L, Davis SS. The organ uptake of intravenously administered colloidal particles can be altered using a non-ionic surfactant (Poloxamer 338). *FEBS letters*. 1984;167(1):79–82.

59. Kaul G, Amiji M. Biodistribution and targeting potential of poly(ethylene glycol)-modified gelatin nanoparticles in subcutaneous murine tumor model. *Journal of drug targeting*. 2004;12(9-10):585–91.

60. Chapman RG, Ostuni E, Takayama S, Holmlin RE, Yan L, Whitesides GM. Surveying for Surfaces that Resist the Adsorption of Proteins. 2000;(16):8303–8304.

61. Israelachvili J. Commentary The different faces of poly (ethylene glycol). 1997;94(August):8378–8379.

62. Gref R, Minamitake Y, Peracchia MT, Trubetskoy V, Torchilin V, Langerll R. Biodegradable long-circulating polymeric nanospheres. *Science*. 1994;263(5153):1600–1603.

63. Gref R, Lück M, Quellec P, et al. "Stealth" corona-core nanoparticles surface modified by polyethylene glycol (PEG): influences of the corona (PEG chain length and surface density) and of the core composition on phagocytic uptake and plasma protein adsorption. *Colloids Surf B Biointerfaces*. 2000;18(3-4):301–313.

64. Yang Z, Galloway J a., Yu H. Protein Interactions with Poly(ethylene glycol) Self-Assembled Monolayers on Glass Substrates: Diffusion and Adsorption. *Langmuir*. 1999;15(24):8405–8411.

65. Roosjen A, Van der Mei HC, Busscher HJ, Norde W. Microbial adhesion to poly(ethylene oxide) brushes: influence of polymer chain length and temperature. *Langmuir : the ACS journal of surfaces and colloids*. 2004;20(25):10949–55.

66. Wan J, Thomas MS, Guthrie S, Vullev VI. Surface-bound proteins with preserved functionality. *Ann Biomed Eng*. 2009;37(6):1190–205.

67. Zoulalian V, Zürcher S, Tosatti S, Textor M, Monge S, Robin J-J. Self-assembly of poly(ethylene glycol)-poly(alkyl phosphonate) terpolymers on titanium oxide surfaces: synthesis, interface characterization, investigation of nonfouling properties, and long-term stability. *Langmuir : the ACS journal of surfaces and colloids*. 2010;26(1):74–82.

68. Pantusa M, Sportelli L, Bartucci R. Spectroscopic and calorimetric studies on the interaction of human serum albumin with DPPC/PEG:2000-DPPE membranes. *European biophysics journal : EBJ*. 2008;37(6):961–73.

69. Xu Z, Holland NB, Marchant RE. Conformations of Short-Chain Poly(ethylene oxide) Lipopolymers at the Air−Water Interface: A Combined Film Balance and Surface Tension Study. *Langmuir*. 2001;17(2):377–383.

70. Harder P, Grunze M, Dahint R, Heidelberg D. Molecular Conformation in Oligo (ethylene glycol) -Terminated Self-Assembled Monolayers on Gold and Silver Surfaces Determines Their Ability To Resist Protein Adsorption. *J Phys Chem B*. 1998;5647(97):426–436.

71. Baxter EW, Reitz AB. Reductive aminations of carbonyl compounds with borohydride and borane reducing agents. In: Overman LE, ed. *Organic Reactions*. John Wiley & Sons, Inc. 2002.

72. Saxena V, Sadoqi M, Shao J, Kumar S. Enhanced Intracellular Uptake of Indocyanine Green by Polymeric Nanoparticulate Delivery Systems. *Journal of Biomedical Nanotechnology*. 2005;1(2):168–175.

73. Yu J, Javier D, Yaseen M a, et al. Self-assembly synthesis, tumor cell targeting, and photothermal capabilities of antibody-coated indocyanine green nanocapsules. *J Am Chem Soc*. 2010;132(6):1929–38.

74. Moghimi SM, Szebeni J. Stealth liposomes and long circulating nanoparticles: critical issues in pharmacokinetics, opsonization and protein-binding properties. *Progress in Lipid Research*. 2003;42(6):463–478.

75. He Q, Zhang J, Shi J, et al. The effect of PEGylation of mesoporous silica nanoparticles on nonspecific binding of serum proteins and cellular responses. *Biomaterials*. 2010;31(6):1085–92.

76. Emoto K, Nagasaki1 Y, Iijima M, Kato M, Kataoka K. Preparation of non-fouling surface through the coating with core-polymerized block copolymer micelles having aldehyde-ended PEG shell. *Colloids and surfaces. B, Biointerfaces*. 2000;18(3-4):337–346.

77. Shapiro HM. *Practical flow cytometry*. New Jersey: John Wiley and Sons. Inc. 2003.

78. Levchenko TS, Rammohan R, Lukyanov AN, Whiteman KR, Torchilin VP. Liposome clearance in mice: the effect of a separate and combined presence of surface charge and polymer coating. *International journal of pharmaceutics*. 2002;240(1-2):95–102.

79. Frangioni J. In vivo near-infrared fluorescence imaging. *Curr Opin Chem Biol*. 2003;7(5):626–634.

80. Peer D, Karp JM, Hong S, Farokhzad OC, Margalit R, Langer R. Nanocarriers as an emerging platform for cancer therapy. *Nat Nanotechnol*. 2007;2(12):751–60.

81. Sevick-Muraca EM, Houston JP, Gurfinkel M. Fluorescence-enhanced, near infrared diagnostic imaging with contrast agents. *Curr Opin Chem Biol*. 2002;6(5):642–50.

82. Ntziachristos V, Bremer C, Weissleder R. Fluorescence imaging with near-infrared light: new technological advances that enable in vivo molecular imaging. *Eur Radiol*. 2003;13(1):195–208.

83. He X, Gao J, Gambhir SS, Cheng Z. Near-infrared fluorescent nanoprobes for cancer molecular imaging: status and challenges. *Trends Mol Med*. 2010;16(12):574–83.

84. Kim S, Lim YT, Soltesz EG, et al. Near-infrared fluorescent type II quantum dots for sentinel lymph node mapping. *Nat Biotechnol*. 2004;22(1):93–7.

85. Yaseen M a, Yu J, Wong MS, Anvari B. In-vivo fluorescence imaging of mammalian organs using charge-assembled mesocapsule constructs containing indocyanine green. *Opt Express*. 2008;16(25):20577–87.

86. Bahmani B, Gupta S, Upadhyayula S, Vullev VI, Anvari B. Effect of polyethylene glycol coatings on uptake of indocyanine green loaded nanocapsules by human spleen macrophages in vitro. *J Biomed Opt*. 2011;16(5):051303.

87. Yannuzzi L a. Indocyanine green angiography: a perspective on use in the clinical setting. *Am J Ophthalmol*. 2011;151(5):745–751.e1.

88. Ross A, Ross AH, Mohamed Q. Review and update of central serous chorioretinopathy. *Curr Opin Ophthalmol*. 2011;22(3):166–73.

89. Mantel I, Uffer S, Zografos L. Peripheral exudative hemorrhagic chorioretinopathy: a clinical, angiographic, and histologic study. *Am J Ophthalmol*. 2009;148(6):932–8.e1.

90. Tanaka E, Chen FY, Flaumenhaft R, Graham GJ, Laurence RG, Frangioni J V. Real-time assessment of cardiac perfusion, coronary angiography, and acute intravascular thrombi using dual-channel near-infrared fluorescence imaging. *J Thorac Cardiovasc Surg*. 2009;138(1):133–40.

91. El-Desoky a, Seifalian a M, Cope M, Delpy DT, Davidson BR. Experimental study of liver dysfunction evaluated by direct indocyanine green clearance using near infrared spectroscopy. *British J surg*. 1999;86(8):1005–11.

92. Hirano A, Kamimura M, Ogura K, et al. A comparison of indocyanine green fluorescence imaging plus blue dye and blue dye alone for sentinel node navigation surgery in breast cancer patients. *Ann Surg Oncol*. 2012;19(13):4112–6.

93. Kitai T, Inomoto T, Miwa M, Shikayama T. Fluorescence navigation with indocyanine green for detecting sentinel lymph nodes in breast cancer. *Breast cancer*. 2005;12(3):211–5.

94. Miyashiro I, Miyoshi N, Hiratsuka M, et al. Detection of sentinel node in gastric cancer surgery by indocyanine green fluorescence imaging: comparison with infrared imaging. *Ann Surg Oncol*. 2008;15(6):1640–3.

95. Nimura H, Narimiya N, Mitsumori N, Yamazaki Y, Yanaga K, Urashima M. Infrared ray electronic endoscopy combined with indocyanine green injection for detection of sentinel nodes of patients with gastric cancer. *Br J Surg*. 2004;91(5):575–9.

96. Uhara H, Yamazaki N, Takata M, et al. Applicability of radiocolloids, blue dyes and fluorescent indocyanine green to sentinel node biopsy in melanoma. *J Dermatol*. 2012;39(4):336–8.

97. Van der Vorst JR, Schaafsma BE, Verbeek FPR, et al. Randomized comparison of near-infrared fluorescence imaging using indocyanine green and 99(m) technetium with or without patent blue for the sentinel lymph node procedure in breast cancer patients. *Ann Surg Oncol*. 2012;19(13):4104–11.

98. Moretó M. Diagnosis of esophagogastric tumors. *Endoscopy*. 2003;35(1):36–42.

99. Yamamoto T, Narushima M, Doi K, et al. Characteristic indocyanine green lymphography findings in lower extremity lymphedema: the generation of a novel lymphedema severity staging system using dermal backflow patterns. *Plast Reconstr Surg*. 2011;127(5):1979–86.

100. Yamamoto T, Yamamoto N, Doi K, et al. Indocyanine green-enhanced lymphography for upper extremity lymphedema: a novel severity staging system using dermal backflow patterns. *Plast Reconstr Surg*. 2011;128(4):941–7.

101. Yoneya S, Saito T, Komatsu Y, Koyama I, Takahashi K, Duvoll-Young J. Binding properties of indocyanine green in human blood. *Invest Ophth Vis Sci*. 1998;39(7):1286–90.

102. Altinoğlu EI, Adair JH. Near infrared imaging with nanoparticles. *Wiley Interdiscip Revi Nanomed Nanobiotechnol*. 2(5):461–77.

103. Sharma P, Bengtsson NE, Walter G a, et al. Gadolinium-doped silica nanoparticles encapsulating indocyanine green for near infrared and magnetic resonance imaging. *Small*. 2012;8(18):2856–68.

104. Alexis F, Pridgen E, Molnar LK, Farokhzad OC. Factors Affecting the Clearance and Biodistribution of Polymeric Nanoparticles. *Mol Pharm*. 2008;5(4):505–515.

105. Hoffman A. non-fouling surfaces. *J Biomater Sci Polymer Edn*. 1999;10(10):1011–1014.

106. Bahmani B, Gupta S, Vullev V, Anvari B. Uptake of PEGylated indocyanine green loaded nanocapsules by cells of reticuloendothelial system. In: Achilefu S, Raghavachari R, eds. *Reporters, Markers, Dyes, Nanoparticles, and Molecular Probes for Biomedical Applications III*.Vol 7910. SPIE; 2011:79101C–79101C–7.

107. Bahmani B, Jung B, Gupta S, Anvari B. Cellular uptake of polymeric nanocapsules loaded with ICG by human blood monocytes and human spleen macrophages. In:

Achilefu S, Raghavachari R, eds. *Reporters, Markers, Dyes, Nanoparticles, and Molecular Probes for Biomedical Applications III*.Vol 7576. SPIE; 2010:75761Q–75761Q–6.

108. Ebert B, Licha K. Cyanine dyes as contrast agents for near-infrared imaging in vivo : acute tolerance , pharmacokinetics , and fluorescence imaging Cyanine dyes as contrast agents for near-infrared imaging in vivo : acute tolerance , pharmacokinetics. *J Biomed Opt*. 2011;16(6):066003.

109. Houston JP, Ke S, Wang W, Li C, Sevick-Muraca EM. Quality analysis of in vivo near-infrared fluorescence and conventional gamma images acquired using a dual-labeled tumor-targeting probe. *J Biomed Opt*. 2005;10(5):054010.

110. Saxena V, Sadoqi M, Shao J. Polymeric nanoparticulate delivery system for Indocyanine green: biodistribution in healthy mice. *Int J Pharm*. 2006;308(1-2):200–4.

111. Cui Y, Leier I, Buchholz U, Keppler D. Hepatic Uptake of Bilirubin and Its Conjugates by the Human Organic Anion Transporter SLC21A6 *. *J Biol Chem*. 2001;276(13):9626–9630.

112. Cesta MF. Normal structure, function, and histology of the spleen. *Toxicol Pathol*. 2006;34(5):455–65.

113. Mebius RE, Kraal G. Structure and function of the spleen. *Nat Rev Immunol*. 2005;5(8):606–16.

114. Card JW, Zeldin DC, Bonner JC, Nestmann ER. Pulmonary applications and toxicity of engineered nanoparticles. *Am J Physiol - Lung C*. 2008:400–411.

115. Leckband D, Sheth S, Halperin A. Grafted poly(ethylene oxide) brushes as nonfouling surface coatings. *J Biomater Sci Polymer Edn*. 1999;10:1125–1147.

116. Upadhyayula S, Quinata T, Bishop S, et al. Coatings of polyethylene glycol for suppressing adhesion between solid microspheres and flat surfaces. *Langmuir*. 2012;28(11):5059–69.

117. Ma Y, Sadoqi M, Shao J. Biodistribution of indocyanine green-loaded nanoparticles with surface modifications of PEG and folic acid. *Int J Pharm*. 2012;436(1-2):25–31.

118. Zheng C, Zheng M, Gong P, et al. Indocyanine green-loaded biodegradable tumor targeting nanoprobes for in vitro and in vivo imaging. *Biomaterials*. 2012;33(22):5603–9.

119. Fang C, Shi B, Pei Y-Y, Hong M-H, Wu J, Chen H-Z. In vivo tumor targeting of tumor necrosis factor-alpha-loaded stealth nanoparticles: effect of MePEG molecular weight and particle size. *Eur J Pharm Sci*. 2006;27(1):27–36.

120. Ballou B, Lagerholm BC, Ernst L a, Bruchez MP, Waggoner AS. Noninvasive imaging of quantum dots in mice. *Bioconjugate Chem*. 2004;15(1):79–86.

121. Ohno K, Akashi T, Tsujii Y, Yamamoto M, Tabata Y. Blood Clearance and Biodistribution of Polymer Brush-Afforded Silica Particles Prepared by Surface-Initiated Living Radical Polymerization. *Biomacromolecules*. 2012.

122. Shah NB, Vercellotti GM, White JG, Fegan A, Wagner CR, Bischof JC. Blood−Nanoparticle Interactions and in Vivo Biodistribution: Impact of Surface PEG and Ligand Properties. *Mol Pharm*. 2012;9:2146–2155.

123. Bahmani B, Vullev V, Anvari B. Development of anti-HER2 conjugated ICG-loaded polymeric nanoparticles for targeted optical imaging of ovarian cancer. In: Achilefu S, Raghavachari R, eds. *Reporters, Markers, Dyes, Nanoparticles, and Molecular Probes for Biomedical Applications III*.Vol 8233. SPIE; 2012:82330L–82330L–6.

124. Jemal A, Siegel R, Xu J, Ward E. Cancer Statistics , 2010 BOTH SEXES FEMALE BOTH SEXES ESTIMATED DEATHS. 2010;60(5):277–300. doi:10.1002/caac.20073.Available.

125. Bahmani B, Lytle CY, Walker AM, Gupta S, Vullev VI, Anvari B. Effects of nanoencapsulation and PEGylation on biodistribution of indocyanine green in healthy mice: quantitative fluorescence imaging and analysis of organs. *International journal of nanomedicine*. 2013;8:1609–20.

126. Berchuck A, Kamel A, Whitaker R, et al. Overexpression of HER-2 / neu Is Associated with Poor Survival in Advanced Epithelial Ovarian Cancer Overexpression of HER-2 / neu Is Associated with Poor Survival in Advanced Epithelial Ovarian Cancer1. *Cancer Research*. 1990;50:4087–4091.

127. Campiglio M, Ali S, Knyazev PG, Ullrich a. Characteristics of EGFR family-mediated HRG signals in human ovarian cancer. *Journal of cellular biochemistry*. 1999;73(4):522–32.

128. Lee C, Ph D, Huntsman DG, et al. Assessment of Her-1 , Her-2 , and Her-3 Expression and Her-2 Amplification in Advanced Stage Ovarian Carcinoma. 2005:147–152.

129. Pansare V, Hejazi S, Faenza W, Prud'homme RK. Review of Long-Wavelength Optical and NIR Imaging Materials: Contrast Agents, Fluorophores and Multifunctional Nano Carriers. *Chemistry of materials : a publication of the American Chemical Society*. 2012;24(5):812–827.

130. Fox JJ, Wood EH. Application of dilution curves recorded from the right side of the heart or venous circulation with the aid of a new indicator dye. *Proceeding of Staff Meeting Mayo Clinic*. 1957;32(19):541–550.

131. CAESAR J, SHALDON S, CHIANDUSSI L, GUEVARA L, SHERLOCK S. The use of indocyanine green in the measurement of hepatic blood flow and as a test of hepatic function. *Clinical Science*. 1961;21:43–57.

132. Van der Vorst JR, Schaafsma BE, Verbeek FPR, et al. Dose optimization for near-infrared fluorescence sentinel lymph node mapping in patients with melanoma. *The British journal of dermatology*. 2013;168(1):93–8.

133. Jeschke S, Lusuardi L, Myatt A, Hruby S, Pirich C, Janetschek G. Visualisation of the lymph node pathway in real time by laparoscopic radioisotope- and fluorescence-guided sentinel lymph node dissection in prostate cancer staging. *Urology*. 2012;80(5):1080–6.

134. Crane LM a, Themelis G, Arts HJG, et al. Intraoperative near-infrared fluorescence imaging for sentinel lymph node detection in vulvar cancer: first clinical results. *Gynecologic oncology*. 2011;120(2):291–5.

135. Sevick-Muraca EM, Sharma R, Rasmussen JC, et al. Imaging of Lymph Flow in Breast Cancer Patients after Microdose Administration of a Methods : Results : Conclusion : 2008;246(3):734–741.

136. SMRETSCHNIG, EVA, ANSARI-SHAHREZAEI S, HAGEN, STEFAN, GLITTENBERG, CARL, KREBS I, BINDER S. Half-fluence photodynamic therapy in chronic central serous chorioretinopathy. *Retina*. 2013;33(2):316–323.

137. YANNUZZI, LAWRENCE A., SLAKTER, JASON S. , GROSS, NICOLE E., SPAIDE, RICHARD F., COSTA, DANIELLE L.L., HUANG, SHEAU J., KLANCNIK, JAMES M., AIZMAN A. ndocyanine green angiography-guided photodynamic therapy for treatment of chronic central serous chorioretinopathy: a pilot study. *Retina*. 2003;23(3):288–298.

138. Costa R a, Scapucin L, Moraes NS, et al. Indocyanine green-mediated photothrombosis as a new technique of treatment for persistent central serous chorioretinopathy. *Current eye research*. 2002;25(5):287–97.

139. Klein a, Szeimies R-M, Bäumler W, et al. Indocyanine green-augmented diode laser treatment of port-wine stains: clinical and histological evidence for a new treatment option from a randomized controlled trial. *The British journal of dermatology*. 2012;167(2):333–42.

140. Liggett P, Lavaque A, Chaudhry N, Jablon E, Quiroz-Mercado H. Preliminary results of combined simultaneous transpupillary thermotherapy and ICG-based photodynamic therapy for choroidal melanoma. *Ophthalmic Surgery, Laser & Imaging*. 2005;36(6):463–470.

141. Jung B, Rao ALN, Anvari B. Optical nano-constructs composed of genome-depleted brome mosaic virus doped with a near infrared chromophore for potential biomedical applications. *ACS nano*. 2011;5(2):1243–52.

142. Gupta S, Chatni MR, Rao ALN, Vullev VI, Wang L V, Anvari B. Virus-mimicking nano-constructs as a contrast agent for near infrared photoacoustic imaging. *Nanoscale*. 2013;5(5):1772–6.

143. Pierigè F, Serafini S, Rossi L, Magnani M. Cell-based drug delivery. *Advanced drug delivery reviews*. 2008;60(2):286–95.

144. Muzykantov VR. Drug delivery by red blood cells: vascular carriers designed by Mother Nature. *Expert Opinion in Drug Delivery*. 2011;7(4):403–427.

145. Gutiérrez Millán, Carmen , Gandarillas CIC, Marinero MLS, Lanao JM. Cell-based drug delivery platforms. *Therapeutic Delivery*. 2012;3(1):25–41.

146. Hu C-MJ, Fang RH, Zhang L. Erythrocyte-inspired delivery systems. *Advanced healthcare materials*. 2012;1(5):537–47.

147. Brähler M, Georgieva R, Buske N, et al. Magnetite-loaded carrier erythrocytes as contrast agents for magnetic resonance imaging. *Nano letters*. 2006;6(11):2505–9.

148. Chang M, Hsiao J-K, Yao M, et al. Homologous RBC-derived vesicles as ultrasmall carriers of iron oxide for magnetic resonance imaging of stem cells. *Nanotechnology*. 2010;21(23):235103.

149. Antonelli A, Sfara C, Manuali E, Bruce I, Magnani M. Encapsulation of superparamagnetic nanoparticles into red blood cells as new carriers of MRI contrast agents. *Nanomedicine (Lond)*. 2011;6(2):211–223.

150. Ahn S, Jung SY, Seo E, Lee SJ. Gold nanoparticle-incorporated human red blood cells (RBCs) for X-ray dynamic imaging. *Biomaterials*. 2011;32(29):7191–9.

151. Milanick M a, Ritter S, Meissner K. Engineering erythrocytes to be erythrosensors: first steps. *Blood cells, molecules & diseases*. 2011;47(2):100–6.

152. Ritter SC, Milanick M a, Meissner KE. Encapsulation of FITC to monitor extracellular pH: a step towards the development of red blood cells as circulating blood analyte biosensors. *Biomedical optics express*. 2011;2(7):2012–21.

153. Flower R, Peiretti E, Magnani M, et al. Observation of erythrocyte dynamics in the retinal capillaries and choriocapillaris using ICG-loaded erythrocyte ghost cells. *Investigative ophthalmology & visual science*. 2008;49(12):5510–6.

154. Kasha M, Rawls HR, Ashraf El-Bayoumi M. The exciton model in molecular spectroscopy. *Pure Applied Chemistry*. 1965;11:371–392.

155. Holzer W, Mauerer M, Penzkofer a, et al. Photostability and thermal stability of indocyanine green. *Journal of photochemistry and photobiology. B, Biology*. 1998;47(2-3):155–64.

156. Hu C-MJ, Zhang L, Aryal S, Cheung C, Fang RH, Zhang L. Erythrocyte membrane-camouflaged polymeric nanoparticles as a biomimetic delivery platform. *Proceedings of the National Academy of Sciences of the United States of America*. 2011;108(27):10980–5.

157. Domenech C, Thomas X, Chabaud S, et al. l-asparaginase loaded red blood cells in refractory or relapsing acute lymphoblastic leukaemia in children and adults: results of the GRASPALL 2005-01 randomized trial. *British journal of haematology*. 2011;153(1):58–65.

158. Bossa F, Latiano A, Rossi L, et al. Erythrocyte-mediated delivery of dexamethasone in patients with mild-to-moderate ulcerative colitis, refractory to mesalamine: a randomized, controlled study. *The American journal of gastroenterology*. 2008;103(10):2509–16.